WASHINGTON UNIVERSITY IN ST. LOUIS

McKelvey School of Engineering
Department of Electrical & Systems Engineering

Dissertation Examination Committee:
Kater Murch, Chair
Erik Henriksen
Matthew Lew
Aravind Nagulu
Karthik Ramanathan

Control and Thermodynamics of Superconducting Qubits with Non-Hermitian Dynamics

by

Serra Erdamar

A dissertation presented to
the McKelvey School of Engineering
of Washington University in
partial fulfillment of the
requirements for the degree
of Doctor of Philosophy

December 2025
St. Louis, Missouri

Table of Contents

List of Figures . . . . . **iv**

Acknowledgments . . . . . **vi**

Abstract . . . . . **x**

Chapter 1: Introduction **1**

Chapter 2: Non-Hermitian Quantum Systems and Open Quantum Systems **4**
2.1 Mathematical framework of non-Hermitian Hamiltonians 5
2.1.1 Lindblad master equation and effective non-Hermitian Hamiltonian . 5
2.1.2 Non-Hermitian eigenstate normalization 8
2.2 Parity-time ($\mathcal{PT}$) symmetry and its properties 8
2.3 Experimental Realization 12
2.3.1 Superconducting Non-Hermitian Qubit 12
2.3.2 Tomography 13
2.3.3 Flux noise and filtering 18
2.3.4 Exceptional points and phase transitions 19
2.3.5 Explorations of the topology 21

Chapter 3: Shortcuts to Adiabaticity and Counterdiabatic Control of a Non-Hermitian qubit **24**
3.1 Adiabaticity in quantum systems 24
3.1.1 Notion of adiabaticity for open quantum systems 26
3.2 Counterdiabatic driving theory 28
3.2.1 Reverse engineering to achieve the adiabatic state 29
3.2.2 Non-Hermitian counterdiabatic drive 30
3.3 Implementation of counterdiabatic protocols 32
3.3.1 Evaluating the success of the counterdiabatic drive 33
3.3.2 Defining Apollonius circles and parameter space relationships 38
3.3.3 Counterdiabatic generalized to complex coupling 42
3.3.4 Exploring the effect of non-Hermitian components in the counterdiabatic drive 44
3.3.5 Resolving the Riemann sheet topology 45

3.4 Hermitian counterdiabatic drive by way of single eigenstate tracking 47
3.5 Conclusion 51

Chapter 4: Thermodynamics in quantum systems 53
4.1 The first and second laws of thermodynamics 53
4.2 Fluctuation theorems 56
4.2.1 The Jarzynski equality 58
4.2.2 Energy distribution and measurements 60
4.3 Results 63
4.4 Numerical simulations exploring non-cyclic paths 68
4.5 Conclusion - discussion of net heat 70

Chapter 5: Conclusions and Future Directions 72

References 74

List of Figures

Figure 1.1: Relaxation and dephasing time 2

Figure 2.1: Setup 5

Figure 2.2: Rabi oscillations in a non-Hermitian system 7

Figure 2.3: $\mathcal{PT}$-symmetry 9

Figure 2.4: Eigenvalue properties of a non-Hermitian Hamiltonian 11

Figure 2.5: Fridge diagram 14

Figure 2.6: Engineering enhanced dissipation 15

Figure 2.7: Readout thresholding 17

Figure 2.8: Bloch sphere 19

Figure 2.9: Transition across the EP 20

Figure 2.10: Riemann sheets and encircling the exceptional point 23

Figure 3.1: Adiabaticity condition of non-Hermitian systems near an EP 27

Figure 3.2: Parallel transport 31

Figure 3.3: Encircling an EP with and without counterdiabatic driving 34

Figure 3.4: Counterdiabatic driving result visualized on Bloch sphere. 35

Figure 3.5: Evaluating the efficacy of counterdiabatic driving over time 36

Figure 3.6: Evaluating the success of counterdiabatic driving 37

Figure 3.7: Evaluating the counterdiabatic drive using fidelity 38

Figure 3.8: Hyperbolic angle and y-axis 41
Figure 3.9: Parameter space and Bloch coordinate state space visualization 42
Figure 3.10: Quantifying deviations from the Apollonius circle 46
Figure 3.11: Resolving the Riemann sheet branch cut 47
Figure 3.12: Hermitian counterdiabatic drive from single eigenstate tracking 49
Figure 3.13: Single eigenstate tracking method experimental results 50

Figure 4.1: First Law 54
Figure 4.2: Particles in a box 56
Figure 4.3: General protocol for experiment 64
Figure 4.4: Parameter paths 65
Figure 4.5: Obtaining the work probability distribution 65
Figure 4.6: Transition probabilities 66
Figure 4.7: Jarzynski equality evaluated for different paths 67
Figure 4.8: Emergent parity-time symmetry 69
Figure 4.9: Jarzynski equality evaluated for non-cyclic paths 70

Acknowledgments

As my academic journey comes to an end, I want to recognize my family, friends, and mentors without whom I couldn't have completed this work. I want to begin by thanking my advisor, Kater Murch. My journey with Kater didn't begin with my PhD studies but actually during my sophomore year of my undergraduate studies. I was initially interested in studying astrophysics, but after taking Kater's course on Introduction to Quantum Physics I, I was convinced. His enthusiasm, intuition, and ability to make science fun and a part of life drew me in. A subject as unintuitive as quantum physics became applicable and intriguing. I learned that I could fulfill my dream of combining my engineering studies with physics in this wonderful field of experimental superconducting qubits. Studying under his guidance has shaped me as a scientist and as a person, and I am forever grateful to Kater for being an encouraging and patient mentor and for spreading his appreciation for science and life.

Maryam Abbasi holds a special place in my graduate studies from the beginning. I could not have asked for a better mentor and close friend to look up to. She made the last several years of learning and experiments feel enjoyable. We laughed through the good and the hard times. Thank you for always graciously answering my (endless) questions. I am extremely grateful for the knowledge and patience of my other mentors Weijian, Chandra, and Daria. I am inspired by the work and learning ethic of all of my labmates Alexandria, Xingrui, Kaiwen, Pratik, Orion, Qian, and Sean. My first project was completed with an undergraduate senior, Byung Ha. I joined the experiment along with him and was lucky to experience his intelligence and kindness as a new member of the lab!

I want to thank Yashika Kapoor for being a constant source of support and friendship over the last few years. Her dedication to research and her expertise were inspiring. Matt joined our lab in the later part of my PhD, and I think we can all agree that we don't know how we survived before he joined. His breadth of knowledge, constant curiosity, and fearlessness in just taking something apart to fix it have made me a better experimentalist. I want to thank my committee members: Matthew Lew, Erik Henriksen, Aravind Nagulu, and Karthik Ramanathan for their interest in my research and for their genuine support in helping me complete a fulfilling PhD degree.

Working with non-Hermitian Hamiltonians has been theory-heavy, and I thank our theory collaborators, Yogesh Joglekar, Aurélia Chenu, Niklas Hörnedal, and Jacob Muldoon, for taking the time to explain theoretical concepts and elegant mathematics. My intuition and appreciation for our experimental systems has greatly increased due to our conversations! I had the wonderful opportunity to complete an internship at MIT Lincoln Laboratory in my last year. I was inspired by the intelligent community and the enthusiastic learning style of the group and am incredibly excited to join as my next chapter!

My family has been an incredible support system throughout this journey. My parents instilled in me a love of learning new things. I want to thank them for being an inspiration to me and an endless source of knowledge. I am grateful for their encouragement and advice as I developed my love for science and for being an unconditional source of comfort, kindness, and love. I want to thank my sister, Aylin, for being my best friend and a source of joy and relief whenever I needed it. I am incredibly thankful for Ben Wagoner and for his love and patience throughout this journey. His passionate dedication to his work and curiosity of learning new things is inspirational.

I want to give honorable mention to my cat, Pauli, who, unlike the exclusion principle discovered by his namesake Wolfgang Pauli, never excluded himself from any space I was working in. His constant company while curled up on my warm laptop, overheating from having Python, MATLAB, Overleaf, and Slack open simultaneously, was a source of comfort and a gentle reminder to get up and stretch (usually to throw his toy).

I want to thank the funding that allowed me to complete this research: it was supported by NSF Grant No. PHY-2408932, the Air Force Office of Scientific Research (AFOSR) Multidisciplinary University Research Initiative (MURI) Award on Programmable systems with non-Hermitian quantum dynamics (Grant No. FA9550-21-1-0202), ONR Grant No. N000142512160. I acknowledge support from the National Science Foundation Research Traineeship (NRT) grant number 2152221, Linking Quantum Sensing Technologies across Disciplines: a Convergent Quantum Sciences and Engineering Graduate Training Program. The devices were fabricated and provided by the Superconducting Qubits at Lincoln Laboratory (SQUILL) Foundry at MIT Lincoln Laboratory, with funding from the Laboratory for Physical Sciences (LPS) Qubit Collaboratory.

Serra Erdamar

Washington University in St. Louis
December 2025

To my family and friends.

ABSTRACT OF THE DISSERTATION

Control and Thermodynamics of Superconducting Qubits with Non-Hermitian Dynamics

by

Serra Erdamar

Doctor of Philosophy in Electrical Engineering

Washington University in St. Louis, 2025

Professor Kater Murch, Chair

As quantum systems are understood better from a fundamental physics perspective, we are gaining more insight and ideas for their many applications. Among them are quantum computation, sensing, and materials. Some difficulties that have been encountered are short lifetimes and coupling to unwanted modes while attempting to control these systems, resulting in error propagation. Previously, physicists have pursued Hermitian descriptions of systems to preserve unitary evolution and real-valued measurements. However, non-Hermitian systems not only provide a realistic description of physical systems within larger environments, but also a rich topological landscape from their complex energy spectrum. In this thesis, we will explore how to control a non-Hermitian qubit to utilize its complex spectrum and the role of its Hamiltonian in energetics and time dynamics. Because superconducting qubits offer flexibility in parameter tuning, we can tune the values of the non-Hermitian Hamiltonian to explore this complex spectrum across regions of both $\mathcal{PT}$-symmetry and $\mathcal{PT}$-symmetry breaking. This complex energy spectrum forms a Riemann surface that has a branch cut and branch points (exceptional points). Encircling these exceptional points adiabatically allows for state transport that can non-trivially convert between eigenstates. Previous experimental studies of this process revealed a chirality: eigenstate conversion occurs when following the state with higher gain, but breaks down when following the state with higher loss. We explore how the interplay between gain and loss in modes of the system results

in the breakdown of this adiabaticity and how we can use a method based on shortcuts to adiabaticity to circumvent this. Finally, we leverage this tunability to further investigate how the components of the non-Hermitian Hamiltonian relate to classical thermodynamic notions of internal energy and work in time-dependent protocols via the Jarzynski equality.

Chapter 1

Introduction

The field of quantum physics has progressed tremendously over the last century. Quantum systems have been extended to various platforms to utilize different control parameters and prioritize certain benefits. For example, the crux of many quantum systems for scalability and the application of quantum algorithms is their finite lifetimes, noise causing decoherence, and coherence in unwanted spaces (the first two are depicted in Figure 1.1 for a two-level system on a Bloch sphere). The finite lifetime is characterized by a T_1 relaxation measurement where the quantum system is prepared in an excited state and its population decay to the ground state is represented by $P_e(t) = P_e(0)e^{-t/T_1}$ [1]. Decoherence in the form of dephasing results from stochastic shifts in the system frequency, thus causing us to lose phase information of the quantum state. For frequency ω_q, the phase after time t is $\phi = \omega_q t + \epsilon$ with uncertainty ϵ. The timescale over which this occurs is characterized using a Ramsey measurement and is called a T_2^* time [1]. Many efforts aim to minimize the loss through design improvements [2, 3, 4, 5, 6] or through mathematical algorithms such as the surface code in the category of "Quantum Error Correction" [7, 8, 9, 10, 11]. For the issue of coupling to other coherent subspaces, important quantum control techniques to minimize this effect include creating pulses with Derivative Removal by Adiabatic Gate (DRAG) [12, 13] or with pulse shaping methods using spectral decomposition [14]. These methods are useful for frequently used pulses like π-pulses or $\pi/2$-pulses which are applied to bring a qubit from one state to the other, 180 or 90 degrees away on the 3-dimensional Bloch sphere, respectively. These pulses have a certain frequency that corresponds to the resonance of the transition, a phase that corresponds to the axis of rotation, and an amplitude envelope that determines strength over time. Previously (and most simply), these pulses were applied with a square amplitude envelope. However, the sharp edges can have a frequency spectrum at unintended values. When the time-dependent pulse is spectrally decomposed, these frequencies can be at the anharmonicity difference which can excite those higher energy transitions. These three pulse parameters give us the tools to apply pulses like DRAG or other pulse shaping methods to cancel out and minimize

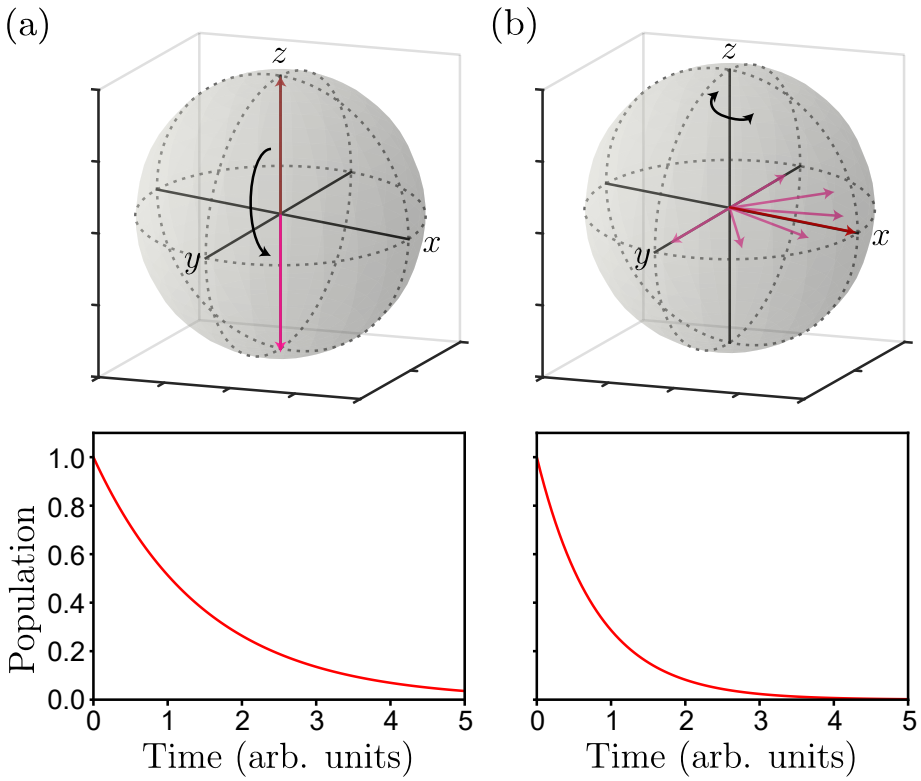

Figure 1.1: **Relaxation and dephasing time.** (a) Single relaxation event depicted on the Bloch sphere (upper) and in terms of population averaged over many events versus time (lower). (b) Dephasing depicted on the Bloch sphere (upper) and in terms of phase information transferred to units of population (lower). Reproduced from [1].

the coupling to unwanted states. These methods allow us to apply fast pulses that also cancel out unintended frequencies and are an example of engineering for quantum systems.

Other kinds of quantum control are those in which the protocol requires the system to be in an eigenstate of the time-dependent Hamiltonian (during which the previous parameters of frequency, phase and amplitude can be varied) [15, 16, 17]. The system remains in the instantaneous eigenstate when the Hamiltonian parameters are varied *adiabatically*. The adiabatic theorem states that if a system's parameters are varied slowly enough, it will remain in the same eigenstate of the instantaneous Hamiltonian [18, 19]. If a system is driven too fast, non-adiabatic transitions will occur between eigenstates. However, if it is driven too slowly, a quantum system succumbs to loss. In our quest to control quantum systems better, we encounter a trade-off between speed for faster computation to avoid this decay and maintaining equilibrium to stay in the desired subspace.

Our chosen platform is a superconducting qubit described by a non-Hermitian Hamiltonian [20]. This type of system provides a rich landscape due to its complex energy spectrum. The real and imaginary parts of the eigenenergies form what are called Riemann sheets and require adiabatic tuning of the parameters to traverse them. The motivation for following the Riemann sheets closely is to resolve and utilize their topological features, including branch cuts and branch points (exceptional points), which allow for state transport between eigenstates [15, 21, 22, 23, 24, 25, 26, 27, 16]. Chapter 2 will explore the theory and experimental verification of this energy spectrum. The imaginary components of these eigenenergies correspond to gain and loss and ultimately lead to the breakdown of adiabaticity when attempting to observe the state transport. In Chapter 3 we will explore the conditions for adiabaticity and methods of Shortcuts to Adiabaticity (STA) to circumvent both non-adiabatic transitions out of the eigenstate and loss due to decoherence. The method of STA we use is called counterdiabatic driving and was first independently developed by Demirplak and Rice [28] and Berry [29]. The technique at the time was aptly called transitionless driving to indicate the suppression of non-adiabatic transitions. This approach allows us to tune our parameters at faster-than-adiabatic speeds and resolve the Riemann topology by remaining on the eigenstate of the instantaneous Hamiltonian.

Our study on adiabatic control of Hamiltonians has also motivated us to explore these processes from a thermodynamic perspective, where optimizing measurements for work, heat, and efficiency can give new insight into quantum control. Quantum thermodynamics in recent years has explored the meaning of measurements as they pertain to feedback, cost, coupling to a measurement apparatus, and measurement strength [30, 31, 32, 33, 34, 35, 36, 37, 38, 39, 40, 41, 42]. In understanding measurements, it has been shown that they can actually be a resource for quantum-based engines [43]. The Hamiltonian describing these systems governs the dynamics and also measurement expectation values. In the case of non-Hermitian Hamiltonians, energy is complex which adds new richness to classical thermodynamics. We need to take care in how we measure our qubit for meaningful energetics. In Chapter 4, we explore how we can characterize the energetics and understand the dynamics in a non-Hermitian qubit using the Jarzynski equality [44]. The non-Hermitian Hamiltonian that describes this qubit is special in that it can obey passive-$\mathcal{PT}$-symmetry with balanced gain and loss. The parameters can be tuned such that we can explore the regions of balanced or imbalanced gain and loss. The consequences of the non-Hermitian Hamiltonian dissatisfying $\mathcal{PT}$-symmetry manifest in our measurements of the internal energy change of the non-Hermitian qubit.

Chapter 2

Non-Hermitian Quantum Systems and Open Quantum Systems

This thesis focuses on experiments performed with superconducting circuits called transmons [45]. Following the discovery in 2007, numerous theses have been written on this topic, with fundamental construction and measurement principles particularly well described in [46, 47, 1, 48]. The basic setup that we will utilize is presented in Fig. 2.1. The qubit is physically embedded in an environment where coupling to nearby elements such as resonators, flux lines, and other qubits is necessary for coherent control and readout; however, complete isolation of the qubit from external unwanted effects is not possible (Fig. 2.1a). Therefore, it is important to study and understand systems in interaction with their surroundings. The following sections will develop mathematical (Sections 2.1 and 2.2) and experimental techniques (Section 2.3) to realize and measure a non-Hermitian qubit based on a superconducting circuit. This type of circuit has both capacitance and non-linear inductance, which results in an anharmonic potential (Fig. 2.1b) of which we will focus on the lower three levels [45]. The "qubit" will refer to the $\{|e\rangle, |f\rangle\}$ energy levels. The qubit is dispersively coupled to a readout resonator (gray), a drive line (pink), and flux line (green) for control. These couplings, though necessary for measurement and control, offer channels for energy decay. One main source of decoherence, which is observable through the state population, is decay/dissipation from higher energy levels to lower ones (γ_e and γ_f). Another source of decoherence, which is observable through sequences that translate rotational phase to population, is dephasing (γ_{ϕ_e} and γ_{ϕ_f}). The non-Hermitian Hamiltonian that describes this qubit can obey $\mathcal{PT}$ symmetry, which corresponds to a system with balanced gain and loss and results in real eigenvalues (Sec. 2.2). We will see that the dynamics of the non-Hermitian Hamiltonian and its complex eigenstates and eigenvalues are experimentally observable in Sections 2.3.4 and 2.3.5.

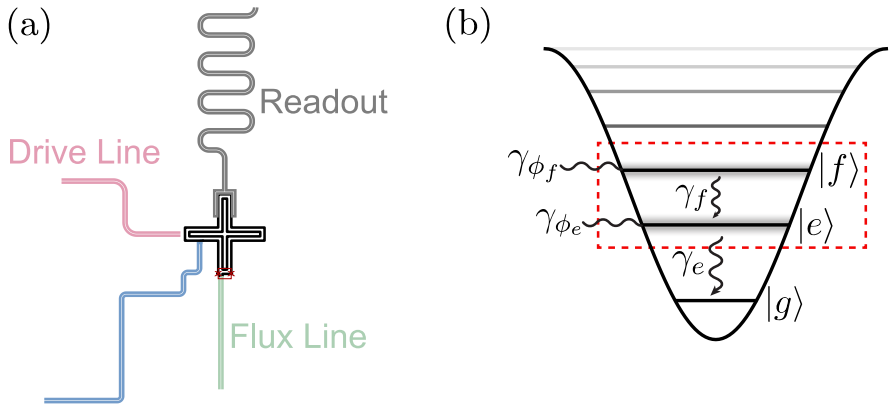

Figure 2.1: **Setup.** (a) Transmon dispersively coupled to a readout resonator, drive line, flux line, and external coaxial cable for engineered dissipation. (b) We will focus on the lowest three energy levels of an anharmonic potential $\{|g\rangle, |e\rangle, |f\rangle\}$. There is dissipation from $|f\rangle \to |e\rangle$ at rate γ_f and $|e\rangle \to |g\rangle$ at rate γ_e. There is dephasing of the qubit transition frequencies at rate γ_{ϕ_f} and γ_{ϕ_e} corresponding to $|f\rangle$ and $|e\rangle$, respectively.

2.1 Mathematical framework of non-Hermitian Hamiltonians

2.1.1 Lindblad master equation and effective non-Hermitian Hamiltonian

Open quantum systems can be described in the Lindblad master equation formalism. This allows us to define dissipators that describe energy transitions that can happen within the system due to an environment. These dissipators are of the form: $L_k = \sqrt{\gamma_k}|i\rangle\langle k|$ where $|k\rangle \to |i\rangle$ when describing radiative decay or $L_{2k} = \sqrt{\gamma_{\phi_k}/2}|k\rangle\langle k|$ when describing dephasing. We begin by looking at a 3×3 density matrix ρ_3 that describes the state in the lower three energy levels (Fig. 2.1b). H_c is the Hermitian coupling Hamiltonian that describes the drive applied to the $\{|e\rangle, |f\rangle\}$ manifold with strength J and detuning $\Delta = \omega_{\text{drive}} - \omega_{ef}$ and is defined: $H_c = \Delta|e\rangle\langle e| + J(|e\rangle\langle f| + |f\rangle\langle e|)$.

$$\dot{\rho_3} = -i[H_c, \rho_3] + \sum_{k\in e,f} L_k \rho_3 L_k^\dagger - \sum_{k\in e,f,2e,2f} \frac{1}{2}\{L_k^\dagger L_k, \rho_3\}. \tag{2.1}$$

When the dissipator decay rates satisfy $\gamma_f, \gamma_{\phi_f}, \gamma_{\phi_e} \ll \gamma_e$, we can consider $\sum_{k\in f,2e,2f} \frac{1}{2}\{L_k^\dagger L_k, \rho_3\}$ and $L_f \rho_3 L_f^\dagger$ negligible and rearrange this description to obtain the resulting effective non-Hermitian Hamiltonian, H_{eff} [20] in Eq. (2.2). The first term $(-i(H_{\text{eff}}\rho_3 - \rho_3 H_{\text{eff}}^\dagger))$ corresponds to non-unitary coherent non-Hermitian evolution and the second term $(L_e \rho_2 L_e^\dagger)$ corresponds to stochastic and random quantum jumps to the $|g\rangle$ state. The loss contrast is defined as $\gamma \equiv \gamma_e - \gamma_f$ when γ_f is not negligible.

$$\dot{\rho_3} = -i(H_{\text{eff}}\rho_3 - \rho_3 H_{\text{eff}}^\dagger) + L_e \rho_3 L_e^\dagger, \tag{2.2}$$

where $H_{\text{eff}} = H_c - \frac{i}{2} L_e^\dagger L_e$. Since the qubit of interest is the two-level system comprised of $\{|e\rangle, |f\rangle\}$ we can look at that 2×2 manifold and write the equation of motion:

$$H_{\text{eff}} = \begin{pmatrix} \Delta - i\gamma/2 & J \\ J & 0 \end{pmatrix}, \tag{2.3}$$

$$\dot{\rho_2} = -i\left(H_{\text{eff}}\rho_2 - \rho_2 H_{\text{eff}}^\dagger\right). \tag{2.4}$$

Evolution according to Eq. (2.4) is non-unitary and not trace-preserving. Therefore, we re-normalize our state to be trace preserving by:

$$\rho = \rho_2 / \text{Tr}[\rho_2]. \tag{2.5}$$

The density matrix can be decomposed into different components that represent the population and coherence of the qubit states.

$$\rho = \begin{pmatrix} \rho_{ee} & \rho_{ef} \\ \rho_{fe} & \rho_{ff} \end{pmatrix} \tag{2.6}$$

The components that correspond to the post-selected state population are the diagonal elements, $P_e = \rho_{ee}$ and $P_f = \rho_{ff}$. To build some intuition about how the post selected effective non-Hermitian evolution affects the state, we plot P_e and P_f with $\Delta = 0$ and some arbitrary non-zero drive strength J in Figure 2.2. In Fig. 2.2a, we see symmetric Rabi

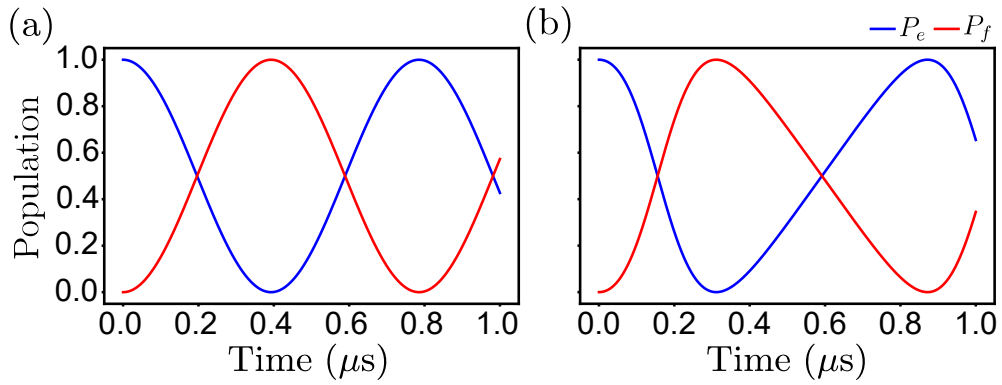

Figure 2.2: **Rabi oscillations in a non-Hermitian system.** Population of P_e and P_f plotted as a function of time with arbitrary drive strength J and $\Delta = 0$. (a) Normal Rabi oscillations with $\gamma = 0$. The rise and fall time is symmetric for P_e and P_f. (b) Rabi oscillations according to Eq. (2.5). There is an asymmetry between the population behavior. P_f has relative gain.

oscillations, where $\gamma = 0$. This corresponds to oscillations seen in Hermitian qubits. In Fig. 2.2b we see asymmetry in the rise and fall time for the populations of $|e\rangle$ and $|f\rangle$. Due to the measurement back-action of the post-selection, one state has relative gain compared to the other state. If the system is initialized in the $|e\rangle$ state where $P_e = 1$ and a drive is applied to the qubit, the loss of the $|e\rangle$ state corresponds to a relative gain of the $|f\rangle$ state, toward which the system tends.

The eigenvalues and eigenstates of H_{eff} are defined as $H_{\text{eff}}|\lambda_n\rangle = \lambda_n|\lambda_n\rangle$ where n represents indexing the positive and negative eigenstates with $n \in \pm$.

$$\lambda_n = \frac{\Delta}{2} - \frac{i\gamma}{4} \pm \sqrt{\frac{1}{4}(\Delta - \frac{i\gamma}{2})^2 + J^2} \tag{2.7}$$

$$|\lambda_+\rangle = \cos(\alpha/2)|e\rangle + \sin(\alpha/2)|f\rangle \tag{2.8}$$

$$|\lambda_-\rangle = -\sin(\alpha/2)|e\rangle + \cos(\alpha/2)|f\rangle \tag{2.9}$$

where $\alpha = \arctan\frac{|J|}{\Delta/2 - i\gamma/4}$. $\alpha = \alpha_{\text{R}} + i\alpha_{\text{I}}$ is referred to as the complex mixing angle. When the imaginary part is related to the non-orthogonality of the eigenstates and when it is zero, we obtain the orthogonal Hermitian Hamiltonian eigenstates. The dynamics of this system

in the $\{|e\rangle, |f\rangle\}$ basis is governed by the complex eigenvalue gap $\delta\lambda = \sqrt{(\Delta - \frac{i\gamma}{2})^2 + 4J^2}$. This will be further explored in the experimental Section 2.3.4.

2.1.2 Non-Hermitian eigenstate normalization

For Hermitian systems one obtains the property that $\langle\psi_i|\psi_j\rangle = \delta_{ij}$, meaning that the eigenstates form an orthonormal basis. When dealing with non-Hermitian eigenstates which are generally non-orthogonal, we cannot assume this same property. Therefore, we need to define left and right eigenstates separately that form a biorthogonal basis. The right eigenstates are defined familiarly as $H_{\text{eff}}|\lambda_n\rangle = \lambda_n|\lambda_n\rangle$ and the left as $H_{\text{eff}}^{\dagger}|\hat{\lambda}_n\rangle = \lambda_n^*|\hat{\lambda}_n\rangle$. They are called "left" eigenvectors because they satisfy: $\langle\hat{\lambda}_n|H_{\text{eff}} = \langle\hat{\lambda}_n|\lambda_n$. Where $n \in \{1, 2, ..., N\}$ and N is the number of eigenstates (nondegenerate). The dagger means complex conjugate transpose and the asterisk means complex conjugate. The left eigenstates in the bra space are:

$$\langle\hat{\lambda}_+| = \cos(\alpha/2)\langle e| + \sin(\alpha/2)\langle f| \tag{2.10}$$

$$\langle\hat{\lambda}_-| = -\sin(\alpha/2)\langle e| + \cos(\alpha/2)\langle f| \tag{2.11}$$

These left and right eigenstates form the biorthogonal basis and satisfy: $\langle\hat{\lambda}_n|\lambda_m\rangle = \delta_{n,m}$. We can see that the coefficients of the eigenstates are normalized due to: $\cos(\alpha/2)^2 + \sin(\alpha/2)^2 = 1$. These states also satisfy completeness/closure relations with [49, 50]:

$$\sum_i |\lambda_n\rangle\langle\hat{\lambda}_n| = \sum_i |\hat{\lambda}_n\rangle\langle\lambda_n| = 1 \tag{2.12}$$

2.2 Parity-time ($\mathcal{PT}$) symmetry and its properties

When dealing with quantum systems and measurements, one generally requires a Hermitian Hamiltonian that has a real energy spectrum and unitary time evolution so that probabilities are conserved. This indicates that energy is not leaving or entering the system, and therefore the system is isolated. For example, for a Hermitian Hamiltonian, H, an initial state can be evolved with unitary evolution operator $\hat{U}_t = e^{-iHt}$: $|\psi_t\rangle = \hat{U}_t|\psi_0\rangle$. The probability is conserved as: $\langle\psi_t|\psi_t\rangle = \langle\psi_0|\hat{U}_t^{\dagger}\hat{U}_t|\psi_0\rangle = \langle\psi_0|\psi_0\rangle$. In 1998, Carl Bender [51] showed that

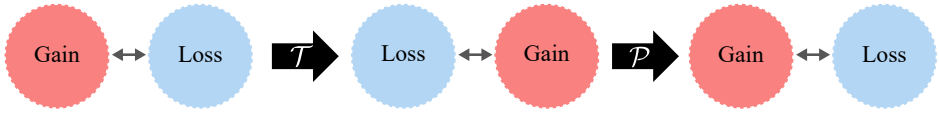

Figure 2.3: **$\mathcal{PT}$-symmetry.** The red circles represent a system with gain at rate κ and the blue circles represent a system with loss at rate $-\kappa$. The $\mathcal{T}$ operator switches the direction of gain/loss and $\mathcal{P}$ switches the position. The double sided arrows between systems represent coupling introduced between them. Adapted from $\mathcal{PT}$-symmetry works such as [52, 53].

there is a more relaxed and physically significant condition that Hamiltonians can obey to preserve the real energy spectrum other than $H = H^\dagger$. This condition is called Parity Time ($\mathcal{PT}$) symmetry where $\mathcal{P}$ is the space reflection operator:

$$\mathcal{P} = \begin{pmatrix} 0 & 1 \\ 1 & 0 \end{pmatrix} \tag{2.13}$$

and $\mathcal{T}$ is complex conjugation: $\mathcal{T}i\mathcal{T}^{-1} = -i$. $\mathcal{T}$ can also be called the time reflection operator. As seen in the Schrodinger equation: $i\hbar\frac{\partial}{\partial t}\psi = H\psi$, the imaginary term i is associated with time t. Thus, reversing the direction of i reverses the direction of time. These properties are also independent of each other: $[\mathcal{P}, \mathcal{T}] = 0$. A Hamiltonian is said to be $\mathcal{PT}$-symmetric when it obeys the commutation relation $[\mathcal{PT}, H] = 0$, thus remaining invariant under space-time reflections. If there are two separate systems (or modes), one with gain rate κ and the other with loss rate $-\kappa$, the composite system of these two subsystems has net rate $\kappa + (-\kappa) = 0$. This system has a net probability flux of zero, but is still not in equilibrium because one subsystem is growing and the other is decaying. If these two subsystems are directly connected, the gain of one system can flow into the system with loss, maintaining an equilibrium. We can see how this kind of system obeys $\mathcal{PT}$-symmetry since if we flip the position of the two subsystems ($\mathcal{P}$) and then flip the sign of κ ($\mathcal{T}$), we return to the original configuration as depicted in Fig. 2.3. Here, the color of each subsystem corresponds to gain (κ) or loss ($-\kappa$) (red or blue, respectively). This allowed the discovery of a group of non-Hermitian Hamiltonians, where $H \neq H^\dagger$, that have a real energy spectrum. This special group of non-Hermitian Hamiltonians are able to achieve a balanced gain and loss of energy/population transfer and maintain conservation of probability.

Looking at our eigenvalues from Eq. (2.7), we observe that there is an overall background loss common to both $-i\gamma/4$. Our effective non-Hermitian Hamiltonian can then be rearranged

as $H_{\mathcal{PT}} = H_{\text{eff}} - i\gamma/4$ and is referred to as a *passive* $\mathcal{PT}$-system since there is one mode with dominant loss:

$$H_{\mathcal{PT}} = \begin{pmatrix} \Delta - i\gamma/4 & J \\ J & +i\gamma/4 \end{pmatrix} \tag{2.14}$$

which has eigenvalues:

$$\lambda_{n,\mathcal{PT}} = \pm\sqrt{\frac{1}{4}(\Delta - \frac{i\gamma}{2})^2 + J^2} \tag{2.15}$$

This Hamiltonian satisfies the condition of $[\mathcal{PT}, H_{\mathcal{PT}}] = 0$ when $\Delta = 0$. This condition can be rewritten as $(\mathcal{PT})H_{\mathcal{PT}}(\mathcal{PT})^{-1} = H_{\mathcal{PT}} \rightarrow \mathcal{P}H^*_{\mathcal{PT}}\mathcal{P}^{-1} = H_{\mathcal{PT}}$. Since $\mathcal{P}$ is a reflection operator, it satisfies $\mathcal{P}^2 = 1$ and $\mathcal{P} = \mathcal{P}^{-1}$.

$$\mathcal{P}H^*\mathcal{P} = \begin{pmatrix} 0 & 1 \\ 1 & 0 \end{pmatrix} \begin{pmatrix} -i\gamma/4 & J \\ J & +i\gamma/4 \end{pmatrix}^* \begin{pmatrix} 0 & 1 \\ 1 & 0 \end{pmatrix} = H \tag{2.16}$$

The eigenvalues of this Hamiltonian have a complex spectrum as a function of its parameters Δ and J (Fig. 2.4a). Due to the negative sign under the square root function, the eigenvalues are able to merge as J is varied. This results in an *exceptional point* (EP) at $J = \pm\gamma/4,\ \Delta = 0$. When $|J| > |J_{\text{EP}}|$, the system is in a regime of unbroken $\mathcal{PT}$-symmetry and the eigenvalues, $\lambda_{n,\mathcal{PT}}$ are purely real (blue region Fig. 2.4). When $|J| < |J_{\text{EP}}|$, the system is in a regime of broken $\mathcal{PT}$-symmetry and the eigenvalues, $\lambda_{n,\mathcal{PT}}$ are purely imaginary (red region Fig. 2.4). In the $\mathcal{PT}$ unbroken regime, the system is in a dynamic equilibrium, thus, resembling a closed (isolated) system. When it is in the broken regime, the eigenvalues are complex conjugates and have equal and opposite values in their imaginary component (red region Fig. 2.4c). The system is not in equilibrium but due to one eigenstate growing and the other decaying, the net probability flux is zero [52]. When $\Delta \neq 0$, the eigenvalues become complex and are no longer complex conjugates.

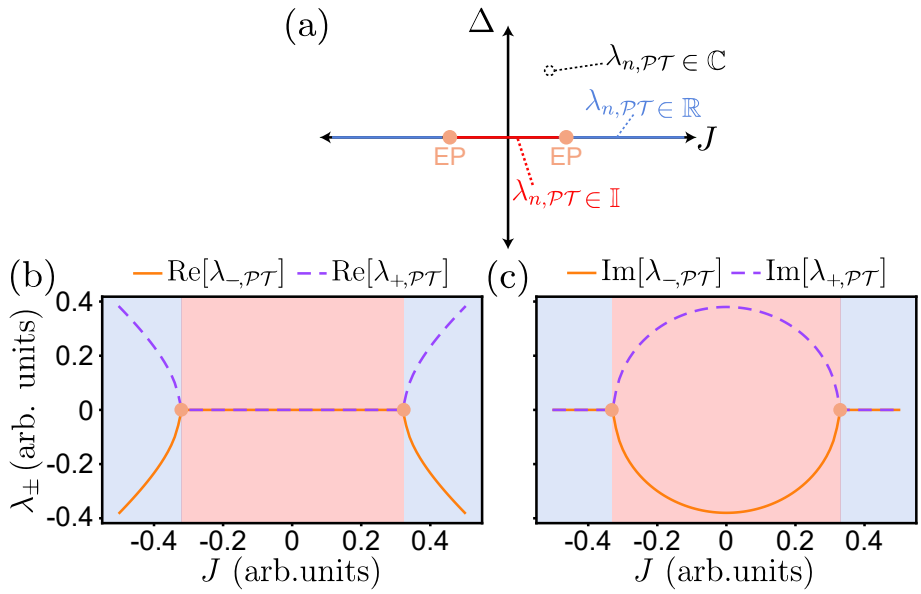

Figure 2.4: **Eigenvalue properties of a non-Hermitian Hamiltonian** (a) The eigenvalues $\lambda_{n,\mathcal{PT}}$ (2.15) of Eq. (2.14) plotted as a function of drive strength J and detuning Δ. An exceptional point (EP) occurs at $J = \pm\gamma/4$ where the eigenvalues and eigenstates coalesce. The eigenvalues become purely real (blue lines) when $|J| > |J_{\mathrm{EP}}|$ and purely imaginary (red line) when $|J| < |J_{\mathrm{EP}}|$ and $\Delta = 0$. The eigenvalues for $\Delta = 0$ are plotted in (b) and (c) to verify the spectrum in the $\mathcal{PT}$-symmetric regime. (b) $\mathrm{Re}[\lambda_{n,\mathcal{PT}}]$ is plotted as a function of J. The two EPs are observed at the transition points from $\mathcal{PT}$ unbroken (non-zero real part) to $\mathcal{PT}$ broken (zero real part) and back to $\mathcal{PT}$ unbroken. (c) The same transitions are observable for the imaginary component: $\mathrm{Im}[\lambda_{n,\mathcal{PT}}]$. Where instead we have zero imaginary part in the $\mathcal{PT}$ unbroken regions and purely imaginary in $\mathcal{PT}$ broken.

2.3 Experimental Realization

$\mathcal{PT}$-symmetric systems have since been realized on many platforms such as optical [54, 55, 56, 57, 58, 59, 60], photonics [61], spin systems [62], and cold atoms [63]. Intuitively and most simply, $\mathcal{PT}$-symmetric systems consist of a gain system coupled to a loss system, for example a whispering gallery mode resonator with gain and one with loss [59]. In this work, we show how we are able to achieve the same dynamics with mode-selective loss, also known as a passive $\mathcal{PT}$-symmetric system, in a superconducting qubit.

2.3.1 Superconducting Non-Hermitian Qubit

Our setup consists of a superconducting flux tunable qubit with a maximum (sweet spot) frequency of $\omega_{ge}/2\pi = 4.373$ GHz. The qubit is tunable by having a dc superconducting quantum interference device (SQUID) as the non-linear element instead of a single Josephson junction [64]. A SQUID consists of two parallel junctions that allow for the critical current to be tuned by applying a magnetic flux through this loop using a dc current. The SQUID is schematically represented by the red circuit in Fig. 2.1a and Fig. 2.5. We use a subset (Q2) of a two-qubit chip fabricated by MIT Lincoln Laboratory (Fig. 2.5). It is dispersively coupled to a resonator with frequency $\omega_r/2\pi = 6.88865$ GHz, a linewidth of $\kappa/2\pi = 246$ kHz, and a coupling rate of $g/2\pi = 33$ MHz. The dispersive shift for a two-level system is $\chi \approx g^2/(\omega_q - \omega_r) = g^2/\delta$ [45]. The setup includes a drive line (Fig. 2.5 blue "DL2") for manipulating the qubit with microwave sequences consisting of π pulses and Rabi drives, making it easy to control the frequency, amplitude and phase of our signals.

To realize the non-Hermitian qubit on our superconducting qubit platform we need to induce extra loss in just the $|e\rangle$ state. We do this by coupling an off-chip resonator to the qubit at a frequency that is slightly below the sweet spot frequency of the $\{|g\rangle, |e\rangle\}$ transition, at $\omega_{\mathrm{NH}}/2\pi = 4.25$ GHz. We then flux tune the qubit down in resonance using a current source applied to the flux line (Fig. 2.5 purple "p2"). This induces a Purcell effect decay into the resonator from the qubit [65, 66, 67]. This off-chip resonator is simply a coaxial cable trimmed down in length to correspond to the required frequency. The pin at the center of the connectors are broken off to create an effective capacitance at either end. To measure this effect, we perform a T_1, or relaxation time, sequence to measure $\gamma_e = 1/T_1$.

The sequence is a π pulse to bring the state to the $|e\rangle$ state through the drive line, and then a variable wait time before performing a readout pulse (Fig. 2.6) through the input readout line. The sequence is then repeated with different DC current values (flux Φ/Φ_0) applied to Q2 flux or global flux. Tuning the flux applied to the SQUID changes the resonance frequency of the energy levels. The goal is to match the resonance of the $\{|g\rangle, |e\rangle\}$ transition to the external coax filter so that the decay rate γ_e (μs^{-1}) is maximized (Fig. 2.6b). The maximum of Fig. 2.6b is $\gamma_e = 1.44\ \mu s^{-1}$, but over the course of separate fridge cool downs and recalibration, this number varies from $\gamma_e \simeq 1.3 - 1.9\ \mu s^{-1}$ among the following experimental results and $\gamma_f \simeq 0.2\ \mu s^{-1}$.

2.3.2 Tomography

We've introduced that coupling to other on-chip elements can lead to dissipation, however, these couplings are also important for readout. Readout has been established and written about in many papers and theses [45, 68, 69, 1, 47], but the basic idea is that the signal passing through the readout resonator acquires a dispersive shift χ. Due to the dispersive shift, we can probe our resonator with a microwave tone through the readout "in" line and obtain a phase shift from the readout "out" line using homodyne detection (Fig. 2.5) [68, 69, 1]. The photons that populate the resonator through the readout line acquire a phase shift on the way out that is dependent on the resonator's frequency which is dependent on the qubit state. This signal is then amplified using a flux pumped Josephson Parametric Amplifier (JPA) and a high-electron mobility (HEMT) amplifier (Fig. 2.5). We want to resolve the phase shift of the three lowest transmon states $\{|g\rangle, |e\rangle, |f\rangle\}$. When considering higher excited states with anharmonicity $\eta = \omega_{ef} - \omega_{ge}$, frequency transition $\omega_{i,i+1} = \omega_{i+1} - \omega_i$, and coupling rate $g_{i,i+1} \approx \sqrt{i+1} g_g$, where $i \in \{|g\rangle, |e\rangle, |f\rangle\}$, the dispersive shift for a two-level system becomes [70, 47]:

$$\chi_{ge} + \frac{\chi_{ef}}{2} = -\frac{g_{ge}^2}{\delta}\left(\frac{1}{1+\delta/\eta}\right). \tag{2.17}$$

When considering the χ_i for $\{|g\rangle, |e\rangle, |f\rangle\}$ we can use [71]:

$$\chi_{i,i+1} = \frac{g_{i,i+1}^2}{\omega_{i,i+1} - \omega_r}. \tag{2.18}$$

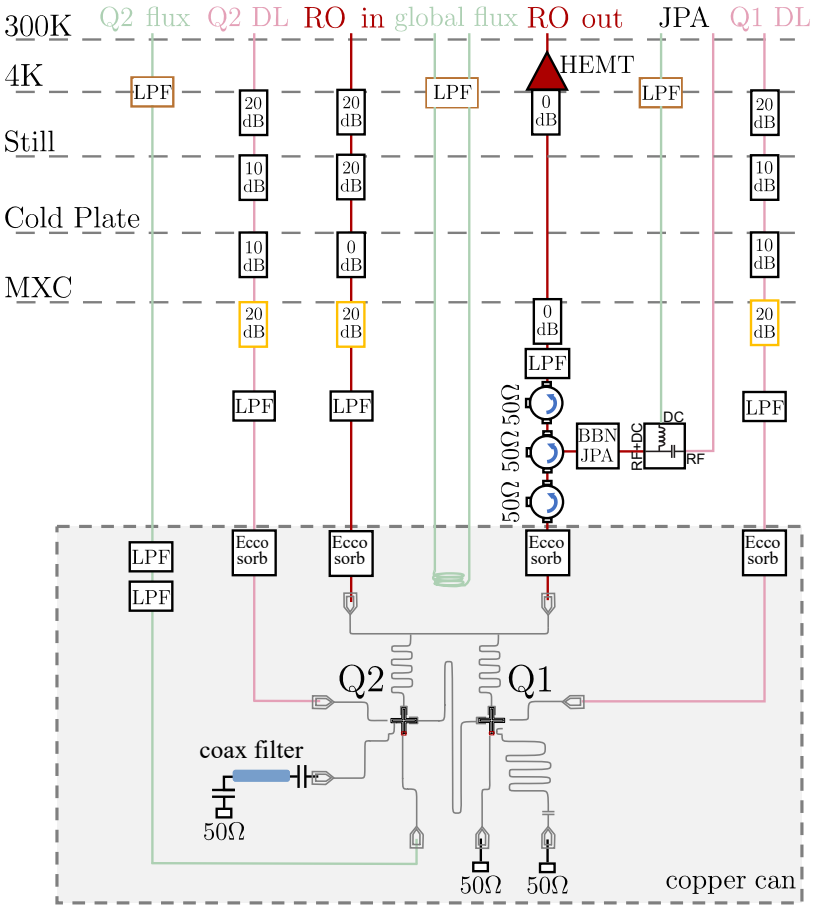

Figure 2.5: **Fridge diagram** The qubit chip is mounted at the mixing chamber stage (MXC) at ~ 10 mK inside a copper can. There are two qubits on this chip, labeled Q1 and Q2. The qubit we use as a non-Hermitian qubit is Q2. There is an off-chip coaxial cable capacitively coupled to the chip and terminated on the other end at 50Ω. The qubit is flux biased (Q2 flux green line) with a DC twisted pair. This signal is passed through a low-pass filter (LPF) from QDevil of 65 kHz mounted at the 4K stage. Pulses and drives on the qubit are applied through a drive line (pink line). This also passes through various attenuators and filters for thermalization and noise filtration. The qubit state is then readout by applying a readout (RO) pulse through the transmission line to the resonator (RO in, red line), and readout through the output of the transmission line (RO out, red line). The readout signal is amplified using a Josephson Parametric Amplifier (JPA) from Raytheon BBN and a high-electron mobility (HEMT LPF) amplifier. The JPA is flux biased through its green line and pumped through its pink pump line. If needed, the global flux of the chip can be biased through twisted DC pairs (green lines with coil). All lines are filtered with a combination of LPFs or high cut-off frequency infrared filters (Eccosorb) to filter out unwanted frequencies and attenuators (decibel dB) to help thermalize and reduce thermal noise.

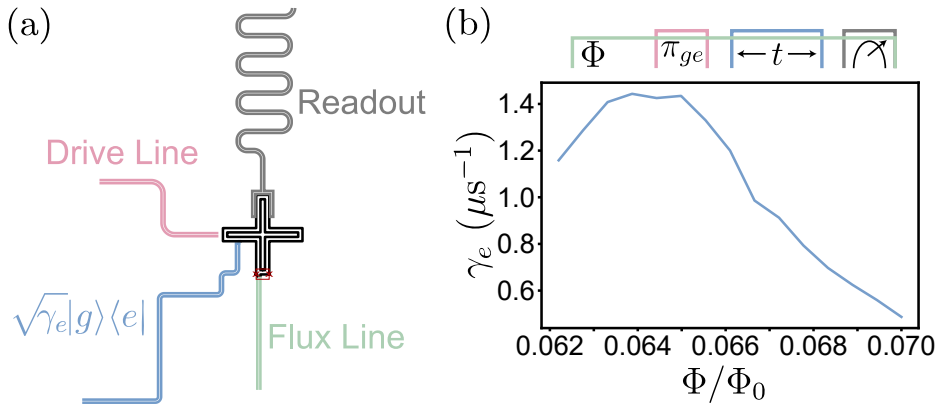

Figure 2.6: **Engineering enhanced dissipation.** (a) Flux line used to apply a DC current to the SQUID (green). Drive line used to apply π pulses (pink). Readout resonator dispersively coupled to the qubit for state dependent readout (gray). (b) (upper inset) A DC pulse is applied throughout the sequence through the flux line (green). A π_{ge} pulse is applied through the drive line to bring the state to $|e\rangle$. A variable amount of time t is waited before applying a readout pulse.

Through demodulation of our signal we obtain the phase (frequency) shift of the resonator frequency $I = \cos(\theta)$ and $Q = \sin(\theta)$ which can be plotted to visualize the spread of the data (Fig. 2.7). We can rotate our data around this plot to maximize the amount of information on a single axis (I or Q) (Fig. 2.7a) and then plot the data in a histogram format along that axis (Fig. 2.7b).

We define a general pulse $s(t; t_0, t_f, \omega_{i-1,i}, A)$ with initial time t_0, final time t_f, transition frequency $\omega_{i-1,i}$, and amplitude A. The main tools we will utilize are π-pulses to prepare one of three states $\{0, s(\pi_{ge}, \omega_{ge}, A_{ge}), s(\pi_{ef}, \omega_{ef}, A_{ef})\} : \{|g\rangle, |e\rangle, |f\rangle\}$, where not applying a π-pulse prepares the $|g\rangle$ state, a readout pulse with frequency ω_{RO} and amplitude A_{RO} to probe the resonator through the input line, and JPA pump frequency, power, and bias to optimize the gain of the output signal. By careful tuning of these parameters, we can optimize our resolution and separation of the phase shift between these three states. The preparation of each state is obtained by repeating three different sequences:

$$|g\rangle : s(t; 0, t_{\mathrm{RO}}, \omega_{\mathrm{RO}}, A_{\mathrm{RO}}) \tag{2.19}$$

$$|e\rangle : s(t; 0, \pi_{ge}, \omega_{ge}, A_{\mathrm{ge}}) + s(t; \pi_{ge}, \pi_{ge} + t_{\mathrm{RO}}, \omega_{\mathrm{RO}}, A_{\mathrm{RO}}) \tag{2.20}$$

$$|f\rangle : s(t; 0, \pi_{ge}, \omega_{ge}, A_{\mathrm{ge}}) + s(t; \pi_{ge}, \pi_{ge} + \pi_{ef}, \omega_{ef}, A_{\mathrm{ef}}) \tag{2.21}$$

$$+ s(t; \pi_{ge} + \pi_{ef}, \pi_{ge} + \pi_{ef} + t_{\mathrm{RO}}, \omega_{\mathrm{RO}}, A_{\mathrm{RO}}) \tag{2.22}$$

We aim to maximize the metric of signal-to-noise ratio (SNR) to tune these parameters:

$$\mathrm{SNR} = \left| \frac{\mu_k - \mu_l}{(\sigma_k - \sigma_l)/2} \right|^2 \tag{2.23}$$

Where $k, l \in \{g, e, f\}$ and μ is the mean and σ is the standard deviation of the Gaussian fit to each state as seen in Fig. 2.7b. We can now optimize the SNR by sweeping ω_{RO} to find the dispersive shift that gives us best separation for both $\{|g\rangle, |e\rangle\}$ and $\{|e\rangle, |f\rangle\}$. Tuning the readout duration, t_{RO}, can also increase the separation in readout between the states. Longer t_{RO} increases the separation due to integrating over more data, but also allows for decay during the readout process, so we need to find the tradeoff balance between the two effects. We can also increase the readout amplitude, A_{RO}, for more readout power but that can cause spurious transitions from lower states to higher states and deviation in the spread of the clusters from Gaussian circles [69, 68, 4].

Once the SNR is calibrated, we can again fit to a three-Gaussian function (Fig. 2.7a) and extract the intersections between the two nearest neighbor Gaussians. This gives us our threshold bounds to threshold the IQ data into one of three states: $\{|g\rangle, |e\rangle, |f\rangle\}$.

In certain readout setups, it can be difficult to optimize the readout parameters to have clear separation along one axis, but enough within the full IQ picture. In these cases, we can employ machine learning tools to threshold our data such as "k-means" and "support-vector-machine". "k-means" is an unsupervised learning technique used to find a specified number of "k" clusters and provide labels for each (Fig. 2.7c). "Support-vector-machine" is a supervised learning technique that receives classified (pre-labeled) data and tries to find lines that best divide these classes (Fig. 2.7d) [72, 73].

Due to some leakage from higher states to lower states due to short lifetimes compared to the readout pulse, the fidelity of thresholding the data is lower. We can predict the amount of mixing and circumvent this by applying a scale matrix, M.

$$M = \begin{pmatrix} p_{gg} & p_{ge} & p_{gf} \\ p_{eg} & p_{ee} & p_{ef} \\ p_{fg} & p_{fe} & p_{ff} \end{pmatrix} \tag{2.24}$$

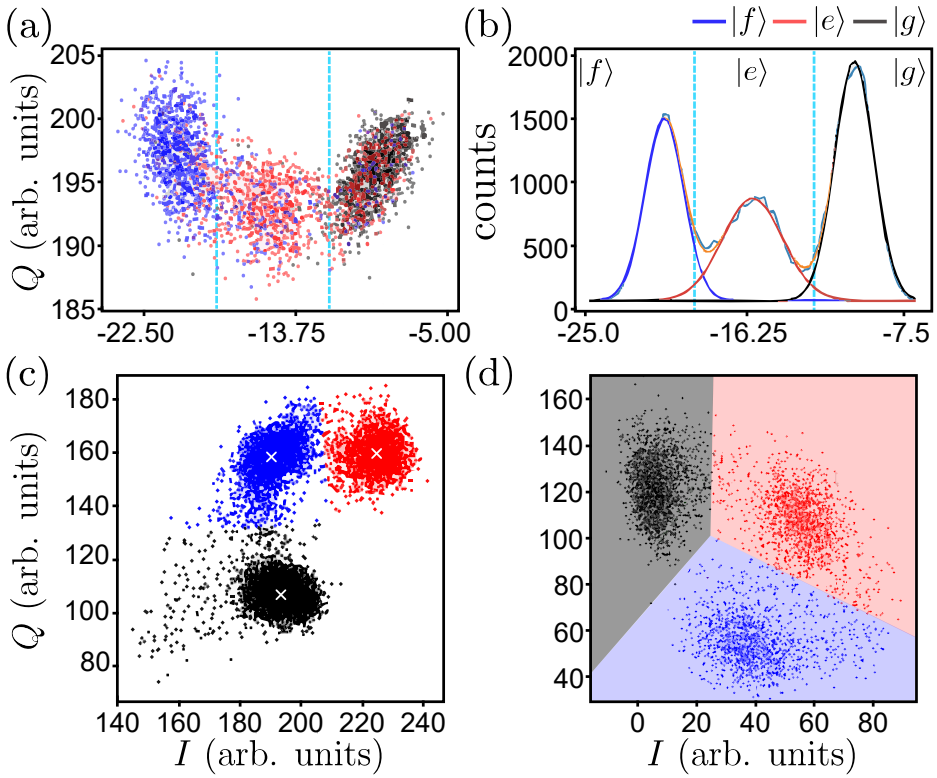

Figure 2.7: **Dispersive shift readout methods.** Experimental results are thresholded according to the following three methods. (a) Readout calibration sequence results are rotated to maximize information along one axis (I axis). (b) Binning the results along the I axis as a histogram to visualize the distribution of acquired points. We can then fit the counts to three Gaussian distributions. (a)-(b) The vertical dashed lines represent the found threshold values on the I axis. (c) "k-means" method of clustering and colored by the cluster classes (white x's are included as illustration). (d) "Support vector machine" (SVM) method of clustering. The points are prelabeled by the readout sequence they were obtained from. SVM finds lines that best divide the three classes. Each point is colored according to the fit results.

The diagonal elements p_{kk} tell us the fidelity at which each state $|k\rangle$ was measured. The off-diagonals tell us the mixing between each state. For example, p_{ge} is the probability of preparing $|g\rangle$ and measuring $|e\rangle$.

If $\tilde{P}_k$ are the populations we measure, our knowledge of our state measurement error from M can be used to scale to our populations to P'_k :

$$\begin{pmatrix} P'_g \\ P'_e \\ P'_f \end{pmatrix} = M^{-1} \begin{pmatrix} \tilde{P}_g \\ \tilde{P}_e \\ \tilde{P}_f \end{pmatrix}. \tag{2.25}$$

Finally, the post-selected populations are obtained from $P_e = \frac{P'_e}{P'_f + P'_e}$ and $P_f = \frac{P'_f}{P'_f + P'_e}$.

These calibrations have been in the z measurement energy basis due to the dispersive coupling. To reconstruct the density matrix, we need full state tomography to access the expectation values of the three Pauli matrices $\{\sigma_x, \sigma_y, \sigma_z\}$: $\rho = \frac{1}{2}(I + \langle x\rangle\sigma_x + \langle y\rangle\sigma_y + \langle z\rangle\sigma_z)$. This involves calibrating the pulses to measure the other two axes $\{x, y\}$. These are related to z by a $\pi/2$ rotation along the polar angle and a 0 or 90° phase for the azimuthal angle. This is easier to visualize using a Bloch sphere and with the vector notation that represents a state on the sphere: $|\psi\rangle = \cos(\theta/2)|0\rangle + e^{i\phi}\sin(\theta/2)|1\rangle$ (Fig. 2.8). Where $|0\rangle, |1\rangle$ represent the ground and excited state of any two level system. For future calibrations of the non-Hermitian qubit, they are assigned to $|e\rangle, |f\rangle$. Furthermore, the eigenstates of σ_x, $|\pm x\rangle$, can be calibrated using the azimuthal angle 180 and 0, respectively. Eigenstates of a Hamiltonian are also known as "stationary states". Therefore, when tuning the amplitude and phase of these pulses, we can apply a Rabi drive on the orthogonal axis, and look for a flat response (amplitude of oscillation is zero).

2.3.3 Flux noise and filtering

Due to the addition of a flux line, we are now susceptible to flux noise carried on this line. More-so when we are operating away from the flux sweet spot. The qubit frequency can only be tuned down from the sweet spot frequency due to the effective Josephson energy having the external flux Φ_{ext} dependence, $2E_J|\cos\Phi_{\text{ext}}/\Phi_0|$ [70]. This is why we created the external

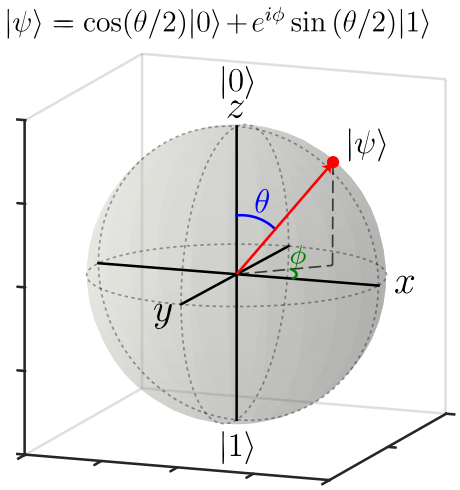

Figure 2.8: **Bloch sphere.** A qubit state on the Bloch sphere can be described using a polar angle θ and azimuthal angle ϕ as $|\psi\rangle = \cos(\theta/2)|0\rangle + e^{i\phi}\sin(\theta/2)|1\rangle$.

coaxial filter to be slightly below the sweet spot for flexibility and certainty of being able to reach it. Therefore, to preserve the coherence of our measurements and to isolate behaviors mostly to γ_e, we want to minimize dephasing noise due to the flux line. The procedure for measuring the $1/f$ flux noise amplitude is as follows [74]: (i) we measure the frequency of the qubit as a function of input flux Φ, and normalize it by the flux quanta Φ_0. We then take the derivative of this to obtain the slope $\frac{1}{2\pi}\frac{\partial\omega}{\partial\Phi}$. (ii) we perform a Ramsey echo (Γ_{2E}) and T_1 ($T_1 = 1/\gamma_1$) sequence to obtain the pure dephasing rate $\Gamma_\phi = \Gamma_{2E} - \gamma_1/2$. Γ_ϕ is plotted as a function of the slope $\frac{1}{2\pi}\frac{\partial\omega}{\partial\Phi}$. Using the relationship $\Gamma_\phi = \sqrt{A_\Phi \ln 2}|\frac{\partial\omega}{\partial\Phi}|$, we can obtain the flux noise amplitude $\sqrt{A_\Phi}$. Initial measurements on unfiltered DC lines using this process gave $\sqrt{A_\Phi} \simeq 152,000\ \mu\Phi_0$. To improve this, we added a Gateway Electronics low pass filter (GQE-LPF-D) with $f_c = 20$ kHz to the 4K stage for the DC wires to pass through, bringing $\sqrt{A_\Phi} \simeq 3\ \mu\Phi_0$. This number is near the lowest reported in literature for this SQUID loop perimeter size of $\sqrt{P} = 10.22\ \mu\text{m}^{1/2}$ [74]. The following experiments are performed with a QDevil QFilter with cutoff frequency of $f_c = 65$ kHz. This filter gives a flux noise amplitude of $\sqrt{A_\Phi} \simeq 25\ \mu\Phi_0$.

2.3.4 Exceptional points and phase transitions

Now that the non-Hermiticity is engineered and we can perform three state readout, we can begin by verifying that the dynamics match the Hamiltonian eigenvalues and that we can

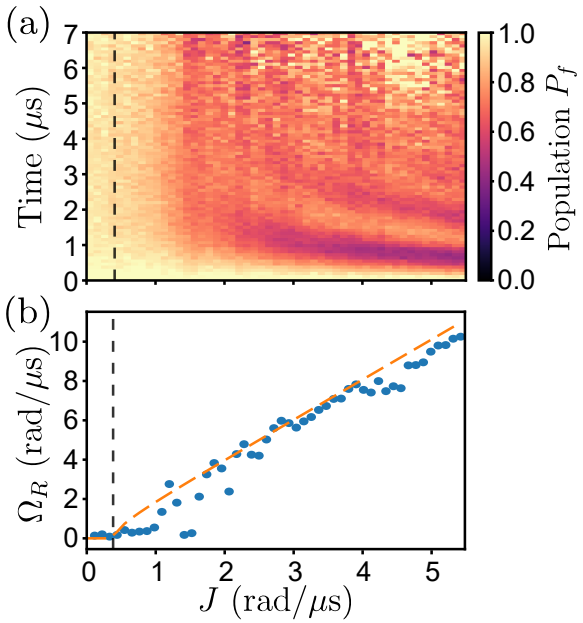

Figure 2.9: **Transition across the EP.** (a) Population of the normalized $|f\rangle$ plotted as a function of time as J is varied. The black dashed line indicates the EP at $J_{\text{EP}} = 0.4075$ rad/μs as calculated by $\text{T}_{1e} = 1/\gamma_e$ and $\text{T}_{1f} = 1/\gamma_f$ sequences. (b) The Rabi oscillations are fit to a sine decay and frequency Ω_R is extracted. The real part of the difference of the eigenvalues (2.7) Re$[\delta\lambda]$ is plotted as the dashed orange line.

observe the two regions of $\mathcal{PT}$-symmetry. The dynamics of the qubit depend on $\delta\lambda = \lambda_+ - \lambda_-$ because $|f\rangle$ can be written as a superposition of both the eigenstates $|\lambda_\pm\rangle$ [20]. To observe the phase transition that occurs between the unbroken and broken regimes we will sweep J while driving on resonance ($\Delta = 0$). First we prepare the qubit in the $|f\rangle$ state and then turn on a drive with strength J. The result is Rabi oscillations at some frequency Ω_R (Fig. 2.9a). We extract this by fitting the normalized population of $|f\rangle$, P_f, to a sine decay $A\sin(\Omega_R t)e^{-\gamma_R t} + D$ (Fig. 2.9a). What we see here is a transition at the EP (black dashed line) from the region of broken $\mathcal{PT}$-symmetry where $\Omega_R \approx 0$ to the region of unbroken $\mathcal{PT}$-symmetry where $\Omega_R > 0$ with the square root dependence. The difference of the real part of the eigenvalues dictates the frequency of oscillations and is plotted in the orange dashed line. When the real part goes to zero, we observe pure decay of the population.

The discovery and observation of EPs has been an exciting avenue of research, particularly due to the square root dependence leading up to it. This allows for greater sensitivity and amplification in making measurements, since a small number under a square root is not as small (e.g. $\sqrt{0.01} = 0.1$). There have since been experiments performed that make accurate

measurements due to this property [75, 76]. Another theoretically explored benefit is speed up of entanglement near exceptional points [77, 24].

2.3.5 Explorations of the topology

The dependence of the complex eigenvalues (2.7) on Δ and J form what are called Riemann sheets. A feature of these sheets is that they connect between the two EPs as branch cuts on both the real and imaginary sheets (Fig. 2.10a,b). Each color on the sheet corresponds to one of the two eigenstates. This branch cut offers a route to continuously and smoothly switch between eigenstates (as indicated by the yellow trace) on both the real and imaginary sheets. This route is referred to as encircling the exceptional point. If the parameters are adiabatically varied in a closed loop around an EP, such that the qubit state is the instantaneous state of the Hamiltonian, the state is transported into the other. The notion and limit of adiabaticity will be discussed in Section 3.1. This behavior has been explored on a variety of platforms such as optomechanical [15, 21], optics [22, 23, 24], NV centers in diamond [25], photonics [26], nano-oscillators [27], and superconducting qubits [16]. In addition to the behavior predicted by the Riemann sheets, there is a chirality observed in the population transfer. For a given initial state, the encircling direction gives a different result in which the state transfer is only completed in one direction. This behavior is a result of the imaginary component of the eigenstates. In certain encircling directions, the path follows the eigenstate with more loss, adiabaticity breaks down, and the gain state is amplified as loss is accumulated [78, 16, 79, 15].

In Figure 2.10c and d, for a loop time of T and time t, encircling in the clockwise $\circlearrowright$ and counterclockwise $\circlearrowleft$ directions takes the specific form of:

$$\begin{aligned} J(t) &= \frac{J_{\max} - J_{\min}}{2} \cos\left(\frac{2\pi t}{T}\right) + \frac{J_{\max} + J_{\min}}{2}, \\ \Delta(t) &= \Delta_{\circlearrowright,\circlearrowleft} \sin\left(\frac{2\pi t}{T}\right), \end{aligned} \tag{2.26}$$

We prepare the $|\lambda_-\rangle$ eigenstate at a value of $J_{\max} = 30$ rad/μs and $\Delta = 0$. Since $J_{\max} \gg J_{\text{EP}}$, $|\lambda_-\rangle \propto |-x\rangle$. We drive with real coupling $J = J_x$ in this loop, though complex coupling will be explored in the next chapter. The loop is then varied for parameters of $T = 1.4$ μs,

$J_{\min} = 0$, and $\Delta_{\circlearrowleft,\circlearrowright} = \pm 10\pi$ rad/μs for Fig. 2.10(c,d), respectively. The instantaneous Hamiltonian H_{eff} at each time t is now dependent on these values of J and Δ. We plot the corresponding instantaneous eigenstate Pauli expectation values $\{x_{\text{I}}, y_{\text{I}}, z_{\text{I}}\}$ in Fig. 2.10(c,d) with the dashed lines. What we see for x_{I} is that as the parameters $J(t)$, $\Delta(t)$ are varied slowly, x_{I} is smoothly transferred from $\langle\sigma_x\rangle = -1$ to $\langle\sigma_x\rangle = +1$ and passes through the branch cut near the EP around $t/T = 0.5$. z_{I} is evolved close to $\langle\sigma_z\rangle = -1 = |f\rangle$ for Fig. 2.10c and $\langle\sigma_z\rangle = +1 = |e\rangle$ for Fig. 2.10d. Since we are driving with $J = J_x$ and $J_{\min} = 0$, we see that $y_{\text{I}} = 0$ for all t.

The Pauli expectation values are experimentally measured (solid lines) $\{x \equiv \langle\hat{\sigma}_x\rangle, y \equiv \langle\hat{\sigma}_y\rangle, z \equiv \langle\hat{\sigma}_z\rangle\}$ using tomography techniques (Sec. 2.3.2) and plotted alongside the simulated Pauli expectation values (dotted lines) $\{x_S, y_S, z_S = \text{Tr}[\rho\hat{\sigma}_{x,y,z}]\}$. The experimental state (solid lines) start off following the instantaneous eigenstates (dashed lines). After the halfway point around $t = 0.7$ μs, the encircling approaches the EP after which the state begins oscillating. These oscillations are due to non-adiabatic couplings between the eigenstates that manifest as we approach the small energy gap, $\delta\lambda$, near the EP too quickly. The following section (Sec. 3.1) will describe in detail the condition of adiabaticity and how it leads to this breakdown. The state also ends in a mixed state due to loss of coherence due to dissipation and dephasing. In dissipative quantum systems, there is a trade-off of varying parameters slow enough to satisfy adiabaticity, and fast enough to mitigate losses due to the relaxation rates $\gamma_{k,\phi}$. The following chapter will aim to solve both of these issues while maintaining the topology of the complex energy spectrum using shortcuts to adiabaticity.

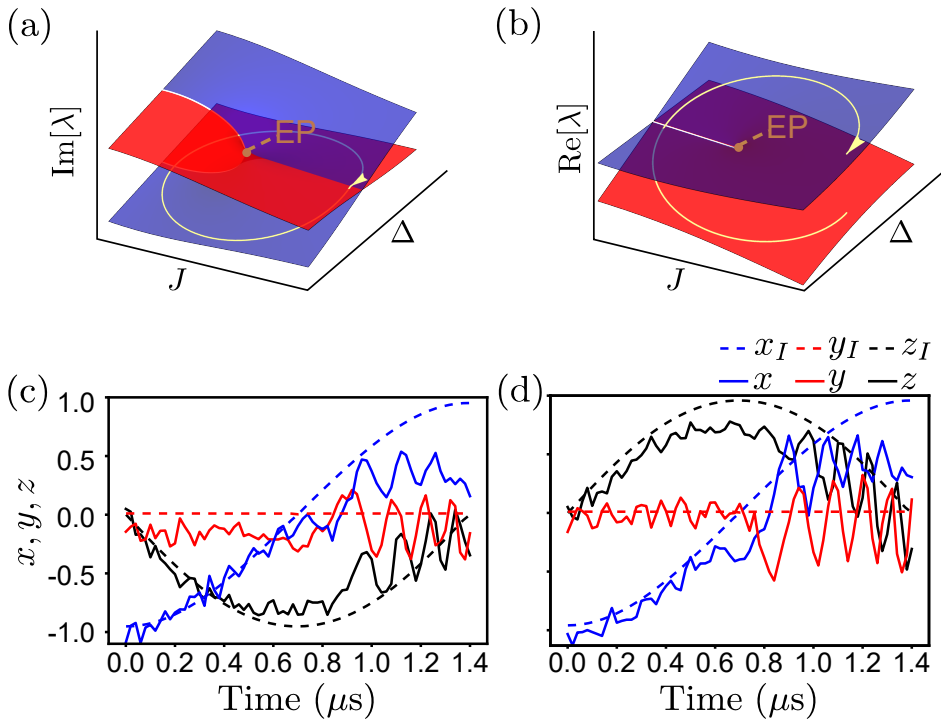

Figure 2.10: **Riemann sheets and encircling the exceptional point.** (a-b) The imaginary and real parts of the eigenvalues plotted as a function of Δ and J. The exceptional point at $J_{\mathrm{EP}} = \gamma/4$ is indicated as the orange circle. The yellow trace shows a loop that encircles the EP and passes through the branch cut. (c-d) This encircling is performed experimentally for 1.4 μs in both the clockwise and counterclockwise directions for a value of $|\Delta_{\mathrm{max}}| = 10\pi$ rad/μs. The Pauli expectation values x, y, z are calculated from the state population. The instantaneous eigenstates of the Hamiltonian are plotted with dashed lines: $x_{\mathrm{I}}, y_{\mathrm{I}}, z_{\mathrm{I}}$.

Chapter 3

Shortcuts to Adiabaticity and Counterdiabatic Control of a Non-Hermitian qubit

The following chapter will explore the how adiabaticity can be extended to non-Hermitian Hamiltonians and how we can overcome the challenges associated with the complex energy spectrum. Section 3.1 will go over the condition of adiabaticity in our relevant system and parameter path. As shown in the previous section, attempting to drive adiabatically in a lossy system results in decoherence to a mixed state or oscillations due non-adiabatic deformations from driving too fast. Therefore, in Section 3.2 we show how we can obtain a drive that keeps us close to the instantaneous eigenstates using shortcuts to adiabaticity. In Section 3.3 we implement these drives on a superconducting qubit to explore the complex energy spectrum of a non-Hermitian Hamiltonian and explore the limits of the protocol through theoretical analysis and further experiments. The work presented in these previous sections includes work published in [80]. In Section 3.4 we evaluate another method that guarantees Hermitian drives when focusing on the eigenstate subspace the system was initialized in.

3.1 Adiabaticity in quantum systems

Adiabaticity in quantum systems offers avenues of robust control. The adiabaticity theorem states that if a state is prepared in an eigenstate of the system, and the parameters are varied adiabatically (and doesn't cross any degeneracies), the system will remain in that eigenstate, up to a phase [18, 19]. An interesting consequence of driving a system adiabatically for a Hermitian system is that it allows boundary conditions to be set using the Hamiltonian.

This means that not every step along a parameter path will matter, as long as it is driven adiabatically, the state population will only depend on the initial and final Hamiltonian. This provides a unique robustness to quantum state preparation. A common use of adiabaticity is in cases where a system is driven with a time-dependent Hamiltonian of which the ground state of the final Hamiltonian is the desired state. For example, demonstrating quantum speedup in combinatorial problems using Rydberg atom arrays [17].

The adiabatic basis of a quantum system refers to the time-independent "frozen" picture of the Hamiltonian, a.k.a, the instantaneous Hamiltonian. If a system is initialized in one of these instantaneous eigenstates, and driven slowly enough, it should remain in that eigenstate (up to a phase). For a time-dependent Hamiltonian $H(t)$ we have its instantaneous eigenstates and eigenvalues: $H(t)|\lambda_n(t)\rangle = \lambda_n(t)|\lambda_n(t)\rangle$. As is valid for paths we explore in this thesis, the evolution is closed loop with with loop time T and $H(0) = H(T)$. The adiabatic approximation of the state $|\psi(t)\rangle$ will be the eigenstate $|\lambda_n(t)\rangle$ multiplied by some phases Eq. (3.1). The first phase is path dependent and is commonly known as the dynamical phase. The second phase θ_B can be solved for from the Schrödinger equation (where $\dot{f(t)} = \partial_t f(t)$):

$$|\psi(t)\rangle = e^{-i\int_0^t dt'\lambda_n(t')} e^{i\theta_B(t)} |\lambda_n(t)\rangle. \tag{3.1}$$

We write $\theta_D = -\int_0^t dt'\lambda_n(t')$ and drop (t) for legibility.

$$H(t)|\psi(t)\rangle = i|\dot{\psi}(t)\rangle, \tag{3.2}$$
$$e^{i\theta_D}e^{i\theta_B}\lambda_n|\lambda_n\rangle = i[-i\lambda_n e^{i\theta_D}e^{i\theta_B}|\lambda\rangle + e^{i\theta_D}i\dot{\theta}_B e^{i\theta_B}|\lambda\rangle + e^{i\theta_D}e^{i\theta_B}|\dot{\lambda}\rangle], \tag{3.3}$$
$$e^{i\theta_D}e^{i\theta_B}\lambda_n|\lambda_n\rangle = i(e^{i\theta_D}e^{i\theta_B})[-i\lambda_n|\lambda\rangle + i\dot{\theta}_B|\lambda\rangle + |\dot{\lambda}\rangle], \tag{3.4}$$

multiply $\langle\lambda_n|$ from the left and cancel like terms:

$$\lambda_n = i(-i\lambda_n + i\dot{\theta}_B + \langle\lambda_n|\dot{\lambda_n}\rangle), \tag{3.5}$$
$$\dot{\theta}_B = i\langle\lambda_n|\dot{\lambda_n}\rangle). \tag{3.6}$$

Therefore, this adiabatic approximation encodes geometric information in $\langle\lambda_n(t)|\partial_t\lambda_n(t)\rangle$ as the vector potential. This is the integrand that leads to the geometric phase that is accumulated for closed loop evolution [81, 82]:

$$\theta_B(T) = i \int_0^T dt \langle \lambda_n(t) | \partial_t \lambda_n(t) \rangle. \tag{3.7}$$

The final state at time T in the adiabatic limit is:

$$|\psi_n(T)\rangle = e^{-i \int_0^T dt \lambda_n(t) - \int_0^T dt \langle \lambda_n(t) | \partial_t \lambda_n(t) \rangle} |\lambda_n(T)\rangle. \tag{3.8}$$

3.1.1 Notion of adiabaticity for open quantum systems

How slow is slow enough? An elegant proof of the adiabaticity condition can be read in [83]. The coefficients describing the state as a linear combination of eigenstates,

$$|\psi(t)\rangle = \sum_n c_n(t) e^{i(\theta_D(t) + \theta_B(t))} |\lambda_n\rangle, \tag{3.9}$$

can be substituted into the Schrödinger equation. Through algebraic manipulation, this yields conditions under which the state evolves adiabatically, characterized by constant populations: $|c_m(0)|^2 = |c_m(t)|^2$. Meaning that a state prepared in an eigenstate $|\lambda_m\rangle$ remains in $|\lambda_m\rangle$: $|c_m(0)|^2 = 1, |c_m(t)|^2 \approx 1$. This means that for a state $n \neq m$, it begins with probability $|c_n(0)|^2 = 0$, later at time t the probability must satisfy $|c_n(t)|^2 \ll 1$. This final inequality is the basis for the adiabaticity condition and thus limits transitions to the *other* eigenstate. During the derivation of the Hermitian adiabaticity condition, there are assumptions made that don't hold for non-Hermitian systems. For example, that $|e^{i \int_0^t \lambda_m(t') - \lambda_n(t')) dt'}|$ contributes a value of 1 when the eigenvalues are real, since the magnitude $|e^{ix}| = 1$ for real x.

For non-Hermitian systems, we have a complex x, therefore we need to take care with accounting for the gain and loss present in the eigenstates and eigenvalues due to the imaginary components. As seen in Section 2.3.5 and with the chirality in past experiments [78, 16, 79, 15], there is an asymmetric breakdown in whether the state remains in the instantaneous eigenstate. We can quantify this amount by taking into account the imaginary component of the eigenstates over the loop duration: $I_{nm} \equiv \text{Im}\left[\int_0^t (\lambda_m(t') - \lambda_n(t')) dt'\right]$ [50].

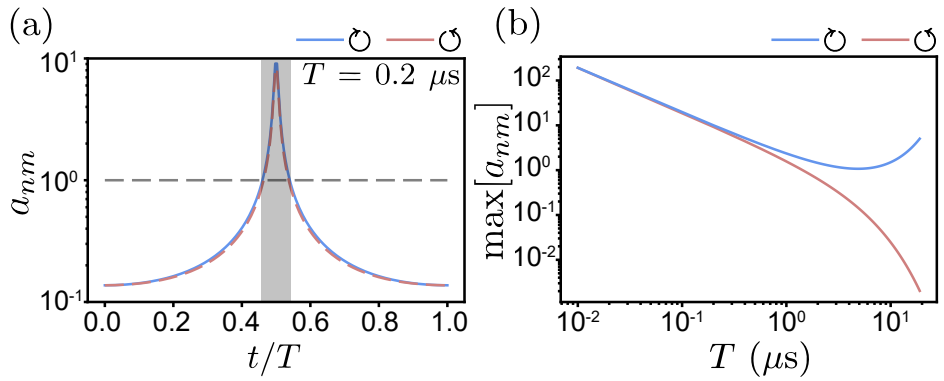

Figure 3.1: **Adiabaticity condition of non-Hermitian systems near an EP** (a) The adiabaticity condition a_{nm} (3.10) plotted for $T = 0.2$ μs with the region exceeding 1 shaded in gray. (b) The maximum of a_{nm} is plotted for both encircling directions as the total variation time T is increased. The clockwise encircling (blue) diverges due to encircling along the Riemann sheet with more loss. The counterclockwise (pink) follows the path with relative gain.

Due to some approximations taken to simplify the condition, we rename our adiabaticity criterion to be $a_{nm} \ll 1$, where $a_{nm} \approx |c_n(t)|$, thus still minimizing the probability of transition to the other eigenstate $|\lambda_n\rangle$.

$$a_{nm} = \frac{|\langle \hat{\lambda}_n(t)|\partial_t \lambda_m(t)\rangle|}{|\lambda_n(t) - \lambda_m(t)|} e^{-I_{nm}(t)} \ll 1, \tag{3.10}$$

This equation has two important factors: the first one comes from the Hermitian adiabaticity condition and only requires the evolution to be slow enough compared to the energy gap between eigenstates. The second one comes from the imaginary component of our complex energies and shows the exponential effects of gain/loss along the path. When we vary the parameters of H_{eff} as in Eqs. (2.26), the eigenstates $|\lambda_n\rangle$ and eigenvalues λ_n change accordingly. We plot this condition for an encircling loop where $J > J_{\text{EP}}$, $\Delta = 0$ and $T = 0.2$ μs in Figure 3.1a [80]. The gray dashed line is drawn at $a_{nm} = 1$ for reference of the condition requirement. We see that $a_{nm} < 1$ in the beginning and end of the loop. However, around the center of the loop ($t/T = 0.5$), the condition exceeds 1. This is due to the fact that in the EP encircling loop, the center of the loop is when the eigenvalue gap becomes smaller (denominator of Eq. (3.10)). This increases the value of a_{nm} and requires even slower driving to satisfy adiabaticity. This rapid increase of a_{nm} when near the EP provides the reason for the rapid breakdown in Figure 2.10c and d after $t/T = 0.5$. Since the

maximum value (and region around it) ultimately determines whether there is a breakdown in adiabaticity, we can take the maximum of a_{nm} and sweep the control time T. This is calculated for the same initial eigenstate and with $\Delta_{\circlearrowleft}$ and $\Delta_{\circlearrowright}$ in Figure 3.1b. We see that for both encircling directions $\max[a_{nm}]$ follows a power law form of $1/T$ for short T due to the first factor of Eq. (3.10). At long T, we see that the exponential term begins to dominate and the encircling directions diverge from each other. The clockwise path accumulates enough loss to diverge from adiabaticity (blue), while the path with gain approaches it (pink) [84, 85]. As seen in Figure 2.10a, if the path follows the state with more loss in the clockwise direction (the lower sheet corresponding to larger negative imaginary component), adiabaticity breaks down. This exploration of a_{nm} in both encircling directions supports previous experiments that are able to observe adiabatic state transfer in the direction with relative gain [78, 16, 79, 15].

3.2 Counterdiabatic driving theory

The following section will derive a Hamiltonian to counteract these non-adiabatic effects and allow us to drive with a Hamiltonian in shorter time scales without inducing unwanted transitions, also known generally as shortcuts to adiabaticity [86, 87]. The specific control method we use is called counterdiabatic driving [29, 28, 88, 89, 90, 91, 92, 83, 93, 94, 95, 96, 97] and allows us to achieve adiabatic response at times faster than what satisfies Eq. (3.10). Before delving into the mathematical formalism, consider an intuitive analogy: a waiter carrying a tray of drinks with leaky glasses. The waiter faces a fundamental tradeoff: he must transport the tray from point A to point B as quickly as possible, but each glass has small holes that allow liquid to continuously leak out. If the waiter moves slowly and cautiously, taking gentle turns around obstacles, the glasses remain perfectly stable and upright. However, this leisurely pace comes at a cost: by the time he reaches the destination, most of the liquid has leaked away through the holes. Conversely, if he rushes directly toward point B, he can minimize the leakage time, but his rapid movements and sharp turns around obstacles will cause the glasses to tip and shift. The solution lies in counterdiabatic driving. By anticipating the forces that his rapid movements will exert on the tray, the waiter can preemptively adjust his grip and tray angle to counteract these destabilizing influences. This allows him to maintain both speed and stability: he reaches point B quickly while preserving the maximum amount of liquid. This physical intuition directly parallels

the quantum mechanical principle, where the "liquid" represents the state population and coherence we wish to preserve and the "counteracting forces" are the additional control fields that maintain adiabatic evolution even during rapid parameter variation.

3.2.1 Reverse engineering to achieve the adiabatic state

The method to derive this control Hamiltonian is called "reverse engineering" [29]. We start with the state explained in Sec. 3.1, Eq. (3.1), as our desired final state. Now we bring back the Schrödinger equation to solve for H_t based on this state:

$$i|\dot{\psi}(t)\rangle = H_t|\psi(t)\rangle. \tag{3.11}$$

We can define any unitary operator satisfies the Schrödinger equation as:

$$i\hat{U}(t) = H_t\hat{U}(t), \tag{3.12}$$

$$H_t = i\dot{\hat{U}}(t)\hat{U}^\dagger \tag{3.13}$$

$$\hat{U}(t) = \sum_n \exp\{-i\int_0^t dt'\lambda_n(t') - \int_0^t dt'\langle\lambda_n(t')|\dot{\lambda}_n(t')\rangle\}|\lambda_n(t)\rangle\langle\lambda(0)|. \tag{3.14}$$

This gives us the Hamiltonian:

$$H_t = \sum_n |n\rangle\lambda_n\langle\lambda| + i\sum_n(|\partial_t\lambda_n\rangle\langle\lambda_n| - \langle\lambda_n|\partial_t\lambda_n\rangle|\lambda_n\rangle\langle\lambda_n|). \tag{3.15}$$

Further observation of this new Hamiltonian shows us that it is the addition of our original Hamiltonian with some new components $H_t = H_{\text{eff}} + H_{\text{CD}}$:

$$H_{\text{CD}}(t) = i\sum_{n\in\pm}|\partial_t\lambda_n(t)\rangle\langle\lambda_n(t)| - \langle\lambda_n(t)|\partial_t\lambda_n(t)\rangle|\lambda_n(t\rangle\langle\lambda_n(t)|. \tag{3.16}$$

$H_{\text{CD}}(t)$ is now an additional drive that is applied along with the parameters of $H_{\text{eff}}(t)$. The first term of H_{CD} accounts for the non-adiabatic transitions out of the eigenstate when tuned at a certain rate. The second term has the integrand to the Berry phase (3.7), called the Berry connection, and is therefore related to the geometry of the parameters [81].

3.2.2 Non-Hermitian counterdiabatic drive

As mentioned in Section 2.1.2, we need to take care when defining our eigenstates and operators in a non-Hermitian setup due to bi-orthogonality. The previous derivation can be extended to a non-Hermitian system using the left eigenstate for the "bra" states $\langle\hat{\lambda}_n|$ [49]:

$$H_{\text{CD}}(t) = i\sum_{n\in\pm} |\partial_t\lambda_n(t)\rangle\langle\hat{\lambda}_n(t)| - \langle\hat{\lambda}_n(t)|\partial_t\lambda_n(t)\rangle|\lambda_n(t\rangle\langle\hat{\lambda}_n(t)|. \tag{3.17}$$

To understand this counterdiabatic drive Hamiltonian for our system better, it is useful to dive deeper into the decomposition of the eigenstates previously defined in Section 2.1.1 as Eqs. (2.8) and (2.9). The defined angle $\alpha = \arctan\frac{|J|}{\Delta/2-i\gamma/4}$ is referred to as the complex mixing angle and can be decomposed as $\alpha = \alpha_{\text{R}} + i\alpha_{\text{I}}$. The non-orthogonality of our non-Hermitian eigenstates is determined by the imaginary part, called the hyperbolic angle, α_{I}. When $\alpha_{\text{I}} = 0$, the eigenstates are orthogonal. When $\alpha_{\text{I}} \neq 0$, we can define the eigenstate overlap as $\langle\lambda_-|\lambda_+\rangle = \langle\hat{\lambda}_-|\hat{\lambda}_+\rangle = i\sinh\alpha_{\text{I}}$ and norm as $\langle\lambda_\pm|\lambda_\pm\rangle = \langle\hat{\lambda}_\pm|\hat{\lambda}_\pm\rangle = \cosh\alpha_{\text{I}}$ [80].

Now that we've defined this complex mixing angle, it follows that there should be a rotation corresponding to this angle to obtain our eigenstates which we will call $\hat{C}_y(\alpha)$. This is a rotation around the y-axis of the Bloch sphere applied to $|e\rangle, |f\rangle$. So we can define the eigenstates as $|\lambda_\pm\rangle = \hat{C}_y(\alpha)|e/f\rangle$. Since α has two components to it, we can further decompose this rotation into:

$$\hat{C}_y(\alpha) \equiv e^{-i\frac{\alpha}{2}\hat{\sigma}_y} = e^{-i\frac{\alpha_{\text{R}}}{2}\hat{\sigma}_y}e^{\frac{\alpha_{\text{I}}}{2}\hat{\sigma}_y} \equiv \hat{R}_y(\alpha_{\text{R}})\hat{B}_y(\alpha_{\text{I}}). \tag{3.18}$$

We can connect this rotation to our dynamics by considering the steps taken in discrete time steps $t_0 \to t$ in the form of a transport operator: $\hat{T}(t,t_0) = \hat{C}_y(\alpha_t)\hat{C}_y(-\alpha_{t_0}) = e^{-\frac{i}{2}(\alpha_t-\alpha_{t_0})\hat{\sigma}_y}$. This essentially shows how if I want to create the eigenstate at time t with α_t, I can undo the

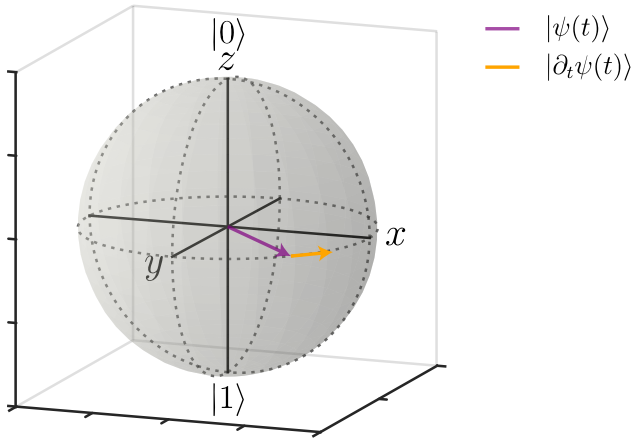

Figure 3.2: **Parallel transport** An example of a state $|\psi(t)\rangle$ in purple and its derivative in $|\partial_t\psi(t)\rangle$ in yellow.

rotation of the eigenstate at t_0 with $\hat{C}_y(-\alpha_{t_0})$, and then apply the new rotation $\hat{C}_y(\alpha_t)$. Since this describes our time dependent dynamics, we can also obtain this from the Hamiltonian $\hat{T}(t,t_0) \equiv e^{-i\int_{t_0}^{t} H_{\text{CD}}(s)ds}$. We can equate these two definitions and obtain:

$$H_{\text{CD}}(t) = \frac{\dot{\alpha}_t}{2}\hat{\sigma}_y. \tag{3.19}$$

From equation (3.18), we can see that $|\partial_t\lambda_\pm\rangle = -i\frac{\dot{\alpha}_t}{2}\hat{\sigma}_y|\lambda_\pm\rangle$. Multiplying this out we get:

$$\sigma_y|\lambda_+\rangle = \begin{pmatrix} 0 & -i \\ i & 0 \end{pmatrix}\begin{pmatrix} \cos\alpha/2 \\ \sin\alpha/2 \end{pmatrix} = \begin{pmatrix} -i\sin\alpha/2 \\ i\cos\alpha/2 \end{pmatrix} = i|\lambda_-\rangle \tag{3.20}$$

Plugging this back in, we now see that $|\partial_t\lambda_\pm\rangle = \frac{\dot{\alpha}_t}{2}|\lambda_\mp\rangle$. This means that, according to the biorthogonal properties from Sec. 2.1.2, $\langle\hat{\lambda}_\pm|\partial_t\lambda_\pm\rangle = \langle\hat{\lambda}_\pm|\lambda_\mp\rangle = 0$. This expression removes the second term of Eq. 3.17 and shows parallel transport because a change in time of an eigenstate produces a vector that is orthogonal to the unchanged eigenstate and can be viewed in Figure 3.2 for a general time varying state $|\psi\rangle$. This is not generally true for cases of complex coupling: $J = J_x + iJ_y = |J|e^{i\phi}$ and general definitions will be defined later in Section 3.3.3.

Using the completeness theorem from Sec. 2.1.2, we can reduce Eq. (3.17) to Eq. (3.19) using the definition of $|\partial_t \lambda_\pm\rangle$. (We drop the time dependence (t) for legibility)

$$H_{\mathrm{CD}} = i \sum_{n\in\pm} |\partial_t \lambda_n\rangle\langle\hat{\lambda}_n| \tag{3.21}$$

$$H_{\mathrm{CD}} = i \sum_{n\in\pm} -i\frac{\dot{\alpha}_t}{2}\hat{\sigma}_y |\lambda_n\rangle\langle\hat{\lambda}_n| \tag{3.22}$$

$$H_{\mathrm{CD}} = \frac{\dot{\alpha}_t}{2}\hat{\sigma}_y \sum_{n\in\pm} |\lambda_n\rangle\langle\hat{\lambda}_n| \tag{3.23}$$

$$H_{\mathrm{CD}} = \frac{\dot{\alpha}_t}{2}\hat{\sigma}_y \tag{3.24}$$

Now that we have a direct relationship between H_{CD} and α which is a complex number, H_{CD} can be non-Hermitian. So, we can decompose it into two components:

$$H_{\mathrm{CD}}(t) = H_{\mathrm{CD}}^{(\mathrm{H})} + H_{\mathrm{CD}}^{(\mathrm{AH})} \equiv \begin{pmatrix} 0 & J_{\mathrm{CD}} \\ -J_{\mathrm{CD}} & 0 \end{pmatrix} \tag{3.25}$$

Where $J_{\mathrm{CD}} = \frac{\dot{\alpha}_{\mathrm{I}}}{2} - i\frac{\dot{\alpha}_{\mathrm{R}}}{2}$. $H_{\mathrm{CD}}^{(\mathrm{H})}$ are parameters that are Hermitian and can be implemented in experiment: $\begin{pmatrix} 0 & -i\dot{\alpha}_{\mathrm{R}}/2 \\ i\dot{\alpha}_{\mathrm{R}}/2 & 0 \end{pmatrix}$. Whereas $H_{\mathrm{CD}}^{(\mathrm{AH})}$ we cannot implement because it is non-Hermitian: $\begin{pmatrix} 0 & \dot{\alpha}_{\mathrm{I}}/2 \\ -\dot{\alpha}_{\mathrm{I}}/2 & 0 \end{pmatrix}$. However, if $\dot{\alpha}_{\mathrm{I}} = 0$, meaning the imaginary part of α is constant, H_{CD} becomes Hermitian and implementable.

3.3 Implementation of counterdiabatic protocols

To demonstrate how counterdiabatic driving will allow us to complete a parameter variation faster than required by the adiabaticity condition (Eq. (3.10)), we begin with performing the encircling for a fast loop time of $T = 0.2$ μs. First we prepare the system in the $|\lambda_-\rangle$ eigenstate at $J = 30$ rad/μs and $\Delta = 0$. Then we tune the parameters of H_{eff} according to Eq. (2.26) These paths are shown in Figure 3.3a and b, for $J_{\mathrm{max}} = 30$ rad/μs, $J_{\mathrm{min}} = 0$ rad/μs, $\Delta_{\circlearrowleft} = 10\pi$ rad/μs and $\Delta_{\circlearrowleft} = -10\pi$ rad/μs, respectively. The loop time T is split up into

discrete steps ($N = 51$) such that our step size is $\delta t = T/(N-1)$. We then perform quantum state tomography and readout as described in Sec. 2.3.2 at each successive time step and obtain the experimental Pauli expectation values $\{x, y, z\}$. We show the results in Figure 3.3c and d for $\Delta_{\circlearrowleft}$ and $\Delta_{\circlearrowright}$, respectively, using solid lines [80]. The dashed lines are the instantaneous eigenstates $\{x_{\mathrm{I}}, y_{\mathrm{I}}, z_{\mathrm{I}}\}$ calculated from H_{eff} as $x_{\mathrm{I}}, y_{\mathrm{I}}, z_{\mathrm{I}} = \langle\lambda_n|\hat{\sigma}_{x,y,z}|\lambda_n\rangle$. Where $n \to -$ while $t < T/2$ and $n \to +$ while $t > T/2$. At first, we see that the experimental results are close to the instantaneous eigenstates. However, after $t > T/2 = 0.1$ μs, we see that the state deviates from the dashed lines. This can be attributed to the previous calculation of the adiabaticity condition in Fig. 3.1a where we saw that the energy gap becomes much smaller at the center of the loop and the condition is violated. Similarly, this region of extreme violation is highlighted in gray. This breakdown is due to the fact that the loop time is short, and thus the parameter variation is too fast for the system to equilibrate to the instantaneous eigenstate of its instantaneous Hamiltonian H_{eff}.

To correct for the non-adiabatic dynamics from Fig. 3.3(c,d), we add the additional drive derived earlier from Section 3.2.2. Due to a small non-Hermitian component $H_{\mathrm{CD}}^{(\mathrm{AH})}$, we can apply an approximate drive as: $\tilde{H}_{\mathrm{CD}} = \frac{1}{2}(H_{\mathrm{CD}} + H_{\mathrm{CD}}^{\dagger})$. We display the parameters from H_{CD} in Figs. 3.3(e,f). Where J_{CD} (blue trace), corresponds to the Hermitian component $H_{\mathrm{CD}}^{(\mathrm{H})}$. The experiment is repeated with the same protocol but with $H_{\mathrm{eff}} + \tilde{H}_{\mathrm{CD}}$. We show the results in Figs. 3.3(g,h) and observe that the experimental state follows the instantaneous lines closely. These results show that the state is able to smoothly follow the Riemann sheets through the branch cut to observe state transfer in either encircling direction. The system was initialized in $|\lambda_-\rangle$ and ends in $|\lambda_+\rangle$, as verified by $x(0) \simeq -1$ and $x(T) \simeq +1$.

To visualize what this looks like on the Bloch sphere, we plot both the Bloch coordinates of the system driven with H_{eff} (green trace) in Fig. 3.4a and $H_{\mathrm{eff}} + \tilde{H}_{\mathrm{CD}}$ (blue trace) in Fig. 3.4b for the results in Fig. 3.3(c,g). The instantaneous eigenstate coordinates are plotted with black dashed lines. We see how the experimental trace with counterdiabatic driving follows it closely.

3.3.1 Evaluating the success of the counterdiabatic drive

Though the success of the counterdiabatic drive is visually verified, we want to quantify this using a metric. We choose the trace distance $D(\rho_{\mathrm{I}}, \rho_{\mathrm{q}})$ to show how closely the experimentally

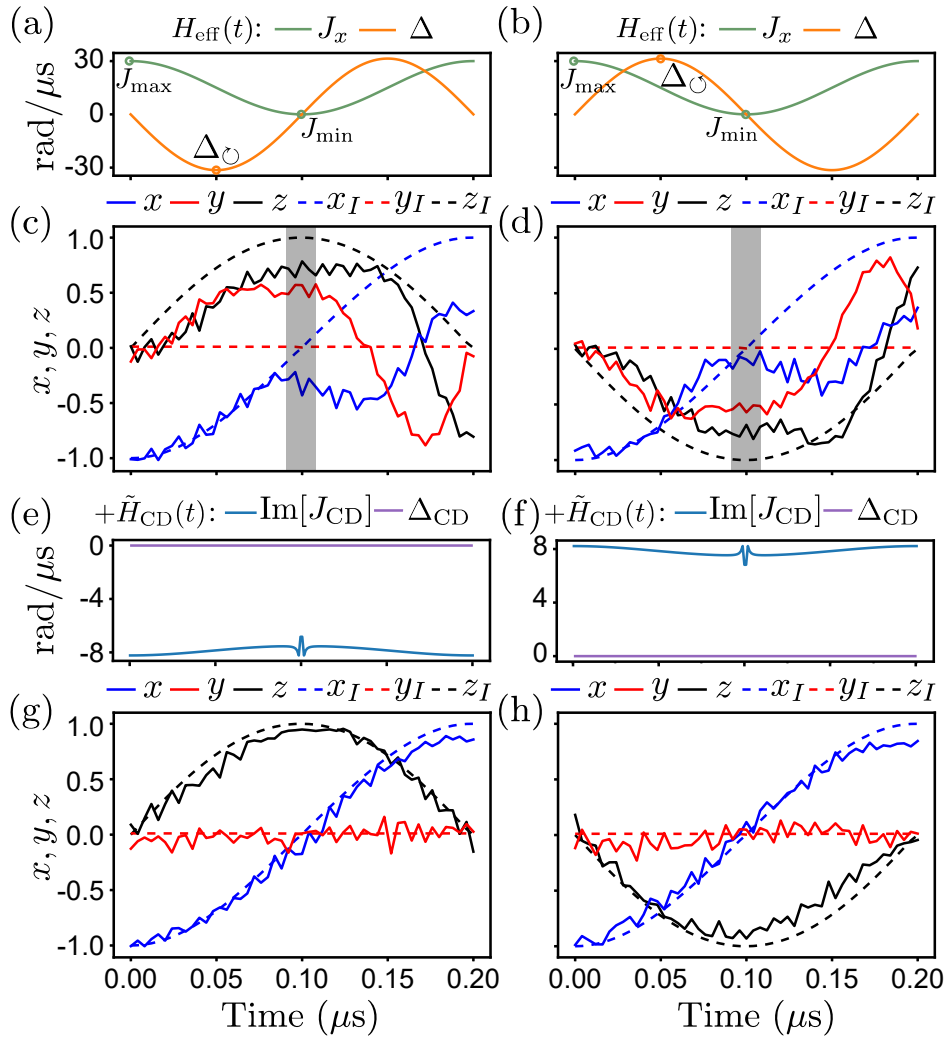

Figure 3.3: **Encircling an EP with and without counterdiabatic driving.** (a,b) $H_{\rm eff}$ time dependence according to Eq. (2.26) plotted for $T = 0.2$ μs in both encircling directions. (c,d) Pauli expectation values $\{x, y, z\}$ experimentally obtained from quantum state tomography (solid lines). The Pauli expectation values for the instantaneous eigenstates $\{x_{\rm I}, y_{\rm I}, z_{\rm I}\}$ are calculated and plotted for reference (dashed lines) The gray shaded region corresponds to the region from Fig. 3.1a where the adiabaticity parameter far exceeds the condition and therefore adiabaticity breaks down. We see that during this region is when the state begins to deviate from the instantaneous eigenstates. (e,f) The components of the approximate drive $\tilde{H}_{\rm CD}$ are plotted as a function of time for both directions. (g,h) The qubit is now driven with the total Hamiltonian that includes the counterdiabatic drive. The quantum state (solid lines) now closely follow the instantaneous eigenstates (dashed lines).

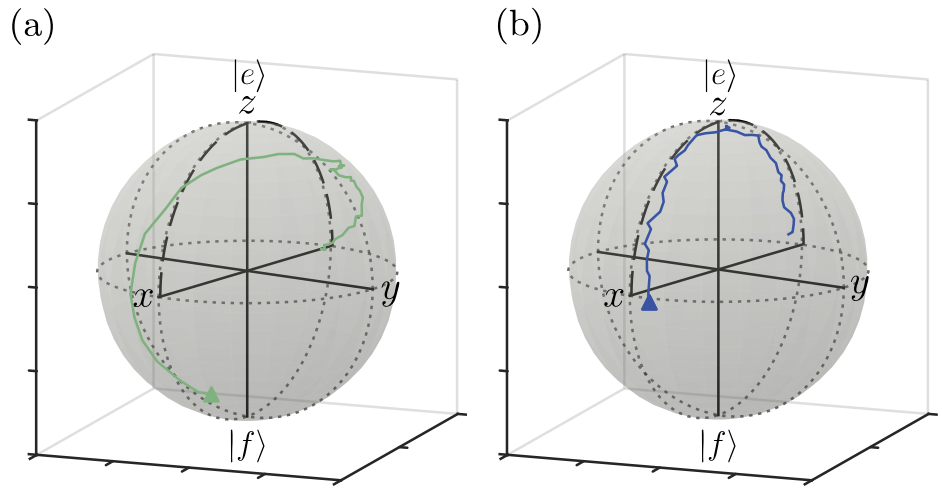

Figure 3.4: **Counterdiabatic driving result visualized on Bloch sphere** Visualizing the $\Delta_{\circlearrowright}$ encircling loop. The instantaneous eigenstates $\{x_{\mathrm{I}}, y_{\mathrm{I}}, z_{\mathrm{I}}\}$ are plotted as the black dashed lines. (a) The experimental Pauli expectation values, $\{x, y, z\}$, plotted as Bloch coordinates for H_{eff} in the green trace. (b) The experimental $\{x, y, z\}$ for $H_{\mathrm{eff}} + \tilde{H}_{\mathrm{CD}}$ plotted in the blue trace. We observe that the blue trace follows the black dashed lines much closer now.

reconstructed state ρ_{q}, follows the instantaneous eigenstate of the Hamiltonian ρ_{I} [80]. We define the density matrices as: $\rho_{\mathrm{I}} = \frac{1}{2}(\hat{I} + x_{\mathrm{I}}\hat{\sigma}_x + y_{\mathrm{I}}\hat{\sigma}_y + z_{\mathrm{I}}\hat{\sigma}_z)$ and $\rho_{\mathrm{q}} = \frac{1}{2}(\hat{I} + x\hat{\sigma}_x + y\hat{\sigma}_y + z\hat{\sigma}_z)$. The trace distance is then defined as:

$$D(\rho_{\mathrm{I}}, \rho_{\mathrm{q}}) = \frac{1}{2}\mathrm{Tr}[\sqrt{(\rho_{\mathrm{I}} - \rho_{\mathrm{q}})^{\dagger}(\rho_{\mathrm{I}} - \rho_{\mathrm{q}})}]. \tag{3.26}$$

We can see in Figure. 3.5 that the trace distance for the drive with the addition of counterdiabatic elements (blue) is much smaller than of that with the original Hamiltonian (green).

To further explore the robustness of the counterdiabatic drive, we study its dependence as a function of the encircling period T. It is now useful to calculate the average trace distance, $\overline{D}$ which is given by averaging $D(\rho_{\mathrm{I}}, \rho_{\mathrm{q}})$ over the entire loop time. The values for $T = 0.2$ μs in Figs. 3.3(c,d) $\Delta_{\circlearrowright}$ and $\Delta_{\circlearrowleft}$ are $\overline{D} = 0.411$ and 0.378, respectively. With the addition of counterdiabatic driving in Figs. 3.3(g,h), $\overline{D} = 0.086$ and $\overline{D} = 0.067$, respectively. In Figure 3.6(a,b) we plot $\overline{D}$ for encircling loop periods of $T = 0.01$ μs to $T = 2.1$ μs. The connected green squares indicate driving with $H_{\mathrm{eff}}(t)$ for both clockwise $\Delta_{\circlearrowright}$ (Fig. 3.6a) and counterclockwise $\Delta_{\circlearrowleft}$ (Fig. 3.6b). We see that as the loop period is decreased, $\overline{D}$ increases.

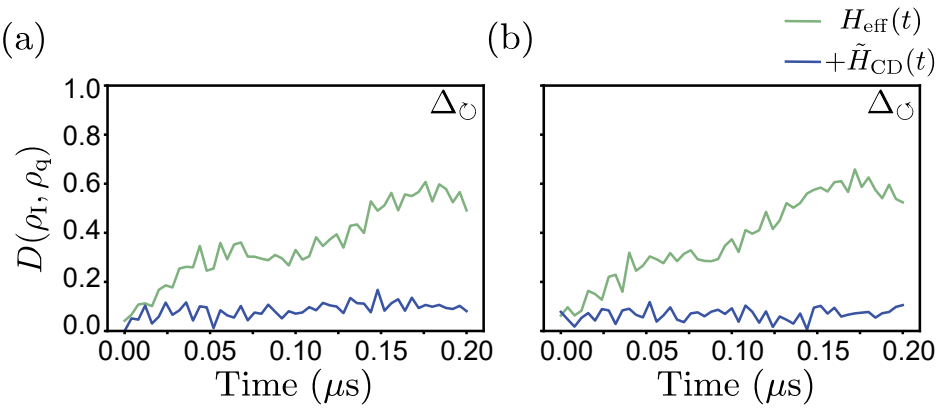

Figure 3.5: **Evaluating the efficacy of counterdiabatic driving over time.** The trace distance (3.26) calculated for the reconstructed experimental state of driving with $H_{\text{eff}}(t)$ (green) and with the addition of $\tilde{H}_{\text{CD}}(t)$ (blue) (a) from Figs. 3.3(c,g) and (b) from Figs. 3.3(d,h), respectively.

This indicates deviation of the state from the instantaneous eigenstates. We can support this by plotting (on the right axis) the adiabaticity condition $\max[a_{nm}]$ as a function of loop period with a dashed line at $a_{nm} = 1$. We see that it increases as T decreases, thereby supporting the conclusion that $\overline{D}$ increases for our evolved state at small Ts due to non-adiabatic deformations. The connected blue circles are the calculated $\overline{D}$ for driving with $H_{\text{eff}}(t) + H_{\text{CD}}(t)$. The increase in these values at short T is attributed to the experimental limitations. As the loop period is decrease, the counterdiabatic drive strength also increases. We can see this by plotting the maximum required drive strength of H_{CD}'s components in Fig. 3.6c. At $T < 0.02$ μs, the components of H_{CD} exceed the experimental limit (black dashed line). For values of $T > 0.02$ μs, we see that the $\overline{D}$ for driving with $\tilde{H}_{\text{CD}}$ are significantly lower. As T gets larger, $\overline{D}$ for $\tilde{H}_{\text{CD}}$ in blue circles approaches the green squares for H_{eff} and levels out at about $\overline{D} \approx 0.2$. This limit is due to decoherence and quantum jumps taking place from γ_ϕ and γ_f being non-zero. We can conclude from this loop period sweep that the counterdiabatic drive is effective in faster than adiabatic timescales, allowing us to also drive with small enough T to avoid decoherence effects taking place.

Another useful and related way to compare our measured qubit state (through the experimental Bloch expectation values) is through the fidelity. The fidelity is defined as:

$$F(\rho_{\text{I}}, \rho_{\text{q}}) = \left(\text{Tr}\left[\sqrt{\sqrt{\rho_{\text{I}}}\rho_{\text{q}}\sqrt{\rho_{\text{I}}}} \right] \right)^2 \tag{3.27}$$

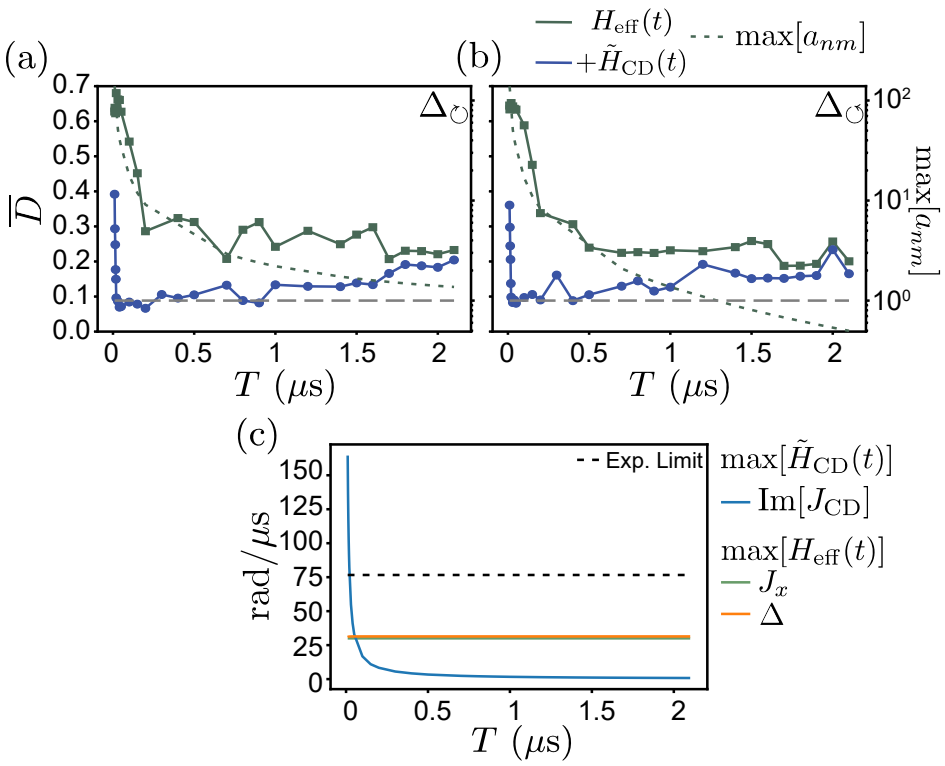

Figure 3.6: **Evaluating the success of counterdiabatic driving.** Average trace distance, $\overline{D}$, is evaluated for loops of different T. The encircling loop is varied with $J_{\max} = 30$ rad/μs and $J_{\min} = 0$ rad/μs. It is varied in both encircling directions with (a) $\Delta_{\circlearrowleft} = 10\pi$ rad/μs and (b) $\Delta_{\circlearrowleft} = 10\pi$ rad/μs. The green squares correspond to $\overline{D}$ for evolution under H_{eff} and the blue circles correspond to evolution under $H_{\text{eff}} + \tilde{H}_{\text{CD}}$. The adiabaticity condition, $\max[a_{nm}]$, is plotted on the right axis as a function of T (dashed green line) with $\max[a_{nm}] = 1$ noted with a gray dashed line. (c) The maximum value of each Hamiltonian drive component is plotted versus time T for $H_{\text{eff}}(t)$ and $\tilde{H}_{\text{CD}}(t)$. The experimental limitation on drive amplitude is plotted with a black dashed line.

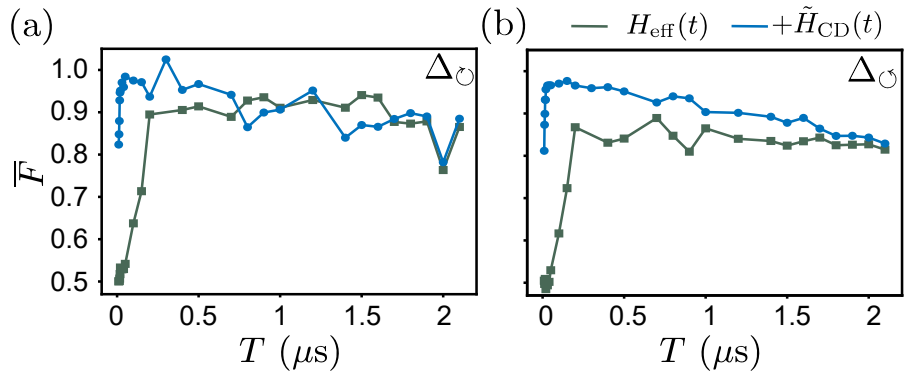

Figure 3.7: **Evaluating the counterdiabatic drive using fidelity.** The average of Eq. (3.27), $\overline{F}$, is plotted as a function of T for both encircling directions. Parameters are the same as in Fig. 3.6.

Where ρ_{q} is the density matrix of our qubit state and ρ_{I} is the density matrix of our instantaneous eigenstate. The average fidelity, $\overline{F}$, is Eq. (3.27) averaged over all time steps in a loop. The relationship of fidelity to the previously used trace distance $\text{D}(\rho, \sigma)$ is:

$$1 - \sqrt{F(\rho_{\text{I}}, \rho_{\text{q}})} \leq D(\rho_{\text{I}}, \rho_{\text{q}}) \leq \sqrt{1 - F(\rho_{\text{I}}, \rho_{\text{q}})} \tag{3.28}$$

The upper bound is only true when the state is a pure state [98].

3.3.2 Defining Apollonius circles and parameter space relationships

This next section will explore why we were able to apply H_{CD} given that $\dot{\alpha}_t$ is generally complex [80]. The previous encircling loops resulted in a Hermitian drive because of a condition where $\dot{\alpha}_{\text{I}} = 0$. This means that the non-orthogonality of our eigenstates are constant throughout the loop. We can explore our parameter space further by defining a complex variable $\varepsilon = \Delta/2 + iJ$. We can redefine $\alpha = \arctan\left(\frac{|J|}{\Delta/2 - i\gamma/4}\right)$ in terms of the parameter space ε using the relationship between arctan and log for complex numbers z:

$$\arctan(z) = \frac{i}{2}\log\left(\frac{1-iz}{1+iz}\right) \tag{3.29}$$

$$z = \frac{J}{\Delta/2 - i\gamma/4} \tag{3.30}$$

Since J is real:

$$\tag{3.31}$$

$$\alpha = \frac{i}{2}\log\left(\frac{1 - i\frac{J}{\Delta/2-i\gamma/4}}{1 + i\frac{J}{\Delta/2-i\gamma/4}}\right) \tag{3.32}$$

$$= \frac{i}{2}\log\left(\frac{\Delta/2 - i\gamma/4 - iJ}{\Delta/2 - i\gamma/4 + iJ}\right) \tag{3.33}$$

$$= \frac{1}{2i}\log\left(\frac{\Delta/2 - i\gamma/4 + iJ}{\Delta/2 - i\gamma/4 - iJ}\right) \tag{3.34}$$

$$= \frac{1}{2i}\log\left(\frac{\varepsilon - i\gamma/4}{\varepsilon^* - i\gamma/4}\right) \tag{3.35}$$

We can now take this reformulation of $\alpha(\varepsilon)$, which is dependent on the complex parameter space, and define the real and imaginary parts of it using properties of complex numbers $z = |z|e^{i\theta}$ and $\log(z) = \log(|z|) + i\arg(z)$:

$$\alpha_R(\varepsilon) = \frac{1}{2}\left(\arg\frac{\varepsilon - i\gamma/4}{\varepsilon^* - i\gamma/4}\right) = \frac{1}{2}\left(\arg(\varepsilon - i\gamma/4) + \arg(\varepsilon + i\gamma/4)\right) \tag{3.36}$$

$$\alpha_I(\varepsilon) = -\frac{1}{2}\left(\log\left|\frac{\varepsilon - i\gamma/4}{\varepsilon^* - i\gamma/4}\right|\right) = \frac{1}{2}\left(\log\left|\frac{\varepsilon + i\gamma/4}{\varepsilon - i\gamma/4}\right|\right) \tag{3.37}$$

$$\tag{3.38}$$

using the property that $|\omega| = |\omega^*|$ we can equate $|\varepsilon^* - i\gamma/4| = |\varepsilon + i\gamma/4| = |(\varepsilon + i\gamma/4)^*|$. Since the counterdiabatic drive depends on $\dot{\alpha}_t$, we look at the derivatives of these expressions. As noted in the earlier section, our drive is only Hermitian (and implementable) if $\dot{\alpha}_\mathrm{I} = 0$. Therefore, we are looking for paths that satisfy:

$$\alpha_I(\varepsilon) = \frac{1}{2}\left(\log\left|\frac{\varepsilon + i\gamma/4}{\varepsilon - i\gamma/4}\right|\right) = \text{constant} \tag{3.39}$$

$$\therefore r = \left|\frac{\varepsilon + i\gamma/4}{\varepsilon - i\gamma/4}\right| = \text{constant} \tag{3.40}$$

Eq. (3.40) describes a set of points known as an Apollonius circle. They are the set of points where the ratio of the distances to $J_{\text{EP}} = \pm i\gamma/4$ is constant and are illustrated in gray circles in Figure 3.10a. Our previous encircling parameters are very near to an Apollonius circle with $r = 0.9733$ (solid gray line) which is why we had a negligible anti-Hermitian component to our counterdiabatic drive. We can derive the center c and radius R of the Apollonius circle using the definition of a circle and rearranging such that $\Delta/2 = x_c$ and $J = y_c$ correspond to (x_c, y_c) coordinates of a circle:

$$(x_c - h)^2 + (y_c - k)^2 = R^2 \tag{3.41}$$

$$x_c^2 + \left(y_c + \frac{\gamma(1+r^2)}{4(1-r^2)}\right)^2 = \left(\frac{\gamma(1+r^2)}{4(1-r^2)}\right)^2 - \frac{\gamma^2}{16}. \tag{3.42}$$

This corresponds to a center c and radius R of:

$$c = \left(\frac{\gamma}{4}\frac{1+r^2}{1-r^2}, 0\right), R = \frac{2\frac{\gamma}{4}r}{|1-r^2|}. \tag{3.43}$$

We can extract our drive parameters through the center c and radius R:

$$J_{\max} = c + (R, 0), J_{\min} = c - (R, 0), \Delta_{\circlearrowleft} = 2R \tag{3.44}$$

To look more in depth, we can show that the angle θ between the right eigenstates $|\lambda_\pm\rangle$ and their angle from the y-axis and the hyperbolic angle α_{I} share the same contour lines (i.e. $\dot{\theta} = 0$). Thus emphasizing that the non-orthogonality need be constant to yield a Hermitian

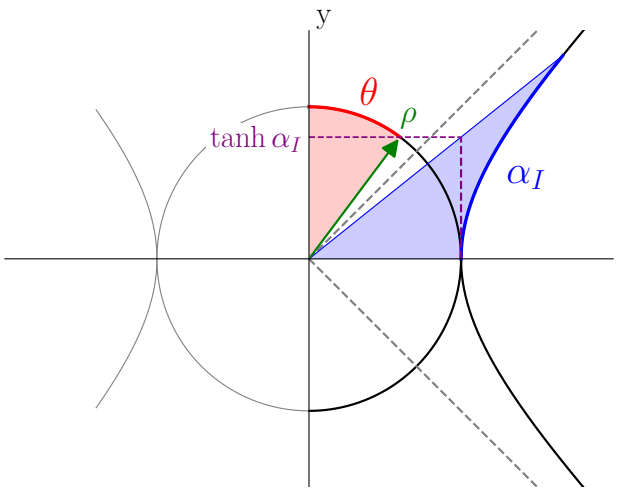

Figure 3.8: **Hyperbolic angle and y-axis.** The angle θ is the angle from the state ρ to the y-axis. α_{I} is the hyperbolic angle. θ and α_{I} are related through $\cos\theta = \tanh\alpha_{\mathrm{I}}$.

counterdiabatic drive. This can be seen from the Bloch coordinates expectation values:

$$\begin{aligned} z_{\pm} &= \mp \cos\alpha_{\mathrm{R}} \sqrt{1-\tanh^2\alpha_{\mathrm{I}}}, \\ x_{\pm} &= \mp \sin\alpha_{\mathrm{R}} \sqrt{1-\tanh^2\alpha_{\mathrm{I}}}, \\ y_{\pm} &= \tanh\alpha_{\mathrm{I}}. \end{aligned} \tag{3.45}$$

From the overlap defined before, the transition probability between normalized eigenstates is:

$$|\langle\Lambda_-|\Lambda_+\rangle|^2 = \frac{|\langle R_-|R_+\rangle|^2}{\langle R_-|R_-\rangle\langle R_+|R_+\rangle} = \tanh^2\alpha_{\mathrm{I}}. \tag{3.46}$$

We see that $\theta \equiv \arccos|\tanh\alpha_{\mathrm{I}}|$ where it can be visualized in Figure 3.8. The Bloch coordinates from Eqs. (3.45) and the Figure 3.9 show how following one Apollonius circle in parameter space is half a circle on Bloch space. In other words, for every coordinate in parameter space, there are two associated points in Bloch space. Therefore, one parameter loop brings $|\psi\rangle \to -|\psi\rangle$ and two loops brings $|\psi\rangle \to |\psi\rangle$.

These simplifications to our counterdiabatic Hamiltonian are possible due to an underlying symmetry that our effective non-Hermitian Hamiltonian has called chiral symmetry. To show

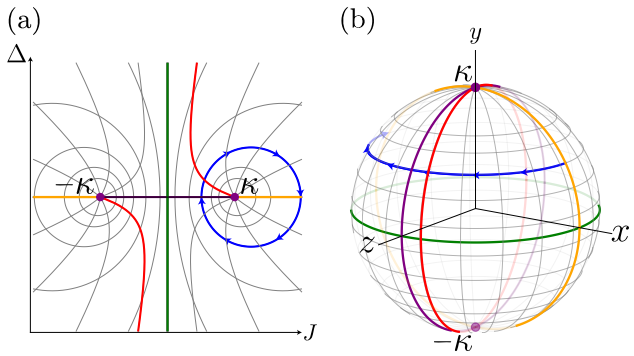

Figure 3.9: **Parameter space and Bloch coordinate state space visualization.** (a) The parameter space. (b) Bloch coordinate space (Bloch sphere) with the exceptional points $\pm\kappa = \pm J_{\mathrm{EP}}$ at the poles with the y-axis pointed up. The blue trace corresponds to encircling the exceptional point in parameter space and corresponds to a half loop in Bloch space.

this symmetry, we shift the Hamiltonian so that it is traceless:

$$H' \equiv H - \frac{1}{2}\mathrm{Tr}(H)\,\hat{I}, \tag{3.47}$$

$$\hat{\Gamma} H' \hat{\Gamma} = -H', \quad \hat{\Gamma}^2 = \hat{I}. \tag{3.48}$$

$$\tag{3.49}$$

The chiral symmetry operator is:

$$\hat{\Gamma} = \hat{R}_z(\phi)\hat{\sigma}_z\hat{R}_z^\dagger(\phi), \tag{3.50}$$

and it performs the operation: $\hat{\Gamma}|\lambda_\pm\rangle = \pm i|\lambda_\mp\rangle$. This symmetry is what allows us to define a complex mixing angle $\alpha = \alpha_{\mathrm{R}} + i\alpha_{\mathrm{I}}$.

3.3.3 Counterdiabatic generalized to complex coupling

This subsection offers a brief extension of previous derivations and definitions to the complex coupling case $J = |J|e^{i\phi}$ [80]. We can extend the definitions of the eigenstates $|\lambda_\pm\rangle$ Bloch coordinates $\{x_\pm, y_\pm, z_\pm\}$ to the rotational and hyperbolic angles α_R and α_I. Since J is complex we now consider a three-dimensional parameters space spanning (Δ, J_x, J_y). What was referred to as Apollonius *circles* is now thought of as Apollonius *tori*. The previous

definition of $\alpha = \arctan \frac{|J|}{E}$ is independent of the phase ϕ. When ϕ is varied, it corresponded to a rotation around the Δ axis in the parameter space. Since each Apollonius circle is defined by a constant α_I, as ϕ is varied these circles sweep out a toroidal surface (like a bagel).

Earlier we mentioned that parallel transport is not generally guaranteed. For $\phi \neq 0$, parallel transport only occurs for $\dot{\phi} = 0$. The eigenstates with nonzero ϕ are defined as:

$$|R_\pm\rangle = \hat{R}_z(\phi)\hat{C}_y(\alpha)|z_\pm\rangle. \tag{3.51}$$

The transport operator that transports Eq. (3.51) from time t_0 to t is now defined as:

$$\hat{T}(t, t_0) \equiv \hat{R}_z(\phi_t)\hat{C}_y(\alpha_t)\hat{C}_y(-\alpha_{t_0})\hat{R}_z(-\phi_{t_0}). \tag{3.52}$$

The Berry connection for a time-dependent ϕ is now:

$$\langle\hat{\lambda}_\pm|\partial_t\lambda_\pm\rangle = \pm i\frac{\dot{\phi}}{2}\cos\alpha. \tag{3.53}$$

This is only zero when $\dot{\phi} = 0$ or $\cos\alpha = 0$. The counterdiabatic drive can be derived from this transport operator as:

$$H_{\text{CD}} = i\dot{\hat{T}}\hat{T}^{-1} = \frac{\dot{\phi}}{2}\hat{\sigma}_z + \frac{\dot{\alpha}}{2}\hat{R}_z(\phi)\hat{\sigma}_y\hat{R}_z^\dagger(\phi). \tag{3.54}$$

This shows that if we follow an Apollonius torus in parameter space, the anti-Hermitian part is still zero when $\alpha_{\text{I}} = \text{constant}$. Even if parallel transport is not achieved, there are certain conditions where the total phase along the path cancels out. When on an Apollonius torus ($\alpha_{\text{I}} = \text{constant}$), if $\alpha_{\text{R}} = \omega$ and $\dot{\phi} = \nu$. When the path goes twice around the torus this corresponds to a full closed loop in Bloch coordinate space.

$$\int_{t_0}^{t} \langle \hat{\lambda}_{\pm}(s) | \partial_t \lambda_{\pm}(s) \rangle \, \mathrm{d}s = \pm \frac{i}{2} \int_{t_0}^{t} \nu \cos\alpha(s) \, \mathrm{d}s \tag{3.55}$$
$$= \pm \frac{i\nu}{2\omega} \Bigg[\cosh(\alpha_{\mathrm{I}}) \int_{\alpha_{\mathrm{R}}(0)}^{\alpha_{\mathrm{R}}(0)+2\pi} \cos\alpha_{\mathrm{R}} \mathrm{d}\alpha_{\mathrm{R}}$$
$$- i \sinh\alpha_{\mathrm{I}} \int_{\alpha_{\mathrm{R}}(0)}^{\alpha_{\mathrm{R}}(0)+2\pi} \sin\alpha_{\mathrm{R}} \, \mathrm{d}\alpha_{\mathrm{R}} \Bigg]$$
$$= 0$$

We can use the Berry connection to define a transport operator that parallel transports the state:

$$\hat{T}_{\parallel}(t;t_0) \equiv \hat{R}_z(\phi_t)\hat{C}_y(\alpha_t)\hat{R}_z(\beta_t)\hat{C}_y(-\alpha_{t_0})\hat{R}_z(-\phi_{t_0})\hat{R}_z(-\beta_0) \tag{3.56}$$

where

$$\beta(t) = -\int_{t_0}^{t} \dot{\phi}(s)\cos\alpha(s)\,\mathrm{d}s. \tag{3.57}$$

Using the previous method we can calculate the counterdiabatic Hamiltonian as:

$$H_{\mathrm{CD}}^{\parallel} = i\dot{T}_{\parallel}T_{\parallel}^{-1} = \frac{\dot{\phi}}{2}\hat{\sigma}_z + \frac{\dot{\alpha}}{2}\hat{R}_z(\phi)\hat{\sigma}_y\hat{R}_z^{\dagger}(\phi) - \frac{\dot{\phi}}{2}\cos\alpha\,\hat{R}_z(\phi)\hat{C}_y(\alpha)\hat{\sigma}_z\hat{C}_y^{-1}(\alpha)\hat{R}_z^{\dagger}(\phi). \tag{3.58}$$

3.3.4 Exploring the effect of non-Hermitian components in the counterdiabatic drive

The rest of this section will explore what happens if we proceed with applying a drive that requires a significant anti-Hermitian component to maintain adiabatic dynamics [80]. The parameters close to the previous path of $r = 0.973$ are $\Delta_{\circlearrowleft} = J_{\max} = 30.3$ rad/μs as shown in Fig. 3.10a (solid gray circle). If we keep $J_{\min}$ and $J_{\max}$ constant but change the max detuning to $\Delta_{\circlearrowleft} = 0.7\pi$ rad/μs, we can analyze a loop that deviates from the Apollonius circle (Fig. 3.10a pink line). Since each dashed gray line represents an Apollonius circle with a different constant α_{I}, we see that this new path crosses over many different ones.

Therefore, the anti-Hermitian part of the counterdiabatic drive becomes non-negligible as seen in Fig. 3.10b in the upper panel. Here we plot the anti-Hermitian component of H_{CD}, which is the real part of J_{CD}, and see that especially at the center of the encircling loop (around $t = 0.1$ μs) it deviates from 0 and becomes significant. In the lower panel in dark green we plot the imaginary part of J_{CD} which corresponds to the Hermitian drive. In Figure 3.10c we show the result of driving with $\tilde{H}_{\text{CD}}$. Here we see that the experimental state deviates largely from the instantaneous eigenstates. We specifically see the deviation of y from y_{I} at the center of the drive. This is around the time when the anti-Hermitian component $\text{Re}[J_{\text{CD}}]$ has significant values, but is not (and cannot) be implemented. We can quantify and verify this deviation in Fig. 3.10d with the trace distance measure (3.26). Here the gray trace corresponds to the previous encircling which closely follows an Apollonius circle and maintains a close distance D to the instantaneous eigenstates. Conversely, in the pink trace we see large spikes at the center of the drive, and a general increase in D.

3.3.5 Resolving the Riemann sheet topology

So far we have demonstrated that counterdiabatic driving is able to remain on the Riemann sheets close enough to pass through the branch cut and have eigenstate switching. Next we will explore how sharply we can transition across the exceptional points to resolve this branch cut by sweeping the value of J_{min}. This will allow us to cross through three regions: encircling zero EPs, one EP, two EPs. The relevant parameter that indicates state transfer is the Pauli expectation value $x = \langle \sigma_x \rangle$ at the end of the parameter path $x_{\text{T}} = x(t = T)$. The experimental protocol from before is implemented with initial state $|\lambda_-\rangle$. Figure 3.11b plots x_{T} for $T = 0.2$ μs and J_{min} varied from -1 to 1 rad/μs. The EP occurs at $J_{\text{EP}} = \pm 0.21$ μs^{-1}. The green trace represents driving without counterdiabtic parameters and we see no indication of the state responding the the Riemann surface. The blue trace however has a transition around $J_{\text{EP}} = \pm 0.21$ μs^{-1}. When the loop encircles zero or two EPs, we see that $x_{\text{T}} \approx -1 = \langle \lambda_- | \hat{\sigma}_x | \lambda_- \rangle$. We began in the $|\lambda_-\rangle$ state and end approximately in that state because the encircling did not pass through the branch cut. Visually, we began in the red sheet and should remain on the red sheet (Fig. 3.11a). The yellow region corresponds to encircling one EP. Previous encircling loops (Fig. 3.3(g,h)) showed us that this leads to a state transfer. This behavior is verified within the EP dashed lines where $x_{\text{T}} \approx +1 = \langle x_+ | \hat{\sigma}_x | x_+ \rangle$. We see that around the EP's the response of $x(T)$ is not very steep for $T = 0.2$ μs. With

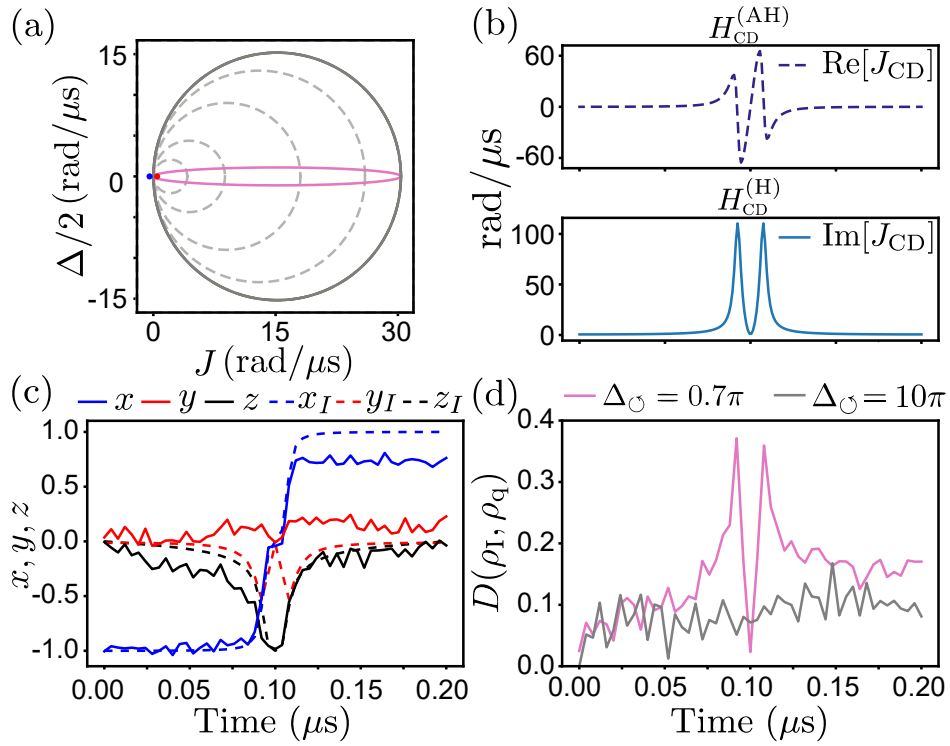

Figure 3.10: **Quantifying deviations from the Apollonius circle.** (a) The complex parameter space ε plotted with different Apollonius circle ratios r (gray circles). The solid gray circle corresponds to an Apollonius circle with $r = 0.973$. The pink line corresponds to a circle with the same J values but $\Delta_{\circlearrowleft} = 0.7\pi$. (b) The anti-Hermitian component $H_{\rm CD}^{\rm (AH)}$ is plotted as Re[$J_{\rm CD}$] in purple in the upper panel. The Hermitian component $H_{\rm CD}^{\rm (H)}$ is plotted as Im[$J_{\rm CD}$] in blue in the lower panel. (c) The encircling loop corresponding to the pink trace is experimentally performed and the tomographic results are plotted $\{x, y, z\}$. The corresponding instantaneous eigenstates are also plotted $\{x_{\rm I}, y_{\rm I}, z_{\rm I}\}$. (d) The trace distance D is calculated for the gray and pink encircling loops to quantify the effect of missing the anti-Hermitian drive components. The parameters at the time of this experiment were $\gamma_e = 1.85\ \mu{\rm s}^{-1}$ and $\gamma_f = 0.2\ \mu{\rm s}^{-1}$.

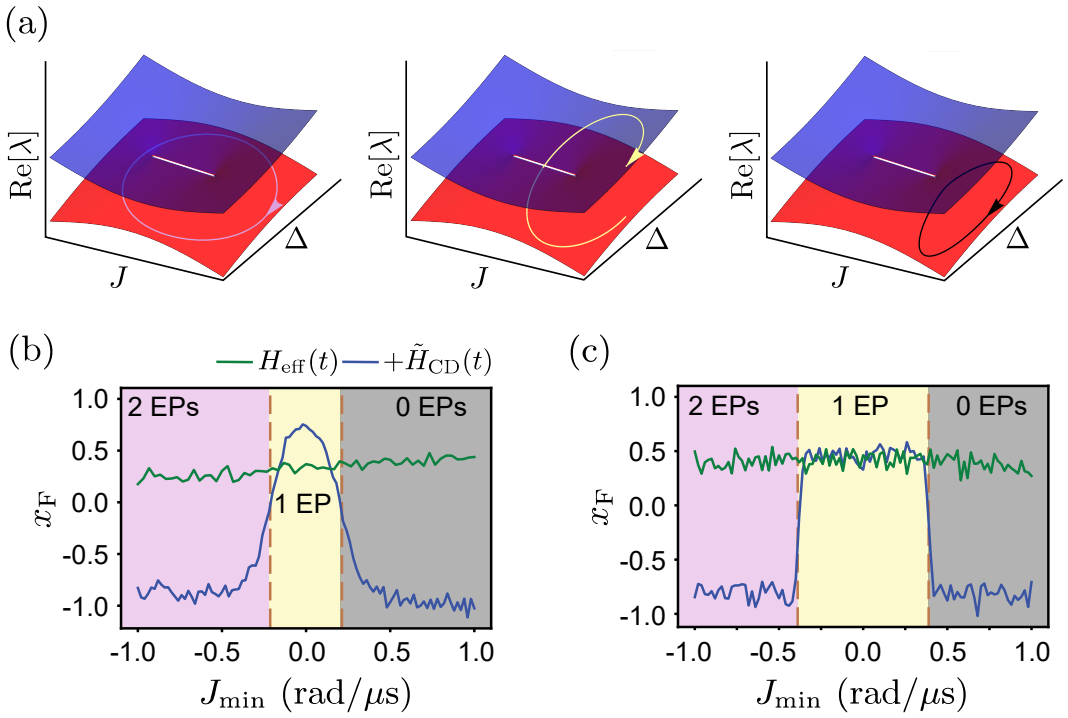

Figure 3.11: **Resolving the Riemann sheet branch cut.** (a) The three encircling regions dependent on J_{min} are plotted on the Riemann sheets. From left to right, encircling two EPs, one EP, and zero EPs. (b,c) The final point of the Pauli expectation value x_{T} plotted as a function of J_{min} from -1 to 1 rad/μs. The other encircling loop parameters are $J_{\text{max}} = 30$ rad/μs and $\Delta_{\circlearrowleft} = -10\pi$ rad/μs. The green traces correspond to driving with H_{eff} and the blue traces correspond to driving with $H_{\text{eff}} + \tilde{H}_{\text{CD}}$. Panel (b) is with $T = 0.2$ μs and $\gamma/4 = 0.21$ μs^{-1}. Panel (c) is with $T = 1$ μs and $\gamma/4 = 0.39$ μs^{-1}.

a sampling rate of 1 GS/s, the minimum time resolution for drive parameter variations is 1 ns. In Fig. 3.11c we repeat the same experiment for $T = 1$ μs. Due to the dephasing rates and decoherence effects, the contrast is lower than that of $T = 0.2$ μs. However, here we observe sharp transitions at the EPs and similar behavior in the three regions of J_{min}.

3.4 Hermitian counterdiabatic drive by way of single eigenstate tracking

Another method to obtain Hermitian driving was derived by our theory collaborators from University of Luxembourg, Niklas Hörnedal and Aurélia Chenu. The goal of staying on the

instantaneous eigenstates can be reformulated as remaining in the subspace $V(t)$ defined by our initial eigenstate $|\lambda_\pm\rangle$. A unique linear map $P(t)$ can be found that projects onto the subspace formed by an eigenstate. This map has the properties:

$$P(t)^2 = P(t), \quad P(t)^\dagger = P(t), \quad P(t)|\psi\rangle = |\psi\rangle, \quad |\psi\rangle \Leftrightarrow V(t) \tag{3.59}$$

With eigenstates $|\lambda\rangle$ the projector reads:

$$P = \frac{|\lambda\rangle\langle\lambda|}{\langle\lambda|\lambda\rangle} \tag{3.60}$$

If initialized in an eigenstate with subspace $V(0)$, the system will remain in that subspace at a later time $V(t)$ when driven with:

$$H_{\text{CD}}(t) = i[\dot{P}(t), P(t)] + 2i\langle\lambda|\dot{\lambda}\rangle P, \tag{3.61}$$

This simplifies to:

$$H_{\text{CD}}(t) = i(|\dot{\lambda}\rangle\langle\lambda| - |\lambda\rangle\langle\dot{\lambda}|). \tag{3.62}$$

Using our previous eigenvalue definitions that are dependent on Δ and J (Eq.(2.7)) we get:

$$H_{\text{CD}} = \begin{pmatrix} \Delta_{\text{CD}} & J_{\text{CD}}^* \\ J_{\text{CD}} & 0 \end{pmatrix}, \quad \Delta_{\text{CD}} = \frac{i(\dot{\lambda}\lambda^* - \lambda\dot{\lambda}^*)}{|\lambda|^2 + J^2}, \quad J_{\text{CD}} = \frac{i(\dot{J}\lambda^* - J\dot{\lambda}^*)}{|\lambda|^2 + J^2}. \tag{3.63}$$

We can now follow the protocol from Sec. 3.3 and encircle the EP in both directions starting from the $|\lambda_-\rangle$ eigenstate. The total drive parameters are extracted from $H_{\text{tot}} = H_{\text{eff}} + H_{\text{CD}}$ and are plotted in Fig. 3.12(a,b). We see in Fig. 3.12b that the component corresponding to the frequency detuning of the drive has a large spike in the center of the drive. Though this peak occurs at ≈ 2000 rad/μs $= 318.3$ MHz, we don't see obvious effects in the dynamics of the system. The anharmonicity of this qubit is $\eta \approx 150$ MHz. Thus, it is important to verify with the addition of counterdiabatic controls that other energy transitions are not being driven. Since this peak is narrow and away from the anharmonicity, we don't see a detrimental effect. The Pauli matrix expectation values are plotted in Fig. 3.12(c,d).

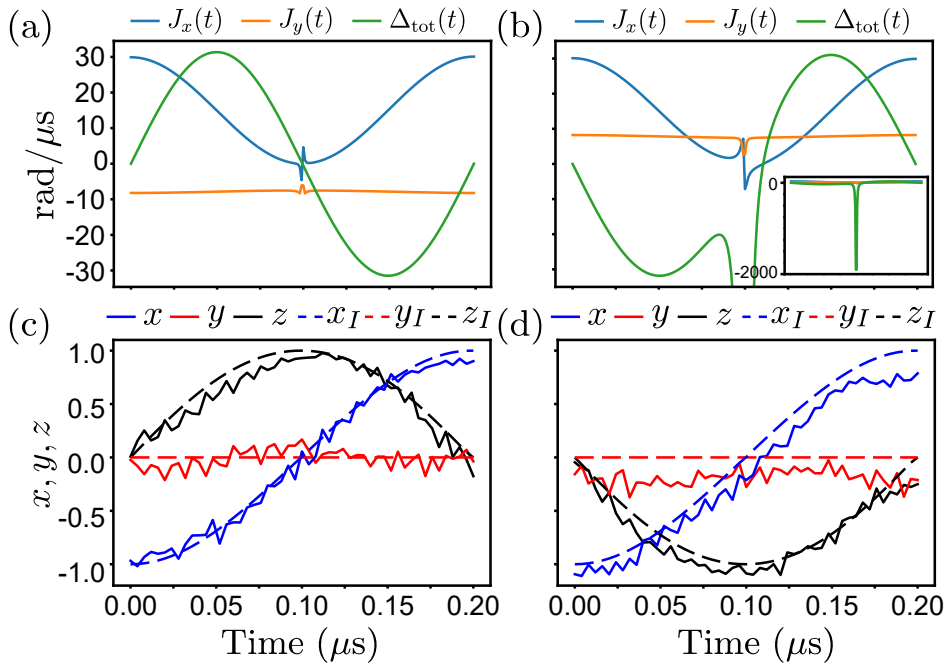

Figure 3.12: **Hermitian counterdiabatic drive from single eigenstate tracking.** (a) The total drive parameters from $H_{\rm tot} = H_{\rm eff} + H_{\rm CD}$ are plotted as a function of time for $T = 0.2$ μs. The drive is according to Eq. (2.26) with $J_{\rm max}$, $J_{\rm min}$, and $|\Delta_{\circlearrowleft,\circlearrowright}|$ are all the same as Fig. 3.3(a,b). Here we plot the total drive parameters as: $J_x(t) = J(t) + {\rm Re}[J_{\rm CD}(t)]$, $J_y(t) = {\rm Im}[J_{\rm CD}(t)]$, and $\Delta_{\rm tot}(t) = \Delta(t) + \Delta_{\rm CD}(t)$. (c,d) Plot the Pauli expectation values (solid lines) as a function of time for each encircling direction. The dashed lines represent the Pauli expectation values of the instantaneous eigenstates.

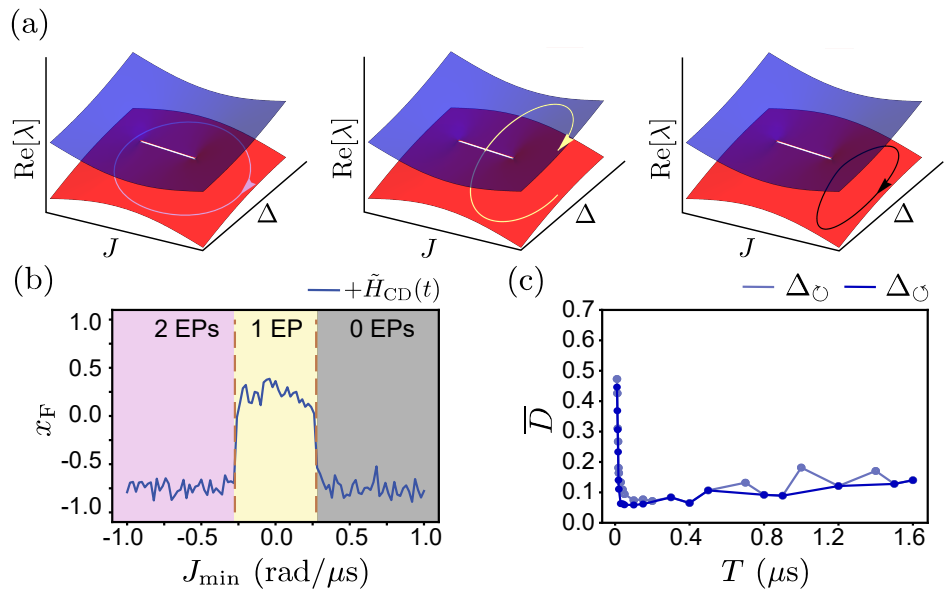

Figure 3.13: **Single eigenstate tracking method experimental results.** (a) The encircling paths for the three different loop types. Pink is encircling two EPs, yellow is encircling one EP, and black is encircling no EPs. (b) The final point of the x-tomography is plotted as a function of J_{min}. We see a sharp transition at the exceptional points from no state transfer (pink and black) to state transfer in the yellow region. (c) The average trace distance $\overline{D}$ is plotted for various loop times T. We see the same increase at short times due to the same experimental limit.

We can explore the sensitivity to the EPs using the same sweep from before of J_{min} from Fig. 3.11. In this sweep the loop time was $T = 1.5$ μs. We prepare the system in $|\lambda_-\rangle$ where $x(0) = -1$, and observe that the state returns to ≈ -1 in the pink and black regions where we do not pass through a branch cut. In the yellow region we observe the increase of $x > 0$. Due to the longer loop period, there is significant dephasing and decoherence taken place, however the sharp behavior is still observed.

The efficacy of this method can be determined using the trace distance metric from earlier Eq. (3.26). $\overline{D}$ is plotted as a function of loop time T in Fig. 3.13 where we observe similar behavior to the counterdiabatic driving method from Sec. 3.3. The average remains much lower than driving with H_{eff} in shorter time scales.

3.5 Conclusion

By identifying specific parameter paths called Apollonius circles that eliminate the non-Hermitian components of the drive, we are able to extend the methods of counterdiabatic driving to non-Hermitian systems. Allowing us to preserve and utilize the rich topology of the energy landscape. Since the significant feature of the energy spectrum that allows this eigenstate switch behavior is the branch cut, passing through it from one sheet to the other is the priority. The actual path taken won't determine the eigenstate switch topologically. Path independent quantities such as the geometric phase (Berry phase) are preserved in closed loops only. Therefore, these Apollonius circles provide flexibility in parameter space and extend the applicability of these drives to non-Hermitian systems. The Berry phase was first experimentally measured in a classical optical fiber [99]. In quantum systems the Berry phase has been explored theoretically and measured [100, 101, 16, 102, 103, 104, 105, 106]. The method of shortcuts to adiabaticity was used to measure the Berry phase in a superconducting phase qubit [107]. Geometric phases have potential uses in quantum computation [108, 109]. In addition, it was recently demonstrated in an optomechanical system that the Berry phase for a non-Hermitian system, which is complex, can provide steady state amplification [110].

For systems where the non-Hermitian contributions cannot be minimized using Apollonius paths, the second method introduced in Section 3.4 reduces the space to the single eigenstate subspace and provides a Hermitian drive. For both of the drives, one must pay attention to the limitations introduced by experimental apparatus. We showed that with small loop times ($T < 0.02\ \mu$s), the drive strength required by the counterdiabatic Hamiltonian exceeds the apparatus limit. For the method described in Sec. 3.4, the counterdiabatic addition to the detuning approaches and exceeds the anharmonicity. Though no effect is observed by this, it is a limitation to look out for if the time spent driving in other frequency transitions is significant.

Complex eigenvalues give us an elegant way to dynamically and smoothly tune our parameters such that we switch between states of our system. Previously thought of as discrete states that we can "jump" between now become continuous in their real and imaginary components. Complex energies not only provide physically observable dynamics in the quantum state, but also a rich topology that we are able to preserve with STA. The efficacy of these

counterdiabatic drives on a non-Hermitian system have been shown for a second order exceptional point (EP2). One can extend the concept of encircling to higher order exceptional points [53, 111, 112]. These higher order EPs have benefits such as an increase in sensitivity [75] or speed up of entanglement [24]. This can be extended to our setup by including more energy levels and due to the anharmonicity, we can continue to apply separate drives to each energy transition. We can write out a Hamiltonian that is $n \times n$ (previously it was 2×2). For example, by including the $|h\rangle$ state, the drive frequencies and strengths of each energy transition denoted by Δ_{ij}, J_{ij}, we can write [53]:

$$H_{\text{eff}} = \begin{pmatrix} -i\gamma/2 + \Delta_{ef} & J_{ge}^* & 0 \\ J_{ge} & \Delta_{fh} & J_{fh}^* \\ 0 & J_{fh} & 0 \end{pmatrix} \tag{3.64}$$

This matrix has the property of third-order exceptional points (EP3) and second-order exceptional lines (EP2). For methods on how to derive these higher-order exceptional points and lines, refer to [111, 53]. When we are able to identify these EPs, we can explore different encircling paths. This gives rise to non-trivial braiding among eigenstates that correspond to braid groups. Now that we have demonstrated experimentally feasible ways to control the non-Hermitian system according to its Riemann topology, future research in this field would be to extend the counterdiabatic drives to encircling the higher-order exceptional points.

Chapter 4

Thermodynamics in quantum systems

We have so far been exploring the limits of controlling a non-Hermitian system due to loss and observing the features of the Riemann topology due to the complex spectrum. This next chapter will explore the role of the non-Hermitian Hamiltonian and its complex energy spectrum as they pertain to heat and work in thermodynamics. In Section 4.1, we define the first and second laws of thermodynamics which are well understood in large systems. The second law of thermodynamics in particular has different forms depending on the process being analyzed. In Section 4.2, we show how, when the system size is reduced and systems are driven in a non-equilibrium manner, the laws of thermodynamics can be applied using fluctuation theorems. We also develop a protocol to measure the work probability distribution to calculate a specific fluctuation theorem: the Jarzynski equality [44]. In Section 4.3, we apply this protocol to the qubit with various closed-loop parameter variations that explore the complex eigenvalue space. In Section 4.4, we extend this protocol to non-cyclic paths in simulation. The results described in the last two sections were published in [80].

4.1 The first and second laws of thermodynamics

As we saw in Chapter 2, non-Hermitian systems can arise from open quantum systems. Thus, a natural connection to a system coupled to an environment is thermodynamics which studies and constrains the processes that can occur between the two. Through thermodynamics, we have measurable and well-defined variables available to us: internal energy U, work applied to the system W, heat transferred to the system Q, entropy of the system S, and temperature of the system (reservoir) T. The values of these energy exchanges and extrinsic and intrinsic properties are governed by the first and second laws of thermodynamics. The first law requires conservation of energy, while the second law limits how we use energy [113].

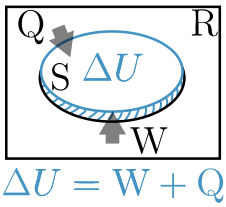

Figure 4.1: **First Law of thermodynamics.** The internal energy of a system, U, is changed by work W applied to the system and heat Q transferred between the system and reservoir.

The first law of thermodynamics can be written as:

$$\Delta U = W + Q. \tag{4.1}$$

Where ΔU is the change in internal energy of the system and is a state function, therefore path independent. The sign of these measurements indicate whether it is going into $(+)$ or out of $(-)$ the system. Figure 4.1 schematically shows how interactions between system and reservoir can change the internal energy of the system. This law constrains the possible changes on a system's internal energy, whether deliberate or not and tells us that energy cannot be created nor destroyed.

The second law of thermodynamics has different forms of expression depending on the concept and process to be analyzed. Ultimately, it constrains energy conversion and limits the directionality of events. A useful equation of entropy, the Clausius relation, relates infinitesimal changes in heat: $dS = \delta Q/T$. Integrating this expression gives us the entropy change between two equilibrium states $\Delta S = \int_i^f dQ/T$. The Clausius relation is for a reversible process, but since ΔS is a change in state property, it can also give ΔS for an irreversible process. Motivated by engineering challenges in engine design, early formulators of thermodynamics had discovered the limits of certain processes. There are two equivalent statements of the second law. First, the Clausius statement which often applies to refrigeration heat flow and was stated as: "It is impossible to construct a device which operates on a cycle and whose sole effect is the transfer of heat from a cooler body to a hotter body." Secondly, the Kelvin-Planck statement says: "No process is possible whose sole result is the absorption of heat from a reservoir and the conversion of this heat into work." [113]. It is essentially stating that no process can perfectly produce work obtained from heat from a cooling reservoir. The theoretical maximum of this efficiency is $\eta = 1 - \frac{Q_C}{Q_H} = 1 - \frac{T_C}{T_H}$. This efficiency was derived from a Carnot engine in which an engine operates between two reservoirs, one hot and one

cold. For the Carnot engine to be 100% efficient, $T_C = 0$. However, we cannot achieve this temperature in nature, therefore a heat engine with 100% efficiency is not possible [113].

The formulation of the second law most useful to this research is:

$$\Delta F \leq \overline{W} \tag{4.2}$$

This inequality holds for non-equilibrium processes and states that the amount of work done, on average, must be greater than the free energy difference $\Delta F \equiv F_f - F_i$. Here, the free energy is defined as the Helmholtz free energy. This energy is the type of useful work obtainable from a closed thermodynamic system at constant temperature (isothermal). The equality holds when the parameters of the system are changed quasi-statically such that the total work performed on the system is equal to the Helmholtz free energy and the process is reversible. If the parameters are changed at a finite rate, then the work is on average greater than ΔF since the system doesn't have time to equilibrate after each change. Therefore, $W_{\text{diss}} = \overline{W} - \Delta F$ represents the dissipated irreversible work.

These laws have been extensively studied for large systems ($N \to \infty$). Since any particle interactions and behaviors are averaged out over the whole system, measurements like pressure, temperature, and volume are well defined. Consider the classic example of an ideal gas in a box (Fig. 4.2a). The combination of microstates, Ω (possible particle arrangements), that give us the most probable macrostate (macroscopic description) tends towards the particles being evenly spread out across the box. This is the configuration with the highest entropy where: $S = k_B \ln \Omega$ and k_B is the Boltzmann constant. In other words, if we were to imagine splitting the box in half, an overwhelming number of microstates would have $(N/2)$ on each side.

Now imagine adding a movable wall as pictured in Figure 4.2b. As the wall is slowly pulled outwards, the volume is increased and the gas particles spread apart, decreasing the pressure. There is work applied to the slowly moving wall by the air particles to always stay near equilibrium and heat added to maintain the internal energy $\Delta U = 0 = -W + Q$. The work can be written as: $W = \int P dV$ $(dW = PdV)$ [114]. Using the ideal gas law, $PV = Nk_BT$ and the fact that $dW = dQ$, we can then plug this into the earlier equation and obtain: $\Delta S = \int_i^f dQ/T = Nk_B \ln 2$. The entropy increases because the particles are overwhelmingly

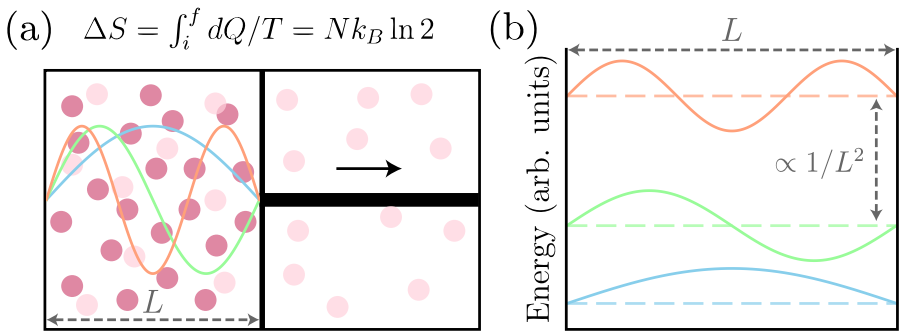

Figure 4.2: **Particles in a box.** (a) $N \to \infty$ number of particles in a box will be most likely distributed evenly due to the entropy being maximized (light pink particles). The number of microstates Ω that represent the macrostate of $N/2$ particles on each side is largest. Splitting the box in half (solid black wall) and measuring the number of particles will most likely yield $N/2$ on each side. Next, all the gas is on one side (dark pink particles) and settled at equilibrium with a movable wall (solid black wall). If the wall is slowly moved to the right to a new volume $V_f = 2V_i$, the gas will expand to fill the new size. The work and heat are well defined and measurable parameters of the system. The entropy change ΔS can be calculated assuming the quasi-static expansion and the ideal gas law $PV = Nk_BT$. If the particle number is lowered to a few particles, the fluctuations in measured pressure against the wall will yield different entropy values in each repetition. We can further decrease our system to a single particle in a box of length L. (b) The wall of the box can still be moved but now instead of measuring volume V, we are affecting the energy spacing of the wave functions. The spacing between energy levels is $\propto 1/L^2$.

more likely to be found distributed throughout the larger volume than concentrated in the smaller region, making spontaneous return to the initial state virtually impossible.

4.2 Fluctuation theorems

The irreversibility described by the second law of thermodynamics seemed to contradict the reversible dynamics allowed by equations of motion in microscopic systems. As the particle number is decreased and we consider a smaller system, the individual statistical fluctuations begin to affect measurements [115]. If we measure the number of particles on each side of the box multiple times, we will not always measure $N/2$ on each. Similarly, if you have a single to a few particles bouncing off of the wall, it will measure different pressures and volumes at different times. If the moving wall example is repeated multiple times the work and heat transferred to keep constant temperature will be different each time due to the microscopic

dynamics of the particles, such that we can see probabilistic violations of the second law due to fluctuations. Another aspect that is commonly encountered are systems out of equilibrium. If the wall is abruptly pulled outwards and pushed inwards to return to the initial position, the system is out of equilibrium and the work done on the system is $W > 0$. For small systems and many repeated measurements, we find on average $\langle W \rangle > 0$. This implies that on occasion, we may measure negative work [116]. The following sections will aim to show that the second law is a probabilistic law that emerges from statistical mechanics—one that is observed and verified in nature due to the enormous number of particles and accessible microstates in macroscopic systems. In 1993, Evans and Searles [115] addressed this concern of violations of the second law in systems that begin in equilibrium but end in a steady state far from equilibrium using numerical simulations. They concluded that temporary violations occurred at the microscopic level, but the probability of such violations decreased over time [117, 118]. That is, for a trajectory that has a positive entropy production, the time-reversed trajectory that has a negative entropy production (and violates the second law) becomes exponentially less likely as time $t \to \infty$. In 1995, Gallavotti and Cohen derived a fluctuation theorem in terms of asymmetry between entropy production in the forward and reverse paths for thermostatted steady-state systems out of equilibrium and with assumptions of chaoticity [119]. Where A is an entropy production rate and t is time, these earlier fluctuation theorems had a form similar to:

$$\frac{P(A)}{P(-A)} = e^{-At}. \tag{4.3}$$

This ratio shows that positive entropy production is exponentially more likely than negative in the limit of $t \to \infty$. It also shows that while there may be individual violations, the probability distribution follows a certain symmetry. This theorem was then further explored in stochastic dynamics [120, 121, 122]. These theorems, valid for systems driven arbitrarily away from equilibrium, showed that for longer timescales or averages, the expected second law behavior is recovered [123].

In a similar vein to the earlier fluctuation theorems, the Crooks fluctuation theorem relates the probability distributions of the entropy production for the forward process P_{F} and reversed P_{R} in a driven system [124]

$$\frac{P_{\mathrm{F}}(+S)}{P_{\mathrm{R}}(-S)} = e^{S}. \tag{4.4}$$

These relations both describe driven systems whereas the Gallavotti-Cohen theorem is about steady-state driven systems and the Crooks theorem is for time-dependent processes and microscopically reversible dynamics. The previous example from Fig. 4.2b is useful to understand this relation. The gas in the box starts at a certain volume at equilibrium. As the wall is pushed in at a certain rate, the gas compresses and stops at a new volume. Now if the wall is pulled outwards at the same rate, we obtain the reverse (R) process. If these processes are repeated multiple times, the probability distributions ($P_{\mathrm{F,R}}$) satisfy this relation. A great result of this relation is that it is valid for any rate and particle limit. We can connect this to the earlier form of the second law (Eq (4.2)) and Kelvin-Planck statement using [116]:

$$-\langle W\rangle_R \leq \Delta F \leq \langle W\rangle_F, \tag{4.5}$$

$$\langle W\rangle_R + \langle W\rangle_F \geq 0 \tag{4.6}$$

Fluctuation theorems were subsequently verified experimentally in classical microscopic systems on platforms such as molecules, turbulent flow, and a classical two-state single-electron box [125, 126, 127, 128, 129, 130, 131, 132, 133].

4.2.1 The Jarzynski equality

These fluctuation theorems have been useful to understand systems driven far from equilibrium and their entropy production. When we consider experiments on qubits where we apply sequences of pulses and Hamiltonian variations, the speeds and strength at which they occur can bring our system out of equilibrium. Thus it is important to consider how to further extend fluctuation theorems to the measurements we make on quantum systems with fast, non-equilibrium dynamics. In 1997, Jarzynski derived a relation for measurements of the work on a system in a non-equilibrium process to its equilibrium free energy change [44, 116, 134]

$$\langle e^{-\beta W} \rangle = \frac{Z(T)}{Z(0)} \equiv e^{-\beta \Delta F} \tag{4.7}$$

where $Z(t)$ is called the partition function and is defined as $Z(t) \equiv \mathrm{Tr}[e^{-\beta H(t)}]$ and $\beta \equiv \frac{1}{k_B T}$ is the inverse temperature. The brackets denote an ensemble average taken over many repeated measurements. Eq. (4.7) holds for arbitrary non-equilibrium paths taken between two equilibrium, measurable states of the system. The result of this equality is that many measurements on a system that is in non-equilibrium give us information on its equilibrium state due to the underlying information in the fluctuations of work. Eq. (4.7) is an extended case of Eq. (4.2) which can be recovered using Jensen's inequality. Jensen's inequality states that for any convex function: $\langle g(x) \rangle \geq g(\langle x \rangle)$. We can check that our function is convex and apply the rule:

$$\frac{\partial^2}{\partial W^2} e^{-\beta W} = \beta^2 e^{-\beta W} > 0, \tag{4.8}$$

Since $e^{-\beta W}$ is convex, Jensen's inequality gives us:

$$\langle e^{-\beta W} \rangle \geq e^{\langle -\beta W \rangle}, \tag{4.9}$$

Taking the natural logarithm of the Jarzynski equality:

$$\ln \langle e^{-\beta W} \rangle = -\beta \Delta F, \tag{4.10}$$

Combining equations (4.9) and (4.10):

$$-\beta \Delta F \geq \langle -\beta W \rangle, \tag{4.11}$$

$$\therefore \quad \Delta F \leq \langle W \rangle. \tag{4.12}$$

Since the Jarzynski equality (4.7) and the previous notations (Eqs (4.2),(4.6)) refer to the average of the work measurements but the Crooks relation concerns the probability distribution of these fluctuations, it can thus be useful to see the relationship as follows. The Crooks

relation (4.4) can be modified to look like the Jarznyski equality [124] with the following steps.

$$\langle e^{-S} \rangle = \int_{-\infty}^{-\infty} P_{\mathrm{F}}(+S) e^{-S} dS = \int_{-\infty}^{-\infty} P_{\mathrm{R}}(-S) dS = 1, \tag{4.13}$$

where we average over the probability distributions. For systems that start in equilibrium $S = -\beta\Delta F + \beta W$:

$$\langle e^{-(-\beta\Delta F + \beta W)} \rangle = 1, \tag{4.14}$$

Since ΔF is a state function, we can pull it out of the average:

$$e^{\beta\Delta F} \langle e^{-\beta W} \rangle = 1 \tag{4.15}$$

$$\therefore \quad \langle e^{-\beta W} \rangle = e^{-\beta\Delta F}. \tag{4.16}$$

The Jarzynski equality has been verified first in classical systems [135, 125, 136, 137, 138, 130], then extended to quantum systems [139, 140, 141, 142, 143, 144, 145]. For systems described by a similar Hamiltonian as our qubit, there have been predicted violations when the spectrum of the non-Hermitian Hamiltonian, H_{eff}, turns complex [146, 147, 148, 149, 150, 151]. The following sections will show how we apply certain measurement protocols to best understand how measurements of a dissipative non-Hermitian system are related to its dynamics.

4.2.2 Energy distribution and measurements

In Figure 4.2, we further reduce the system size to a single particle. We can plot the wavefunctions of a single particle in a box of length L, particle mass m, mode number n (up to $n = 3$), and Planck's constant h. The energy spacing between these wave functions (Fig. 4.2b), are inverse quadratically dependent on the length of the box $E_n = \frac{n^2 h^2}{8mL^2}$. Therefore, moving the wall inwards and outwards changes the energy levels. The internal energy change of this system after performing the work to change the size of the box is related to

$\Delta U = E_n(L_2) - E_n(L_1)$. In quantum systems, the relevant descriptors are the Hamiltonian and the density matrix (qubit state). In a closed quantum system the Hermitian Hamiltonian, $H(t)$ with eigenvalues $H|\lambda\rangle = \lambda|\lambda\rangle$, has the role of the internal energy operator $U(t) \equiv \mathrm{Tr}[\rho(t)H(t)]$ and generator of its time dynamics, $\hat{G}(t) = e^{-iHt}$. Our qubit energy levels are distributed similarly to the particle in a box. However, instead of changing the length of the box to apply work, we can change the values in our Hamiltonian $H(t)$, such as drive strength J and detuning Δ, to change the spacing between our eigenvalues.

To quantify the internal energy change in a quantum system, ΔU, it is common to employ the "two-point projective measurement" (TPM) protocol [152, 153, 154]. Projectively measuring a qubit obtains one of it's eigenstates and leaves the qubit in the associated eigenstate. Therefore, performing a measurement in the beginning and end of an experiment will give you the initial and final energy states in terms of transition probabilities P_{ij}. Where j is the initial state and i is the final state, P_{ij} refers to the probability of measuring in state i given the system started in state $j : P(i|j)$. This gives us an internal energy distribution $P(\Delta U)$:

$$P(\Delta U) = \sum_{i,j=\pm x} P_{ij} P_j \delta(\Delta U - (\Delta\lambda)) \tag{4.17}$$

Therefore, the probability of measuring $\lambda_j(0)$ and $\lambda_i(T)$ is $P(j \cap i) = P(i|j)P_j$. The initial probability of measuring the eigenvalue in a Gibbs state [154]:

$$\frac{e^{-\beta H(0)}}{Z(0)} \rightarrow P_j = \frac{e^{-\beta\lambda_j(0)}}{Z(0)}. \tag{4.18}$$

When this protocol is applied to a closed quantum system, $Q = 0$, this becomes the probability distribution of the work, $P(W)$.

In a Hermitian system, we experimentally measure with our right eigenvector projectors (Sec. 2.1.2):

$$\Pi_n = |n\rangle\langle n| \tag{4.19}$$

Where $|n\rangle$ is our measurement energy basis. Focusing on measuring the eigenstates of the Hamiltonian, we can look at that cases where $|n\rangle \in |\pm x\rangle$. The system is prepared in some pure state $|\psi(0)\rangle = |j\rangle$, where $j \in |\pm x\rangle$ and evolved for a time t. The evolved state is now in some combination of $|\psi(t)\rangle = \alpha|+x\rangle + \beta|-x\rangle$. Now if we want to find the transition probability from initial state j to some final state $i \in |\pm x\rangle$, we can make separate measurements in the respective basis.

$$p_{+xj} = |\alpha|^2 = \langle\psi(t)|\Pi_+|\psi(t)\rangle \tag{4.20}$$

$$p_{-xj} = |\beta|^2 = \langle\psi(t)|\Pi_-|\psi(t)\rangle \tag{4.21}$$

Since a single measurement will project the state $\psi(t)$ into one of the measurement states $|\pm x\rangle$, we obtain a 0 or a 1. Therefore, we repeat this measurement N times and calculate the ratio:

$$P_{\pm xj} = \frac{\sum_N p_{\pm xj}}{N} \tag{4.22}$$

An important property to note is that $P_{+xj} + P_{-xj} = 1$.

In non-Hermitian systems, we encounter imaginary terms. While these terms have a significant and observable affect on time evolution, we can only measure real values in experiment. Therefore, the following experiments are performed with the projective measurements in the TPM protocol in the Hermitian (real eigenvalue) basis [155].

To connect the TPM protocol from subsection 4.2.2 to our non-Hermitian qubit, we have a sequence of pulses and drives (Fig. 4.5a). The projective measurements will be made such that we obtain ΔU in the $|e\rangle - |f\rangle$ manifold. Our sequence begins with preparing our qubit in one of the eigenstates of its initial Hamiltonian $H(0) = J\sigma_x$, $|\pm x\rangle = (|f\rangle + |e\rangle)/2$ by applying a π rotation to bring it to the $|e\rangle$ state and a $\pi/2$ rotation to the $|\pm x\rangle$ state. We synthesize an initial Gibbs state with $P_\pm = e^{\mp\beta J_{\max}}$. $\beta = 0.5\mu s^{-1}$ for all of these experiments. We then evolve $H_{\text{eff}}(t)$ according to $J(t)$ and $\Delta(t)$ (Eqs. (4.25), (4.26) and (4.27)). We then perform state tomography rotations for a final projective measurement in our energy basis

$|g\rangle, |+x\rangle, |-x\rangle$.

$$p_m = \mathrm{Tr}[\Pi_m \rho] = \langle m|\rho|m\rangle \tag{4.23}$$

where $m \in |g\rangle, |+x\rangle, |-x\rangle$. To extend the probability distribution to our non-Hermitian system, we define the following relationship to transition probabilities due to post-selection:

$$P_{ij}(T) = \frac{|\langle i|G(T)|j\rangle|^2}{\langle j|G^\dagger(T)G(T)|j\rangle} = \frac{p_{ij}}{p_{+x,j} + p_{-x,j}} \tag{4.24}$$

On the right hand side, we have p_{ij} which is one of the following: $p_{g,j}, p_{+x,j}, p_{-x,j}$. We obtain these by applying a pulse that rotates $|+x\rangle$ to the $|f\rangle$ state and $|-x\rangle$ to the $|e\rangle$ state. Therefore, when we perform 3-state readout, we can threshold our data to obtain p_g, p_{+x}, p_{-x} (given it started in j). Because post selection is norm preserving, we have the property $\sum_i P_{ij}(T) = 1$ (Fig. 4.5b). The four possible eigenstate transitions we can measure are depicted in Figure 4.5a's upper panel. The non-unitary evolution operator is defined as $G(T) = \mathbb{T}\exp\left[-i\int_0^T H_{\text{eff}}(t')dt'\right]$. Since we are driving a closed loop, we can also define a Floquet Hamiltonian defined as $G(T) \equiv \exp(-iTH^F_{\text{eff}})$, where $H^F_{\text{eff}} \equiv H^F + i\Gamma^F$ and H^F is the Floquet internal energy operator.

4.3 Results

As discussed in Chapter 2, the non-Hermitian Hamiltonian obeys different properties based on its parameters: non-Hermiticity, $\mathcal{PT}$-symmetry, and broken $\mathcal{PT}$-symmetry. In this next section, we will start to explore the consequences of these different regions [155]. For simplicity, the experimental paths we take will be a closed loop. Since our initial and final Hamiltonians will be the same, $H_{\text{eff}}(0) = H_{\text{eff}}(T)$, it follows that, $\frac{Z(T)}{Z(0)} = 1$. This is analogous to the box example of changing the size of the box but returning it to the initial size. We will prepare our system in some initial quantum state ρ_{eq}, evolve it according to the system Hamiltonian, H_{eff}, and then perform a projective energy measurement for its final state (Fig. 4.3). The Hamiltonian will be varied according to the following parameter paths visualized in Figure 4.4:

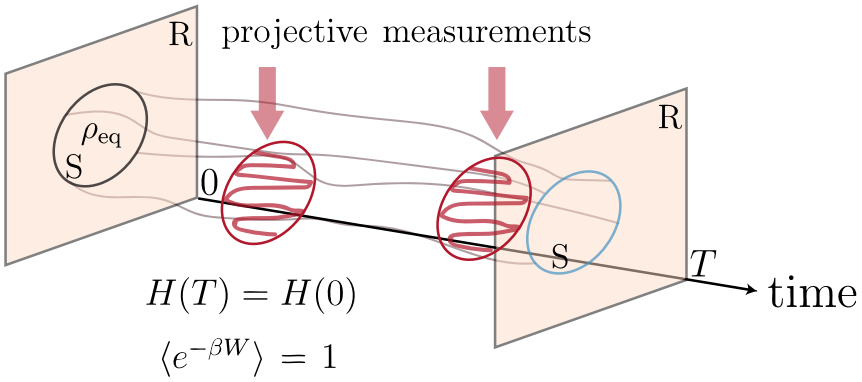

Figure 4.3: **General protocol for the experiment.** We prepare the quantum system (S) in an initial equilibrium state ρ_{eq}. This quantum system is a subset of a larger environment to which it is coupled to as a reservoir (R). We perform two projective measurements at time $= 0$ and at time $= T$ in the energy basis of H. The system is evolved over time according to $H_{\text{eff}}(t)$ with $H(0) = H(T)$. The various states of the initial system experience the Hamiltonian variation in different ways which we will observe through the projective energy measurements and using the Jarzynski equality (4.7) as a metric.

$$J(t) = \bar{J} + \frac{(J_{\max} - J_{\min})}{2} \cos\left(\frac{2\pi t}{T}\right), \ \Delta(t) = 0 \tag{4.25}$$

$$\Delta_1(t) = \Delta_{\max} \sin\left(\frac{\pi t}{T}\right), \ J(t) = J_{\max} \tag{4.26}$$

$$\Delta_2(t) = \Delta_{\max} \sin\left(\frac{2\pi t}{T}\right), \ J(t) = J_{\max}, \tag{4.27}$$

where T is the duration of the loop and $\bar{J} = (J_{\max} + J_{\min})/2$. By utilizing the minima and maxima of these equations, we can explore different parameter regimes of our Hamiltonian, H_{eff}.

We repeat this measurement sequence with a range of loop times 0.1 μs $\leq$ T $\leq$ 1 μs. In Fig 4.6a, we start out with the simplest case of constant $J(t)$ and $\Delta(t)$. We have $J_{\max} = J_{\min} = 3.74$ rad/μs and $\Delta_{\max} = 0$ in the $\mathcal{PT}$-symmetric regime. Here, we see that the transition probabilities are symmetric. What this means is that the probability of staying or transitioning to the other state is the same for both eigenstates. In Fig. 4.6b, we run the same loops but with $\Delta_{\max} = 10\pi$ rad/μs. Having a non-zero $\Delta_{\max}$ breaks our explicit $\mathcal{PT}$ symmetry. However, in this plot, we now see that the symmetry of surviving in/transitioning out of a state is broken between initial eigenstates ($P_{++} \neq P_{--}/P_{-+} \neq P_{+-}$). The reasoning

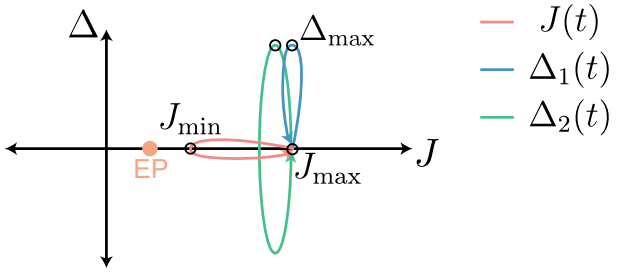

Figure 4.4: **Parameter paths.** We will explore three different path types $J(t)$ (4.25) (orange), $\Delta_1(t)$ (4.26) (blue), and $\Delta_2(t)$ (4.27) (green). $J(t)$ begins at some $J_{\max}$ and is varied to a $J_{\min}$ and back to the maximum. $\Delta_1(t)$ has a constant $J(t) = J_{\max}$ and begins at $\Delta = 0$ and is varied up to a $\Delta_{\max}$ and back down to 0. The third path, $\Delta_2(t)$, is a symmetric loop about the x-axis. It also has a constant $J(t) = J_{\max}$ and begins at 0, but is varied up to a maximum $\Delta_{\max}$, down to $-\Delta_{\max}$, and then ends at 0.

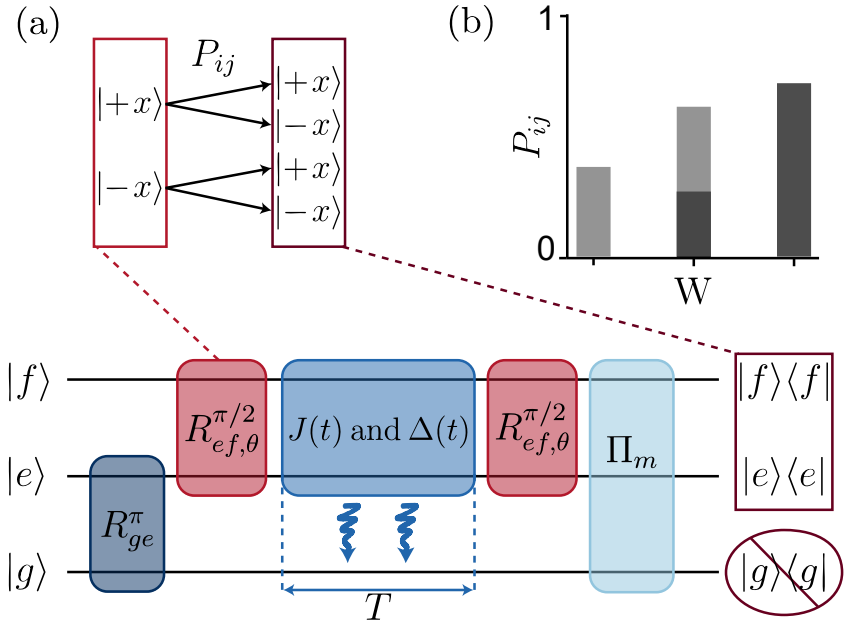

Figure 4.5: **Obtaining the work probability distribution.** (a) The experimental sequence to realize TPM, post-selection and the variation of parameters. First we prepare an eigenstate of $H(t)$, $|\pm x\rangle = (|f\rangle \pm |e\rangle)/\sqrt{2}$, by applying resonant rotation pulses R^{π}_{ge} and $R^{\pi/2}_{ef,\theta}$ (where $\theta = \pi$ for $|+x\rangle$ or 0 for $|-x\rangle$). We then tune the parameters of $H(t)$ for a certain time T and returning it to its initial value $H(T) = H(0)$. Finally, we apply a final $R^{\pi/2}_{ef,\theta}$ rotation and post-selective quantum state tomography. (b) By repeating each preparation sequence 3000 times and post-selecting, we sample both initial states $|j\rangle \in \{|+x\rangle, |-x\rangle\}$ and obtain the transition probabilities P_{ij} within the excited-state manifold $\{|e\rangle, |f\rangle\}$.

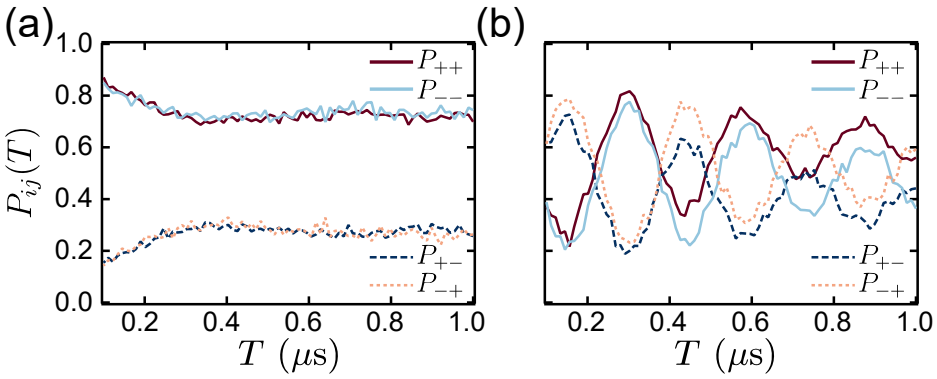

Figure 4.6: **Transition probabilities.** Transition probabilities $P_{ij}(T)$ for loop times ranging between 0.1 μs $\leq T \leq$ 1 μs. (a) Eq. (4.25) with $J_{\max} = J_{\min} = 3.74$ rad/μs and Eq. (4.26) $\Delta_{\max} = 0$. (b) with the same Eq. (4.25) but Eq. (4.26) $\Delta_{\max} = 10\pi$ rad/μs.

for this will be discussed later in Section 4.5. How will these symmetries and asymmetries affect the internal energy distribution used in the Jarzynski equality (4.7)?

We can expand the left-hand side of Eq. (4.7) into the probability distribution that represents its ensemble average:

$$\langle e^{-\beta \Delta U} \rangle(T) = \sum_{ij=\pm x} e^{-\beta(J_{\max,i} - J_{\max,j})} P_{ij}(T) P_j, \tag{4.28}$$

where P_{ij} are the experimentally obtained transition probabilities. Since we are driving our system with closed loops where $\Delta(0) = \Delta(t) = 0$, our initial and final eigenstate energies depend only on $J_{\max}$. In the previous section we measured transition probabilities that give us our internal energy distribution. With a synthesized Gibbs state with inverse temperature $\beta = 0.5$ μs/rad, we have initial probabilities of $P_{\pm x} = \{0.98, 0.02\}$. With all the pieces of the equation, we can now plug them into Eq. (4.28).

All of the figures in Fig. 4.7 include an inset of the path taken with $J(t)$ and $\Delta(t)$. The positive EP is plotted at $J_{\text{EP}} = +\gamma/4$. Though these parameter drives can be done similarly when reflected about the y-axis (with $J_{\text{EP}} = -\gamma/4$). Figure 4.7a displays Eq. (4.28) for the transition probabilities obtained in Fig. 4.6a in the red trace. The black trace corresponds to $J_{\max} = J_{\min} = 1.89$ rad/μs. Here we see that the LHS (4.28) is equal to 1 as we expected from the RHS ($\frac{Z(T)}{Z(0)} = 1$). Thus, our TPM measurements calculated $\Delta U = W$. In Fig. 4.7b we have $J_{\min} = 0.5 J_{\max}$ so the path is varied but confined to the $\mathcal{PT}$ symmetric region

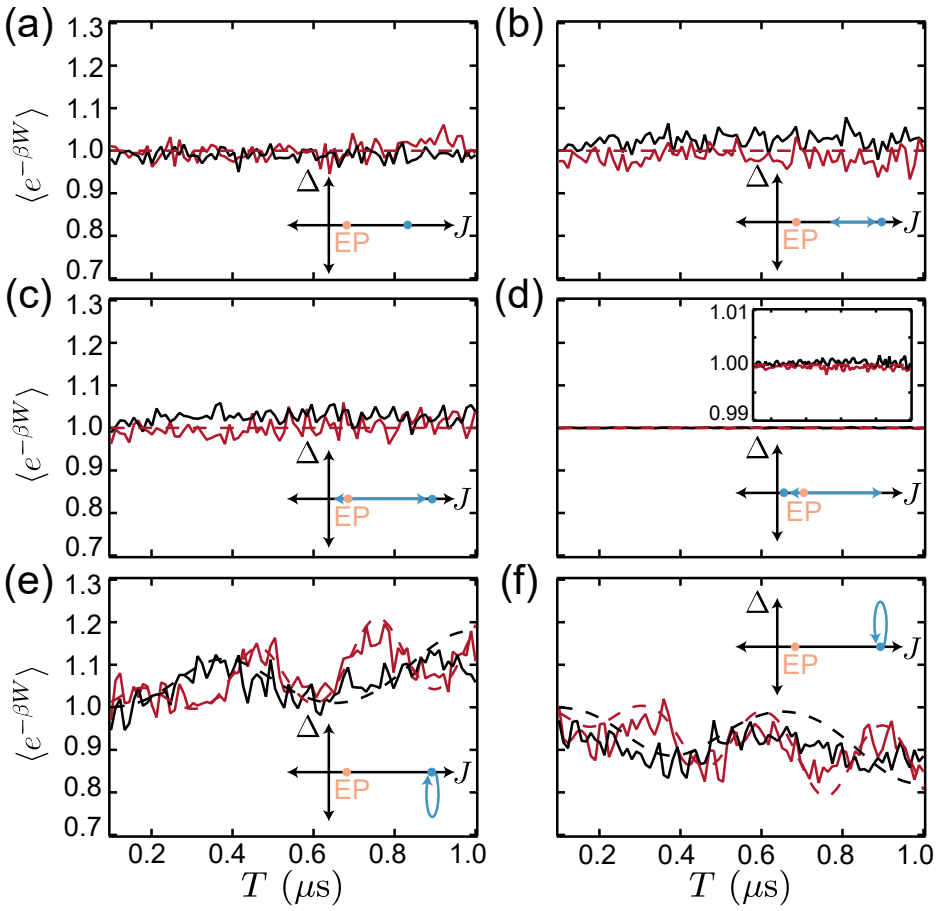

Figure 4.7: **Jarzynski equality evaluated for different paths.** Eq. (4.28) evaluated at T after evolving with $H_{\text{eff}}(t)$ (solid lines) along with the corresponding simulations (dashed lines). The parameter path taken is displayed in the inset with the EP placed at $J_{\text{EP}} = \gamma/4$. (a)-(d) $\Delta_{\max} = 0$ and $J(t)$ (4.25) is varied with $J_{\max} = 3.74$ rad/μs (red trace) or $J_{\max} = 1.89$ rad/μs (black trace). These paths all satisfy (4.7). (a) Is the static case in the $\mathcal{PT}$ symmetric regime with $J_{\max} = J_{\min}$. (b) Is a path varied within the $\mathcal{PT}$ symmetric regime with $J_{\min} = 0.5 J_{\max}$. (c) Begins in the $\mathcal{PT}$ symmetric regime and goes down to $J_{\min} = 0$ in the broken regime. (d) Begins in the $\mathcal{PT}$ symmetric broken regime at $J_{\min} = 0.04$ rad/μs and is varied through the EP and back. (e),(f) In these loops, $\mathcal{PT}$ symmetry is explicitly broken with the path $\Delta_1(t)$ (4.26) where $\Delta_{\max} = \mp 10\pi$ rad/μs (red trace) and $\Delta_{\max} = \mp 2\pi$ rad/μs (black trace) and $J_{\max} = 3.74$ rad/μs for all. (4.7) is not satisfied.

(where $0.5J_{\max} > J_{\text{EP}}$). In Fig. 4.7c we cross the EP into the broken $\mathcal{PT}$ symmetric region until $J_{\min} = 0$. In Fig. 4.7d we begin at $J = 0.04$ rad/μs and reach the maximum at $J_{\max} = 3.74$ rad/μs (red trace) and $J_{\max} = 1.89$ rad/μs (black trace). Similarly, in Figs. 4.7b-d, we observe $\langle e^{-\beta W} \rangle \simeq 1$. What these first four paths have in common is that H_{eff} obeys an explicit $\mathcal{PT}$ symmetry, thus ensuring real or complex-conjugate eigenvalues throughout the evolution (Fig. 2.4). This provides us with a balanced gain and loss between eigenstates.

Figure 4.7e and f correspond to single sided loops where $\Delta_{\max}(t) \neq 0$ in Eq. (4.26). Figure 4.7f displays Eq. (4.28) for the transition probabilities obtained in Fig. 4.6b in the red trace. The asymmetry in the transition probabilities has manifested as a violation in the Jarzynski equality ((4.7)). In these loops $H_{\text{eff}}(t)$ does not obey $\mathcal{PT}$ symmetry. Therefore, we see that $\langle e^{-\beta \Delta U} \rangle \neq 1$ over different loop times T. In these cases $Q \neq 0$, so our TPM protocol gives us $\Delta U = W + Q$.

The final case we explore experimentally are those with loops in Eq. (4.27). This is an interesting case in which $H_{\text{eff}}(t)$ does not explicitly obey $\mathcal{PT}$ symmetry, however the Floquet energy operator, H^F does at certain loop times. We can begin with a similar analysis as before by looking at the transition probabilities. In Fig. 4.8a we see that the symmetry between state survival or transition is recovered at two points, $T_1 = 0.455$ and $T_2 = 0.572$ μs. We look at this by taking the difference between the survival probabilities $\Delta P(T) = P_{++} - P_{--}$ (brown) and transition probabilities $\Delta P(T) = P_{+-} - P_{-+}$ (orange). The curved dashed line is simulation and the straight line at 0 indicates when the probabilities are symmetric. This experiment was performed with the parameters along the red line on Fig. 4.8b. Here, $\Delta_{\max}$ is swept from 0 to 20π rad/μs and loop time T from 0 to 2 μs. The black dashed contours correspond to when $\langle e^{-\beta W} \rangle = 1$. In Fig. 4.8c we evaluate (4.28) with these transition probabilities. Fig. 4.8d provides a zoomed in view taken with more points to resolve the notable region better. Indeed we see that $\langle e^{\beta W} \rangle = 1$ at T_1 and T_2. These two spots correspond to loops with emergent $\mathcal{PT}$ symmetry where H^F_{eff} is $\mathcal{PT}$ symmetric. The balanced gain and loss throughout the loop is recovered, and $Q_{\text{net}} = 0$.

4.4 Numerical simulations exploring non-cyclic paths

The Floquet analysis allowed validation for a group of closed loops that wouldn't have initially intuitively validated the Jarzynski equality with the TPM protocol. To further

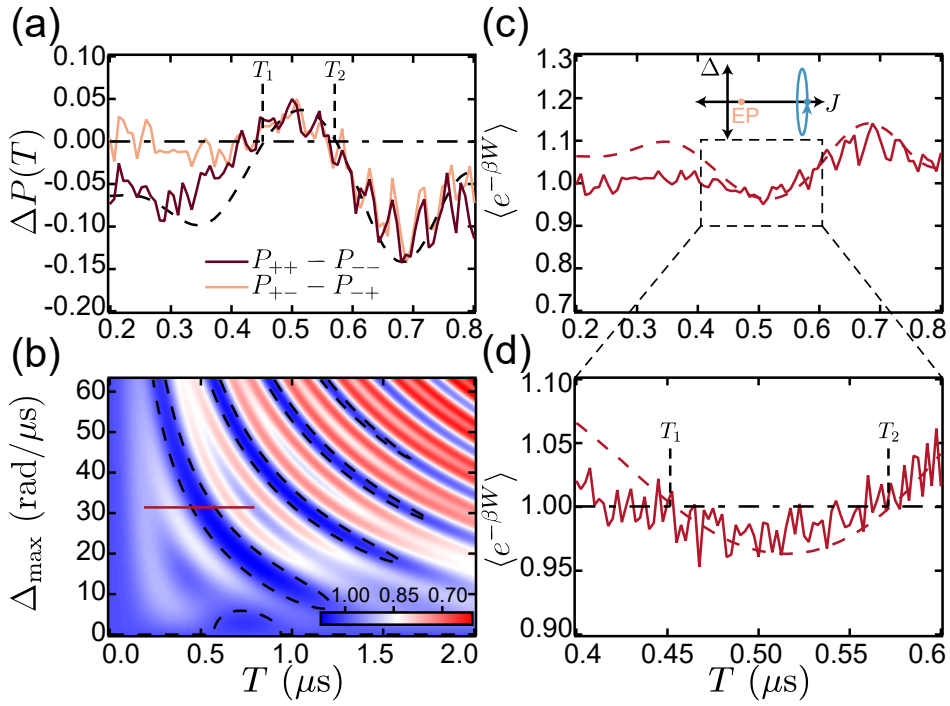

Figure 4.8: **Emergent parity-time symmetry.** The Hamiltonian $H_{\text{eff}}(t)$ is varied according to $\Delta_2(t)$ which is symmetric about the x-axis and $J_{\max} = J_{\min} = 3.74$ rad/μs. (a) The difference of the transition probabilities is plotted as a function of loop time T for $\Delta_{\max} = 10\pi$ rad/μs. $\Delta P(T) = P_{++} - P_{--}$ (brown) and $\Delta P(T) = P_{+-} - P_{-+}$ (orange) are nonzero except at loop times $T_1 = 0.455$ μs and $T_2 = 0.572$ μs (b) Eq. (4.28) evaluated in simulation while changing $\Delta_{\max}$ and loop time T in $\Delta_2(t)$. The black dashed lines correspond to where $\langle e^{-\beta W} \rangle = 1$ and where H^F is in the same basis as H(0). The red line corresponds to the loop taken for (a) and (c). (c) The Jarzynski equality is evaluated with the TPM results. Zooming into the region around $T = 0.5$ μs, we see that it crosses the $e^{-\beta \Delta F} = 1$ line at T_1 and T_2. $\Delta_{\max}$ (rad/μs)

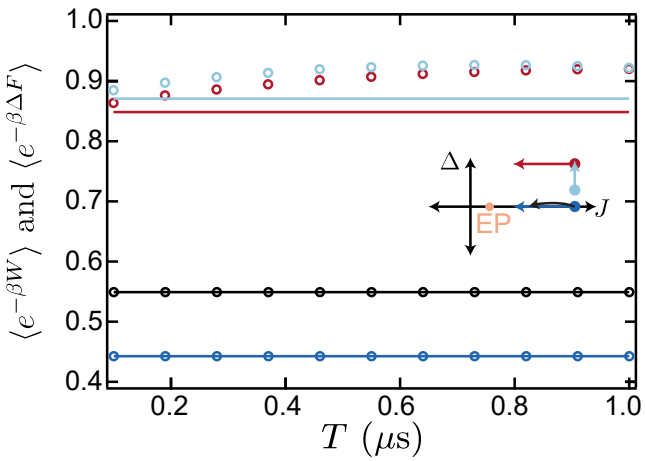

Figure 4.9: **Jarzynski equality evaluated for non-cyclic paths.** $\langle e^{-\beta W}\rangle$ and $\langle e^{-\beta \Delta F}\rangle$ plotted at various periods T for four different paths (i)-(iv) where $Z(0) \neq Z(T)$. (i) J is varied linearly from $J_{\max} = 3.74$ rad/μs down to $J_{\min} = J_{\max}/2$ with $\Delta_{\max} = 0$ (dark blue). (ii) The same path as (i) but with $J_{\min} = J_{\max}/4$ (black). (iii) $\Delta_{\max} = 10\pi$ rad/μs but same $J(t)$ as (i) (red). The final case (iv) varies $\Delta_{\max}$ from 6π rad/μs to 10π rad/μs (light blue). The solid lines correspond to the RHS of (4.7) and the markers to the LHS of (4.7).

extend the applicability of this protocol, this section will show simulation results of paths where $H(0) \neq H(T)$ [155]. Figure 4.9 shows four different paths. (i) In the $\mathcal{PT}$ symmetric regime, with $J_{\max} = 3.74$ rad/μs, $J_{\min} = J_{\max}/2$, $\Delta_{\max} = 0$ (dark blue). (ii) The same path as (i) but with $J_{\min} = J_{\max}/4$ (black). (iii) Is in a region where $H_{\text{eff}}(t)$ does not obey $\mathcal{PT}$ symmetry with $\Delta_{\max} = 10\pi$ rad/μs but same $J(t)$ as (i) (red). The final case (iv) also breaks the $\mathcal{PT}$ symmetry, varying $\Delta_{\max}$ from 6π rad/μs to 10π rad/μs (light blue). All of the solid lines correspond to the RHS of (4.7). For the paths in (i) and (ii) where the initial and final energy basis states are the same $[H(0), H(T)] = 0$, the equality (4.7) is satisfied. For (iii) and (iv), $[H(0), H(T)] \neq 0$, and the equality (4.7) is not satisfied

4.5 Conclusion - discussion of net heat

In this section, we will connect our experimental results back to the initial discussion of the first law, which states that energy cannot be created or destroyed, and $\mathcal{PT}$ symmetry, which defines the condition where the total energy flux equals zero, even if there is gain and loss within a system. Given that we are using the TPM protocol in an open quantum system, we

are obtaining ΔU [34, 36, 35, 40, 41, 42]. Previous explorations of applying the TPM in non-Hermitian systems obeying $\mathcal{PT}$ symmetry had found violations of the Jarzynski equality. However, this is due to previous notions that the effective non-Hermitian Hamiltonian also represents allowed energies [146, 147, 148, 149, 150, 151]. In our protocol, we split the responsibilities of the Hamiltonian H_{eff} such that the Hermitian part serves as our projective measurement basis $H(t)$ while the full Hamiltonian governs the time-dependent dynamics $G(T) = \mathbb{T}\exp\left[-i\int_0^T H_{\text{eff}}(t')dt'\right]$. As we saw earlier in Chapter 2, the loss in our system is due to decay from $|e\rangle \rightarrow |g\rangle$ in the form of $-i\gamma/2|e\rangle\langle e|$. When we extract an overall background loss term $-i\gamma/4\mathbb{I}$, we are left with $+i\gamma/4|f\rangle\langle f|$ (gain) and $-i\gamma/4|e\rangle\langle e|$ (loss). In quantum systems, we quantify our energies through populations/probabilities of the energy states. Therefore, we can think of this as balanced heat flow in and out of the eigenstates, $Q_{\text{net}} = 0$, and the net probability flux is zero (Sec. 2.2). Our protocol applied work to our system by varying the Hamiltonian parameters as a function of time. In the cases with violations, the heat in our measurement comes in the form of irreversible "classical" heat [42, 156]. These cases are those where $\mathcal{PT}$ symmetry is explicitly (and in the Floquet picture) broken. This results in an imbalance of loss among the eigenstates over the loop because they are not complex conjugates of each other, as was demonstrated in the survival and transition probabilities of Fig. 4.6b. The imaginary component corresponds to relative gain/loss, which is a result of the non-Hermitian Hamiltonian.

Chapter 5

Conclusions and Future Directions

In this thesis, we were able to better understand and harness the complex energy spectrum resulting from our non-Hermitian Hamiltonian. While many protocols, such as counterdiabatic driving and the two-projective measurement protocol (TPM), were originally derived for Hermitian systems, we were able to extend them to non-Hermitian ones in Chapters 3 and 4. In Chapter 2, we built out the math underlying the non-Hermitian Hamiltonian and discussed what to expect from experimental measurements, followed by observing the EP transition and encircling of this EP. The resulting breakdown in adiabaticity, which caused non-adiabatic transitions and loss at longer times, motivated the exploration of shortcuts to adiabaticity (STA) in the next Chapter. In Chapter 3, we were able to explore in depth the consequences of non-orthogonality of our eigenstates and found encircling paths called Apollonius circles that provided a Hermitian counterdiabatic drive, with the limiting factor being whether $\dot{\alpha}_{\mathrm{I}} = 0$. Another method of Hermitian counterdiabatic driving was introduced that chooses a projector that keeps the state within the intended subspace. This method was experimentally verified and performed similarly to the previous one. These two methods provide avenues for future research in non-Hermitian quantum control for other platforms and Hamiltonians.

Future directions can explore higher-order exceptional points as they offer numerous ways of encircling EPs and EP lines. Since decoherence remains an issue for longer encircling loops, future directions will attempt to mitigate errors due to known dephasing parameters (γ_ϕ), thus expanding the total drive times for which counterdiabatic driving maintains the instantaneous eigenstate. Future research can also extend shortcuts to adiabaticity to multiple qubits to generate entangled states [157, 158, 159].

In Chapter 4, we better understood the role of the non-Hermitian Hamiltonian in energetics and dynamics: roles that were previously conflated and resulted in predicted violations of the Jarzynski equality in certain regions [146, 147, 148, 149, 151]. In this experiment, we

were able to show that as long as the Hamiltonian obeyed $\mathcal{PT}$-symmetry explicitly or in the Floquet picture, the Hermitian part of the Hamiltonian acts as the internal energy operator, and the net heat vanishes, verifying the Jarzynski equality. We performed projective measurements in the Hermitian basis, which gave us real, allowed energies, while the non-Hermitian Hamiltonian governed the time evolution. The Jarzynski equality was previously verified in isolated quantum systems [152] and decohering systems (no dissipation) [143] since the TPM protocol gives measurements of internal energy where $Q = 0$. Previous tests of the Jarzynski equality have offered corrections for the energetic cost of information, monitoring, feedback, and the measurement process [160, 39, 161, 144, 162, 30]. A fully comprehensive measurement scheme or correction to the Jarzynski equality remains an open question in this field for dissipative non-Hermitian Hamiltonians that don't obey $\mathcal{PT}$ symmetry (Floquet or explicit).

We hope that this thesis provides some insight through a better understanding of how non-Hermitian Hamiltonians function. By exploring the parameter space both in terms of the topology of the Riemann sheets and the regions of $\mathcal{PT}$-symmetry, we better understand how gain and loss affect our dynamics and measurements. This research provides future avenues of exploration that can utilize systems described by non-Hermitian Hamiltonians for state preparation (single or multi-qubit), thermodynamic engines, or computational protocols.

References

[1] Mahdi Naghiloo. *Introduction to Experimental Quantum Measurement with Superconducting Qubits*. PhD thesis, Washington University in St. Louis, 2019.

[2] Alec Yen, Yufeng Ye, Kaidong Peng, Jennifer Wang, Gregory Cunningham, Michael Gingras, Bethany M. Niedzielski, Hannah Stickler, Kyle Serniak, Mollie E. Schwartz, and Kevin P. O'Brien. Interferometric Purcell suppression of spontaneous emission in a superconducting qubit. *Physical Review Applied*, 23(2), February 2025.

[3] M. D. Reed, B. R. Johnson, A. A. Houck, L. DiCarlo, J. M. Chow, D. I. Schuster, L. Frunzio, and R. J. Schoelkopf. Fast reset and suppressing spontaneous emission of a superconducting qubit. *Applied Physics Letters*, 96(20), May 2010.

[4] M. D. Reed, L. DiCarlo, B. R. Johnson, L. Sun, D. I. Schuster, L. Frunzio, and R. J. Schoelkopf. High-fidelity readout in circuit quantum electrodynamics using the Jaynes-Cummings nonlinearity. *Physical Review Letters*, 105(17), October 2010.

[5] Evan Jeffrey, Daniel Sank, J.Y. Mutus, T.C. White, J. Kelly, R. Barends, Y. Chen, Z. Chen, B. Chiaro, A. Dunsworth, A. Megrant, P.J.J. O'Malley, C. Neill, P. Roushan, A. Vainsencher, J. Wenner, A.N. Cleland, and John M. Martinis. Fast accurate state measurement with superconducting qubits. *Physical Review Letters*, 112(19), May 2014.

[6] Eyob A. Sete, John M. Martinis, and Alexander N. Korotkov. Quantum theory of a bandpass Purcell filter for qubit readout. *Physical Review A*, 92(1), July 2015.

[7] Google Quantum AI and Collaborators. Suppressing quantum errors by scaling a surface code logical qubit. *Nature*, 614(7949):676–681, February 2023.

[8] Google Quantum AI and Collaborators. Quantum error correction below the surface code threshold. *Nature*, 638(8052):920–926, December 2024.

[9] Kevin C. Miao, Matt McEwen, Juan Atalaya, et al. Overcoming leakage in quantum error correction. *Nature Physics*, 19(12):1780–1786, October 2023.

[10] Sebastian Krinner, Nathan Lacroix, Ants Remm, Agustin Di Paolo, Elie Genois, Catherine Leroux, Christoph Hellings, Stefania Lazar, Francois Swiadek, Johannes Herrmann, Graham J. Norris, Christian Kraglund Andersen, Markus Müller, Alexandre Blais, Christopher Eichler, and Andreas Wallraff. Realizing repeated quantum error correction in a distance-three surface code. *Nature*, 605(7911):669–674, May 2022.

[11] Sergey Bravyi, Andrew W. Cross, Jay M. Gambetta, Dmitri Maslov, Patrick Rall, and Theodore J. Yoder. High-threshold and low-overhead fault-tolerant quantum memory. *Nature*, 627(8005):778–782, March 2024.

[12] F. Motzoi, J. M. Gambetta, P. Rebentrost, and F. K. Wilhelm. Simple pulses for elimination of leakage in weakly nonlinear qubits. *Physical Review Letters*, 103(11), September 2009.

[13] J. M. Gambetta, F. Motzoi, S. T. Merkel, and F. K. Wilhelm. Analytic control methods for high-fidelity unitary operations in a weakly nonlinear oscillator. *Physical Review A*, 83(1), January 2011.

[14] Xingrui Song. *Entanglement-Enhanced Metrology With Superconducting Circuits*. PhD thesis, Washington University in St. Louis, 2025.

[15] H. Xu, D. Mason, Luyao Jiang, and J. G. E. Harris. Topological energy transfer in an optomechanical system with exceptional points. *Nature*, 537(7618):80–83, July 2016.

[16] Maryam Abbasi, Weijian Chen, Mahdi Naghiloo, Yogesh N. Joglekar, and Kater W. Murch. Topological quantum state control through exceptional-point proximity. *Physical Review Letters*, 128(16), April 2022.

[17] S. Ebadi, A. Keesling, M. Cain, T. T. Wang, H. Levine, D. Bluvstein, G. Semeghini, A. Omran, J.-G. Liu, R. Samajdar, X.-Z. Luo, B. Nash, X. Gao, B. Barak, E. Farhi, S. Sachdev, N. Gemelke, L. Zhou, S. Choi, H. Pichler, S.-T. Wang, M. Greiner, V. Vuletić, and M. D. Lukin. Quantum optimization of maximum independent set using Rydberg atom arrays. *Science*, 376(6598):1209–1215, June 2022.

[18] Tosio Kato. On the adiabatic theorem of quantum mechanics. *Journal of the Physical Society of Japan*, 5(6):435–439, November 1950.

[19] G Nenciu. On the adiabatic theorem of quantum mechanics. *Journal of Physics A: Mathematical and General*, 13(2):L15–L18, February 1980.

[20] M. Naghiloo, M. Abbasi, Yogesh N. Joglekar, and K. W. Murch. Quantum state tomography across the exceptional point in a single dissipative qubit. *Nature Physics*, 15(12):1232–1236, October 2019.

[21] Chitres Guria, Qi Zhong, Sahin Kaya Ozdemir, Yogesh S. S. Patil, Ramy El-Ganainy, and Jack Gwynne Emmet Harris. Resolving the topology of encircling multiple exceptional points. *Nature Communications*, 15(1), February 2024.

[22] Jörg Doppler, Alexei A. Mailybaev, Julian Böhm, Ulrich Kuhl, Adrian Girschik, Florian Libisch, Thomas J. Milburn, Peter Rabl, Nimrod Moiseyev, and Stefan Rotter. Dynamically encircling an exceptional point for asymmetric mode switching. *Nature*, 537(7618):76–79, July 2016.

[23] Aodong Li, Jianji Dong, Jian Wang, Ziwei Cheng, John S. Ho, Dawei Zhang, Jing Wen, Xu-Lin Zhang, C.T. Chan, Andrea Alù, Cheng-Wei Qiu, and Lin Chen. Hamiltonian hopping for efficient chiral mode switching in encircling exceptional points. *Physical Review Letters*, 125(18), October 2020.

[24] Aodong Li, Weijin Chen, Heng Wei, Guowei Lu, Andrea Alù, Cheng-Wei Qiu, and Lin Chen. Riemann-encircling exceptional points for efficient asymmetric polarization-locked devices. *Physical Review Letters*, 129(12), September 2022.

[25] Wenquan Liu, Yang Wu, Chang-Kui Duan, Xing Rong, and Jiangfeng Du. Dynamically encircling an exceptional point in a real quantum system. *Physical Review Letters*, 126(17), April 2021.

[26] Huixia Gao, Konghao Sun, Dengke Qu, Kunkun Wang, Lei Xiao, Wei Yi, and Peng Xue. Photonic chiral state transfer near the Liouvillian exceptional point, 2025.

[27] K. Ho, S. Perna, S. Wittrock, S. Tsunegi, H. Kubota, S. Yuasa, P. Bortolotti, M. d'Aquino, C. Serpico, V. Cros, and R. Lebrun. Controlling encirclement of an exceptional point using coupled spintronic nano-oscillators, 2024.

[28] Mustafa Demirplak and Stuart A. Rice. Adiabatic population transfer with control fields. *The Journal of Physical Chemistry A*, 107(46):9937–9945, October 2003.

[29] M V Berry. Transitionless quantum driving. *Journal of Physics A: Mathematical and Theoretical*, 42(36):365303, August 2009.

[30] Xiayu Linpeng, Léa Bresque, Maria Maffei, Andrew N. Jordan, Alexia Auffèves, and Kater W. Murch. Energetic cost of measurements using quantum, coherent, and thermal light. *Physical Review Letters*, 128(22), June 2022.

[31] M. Naghiloo, D. Tan, P. M. Harrington, J. J. Alonso, E. Lutz, A. Romito, and K. W. Murch. Heat and work along individual trajectories of a quantum bit. *Phys. Rev. Lett.*, 124:110604, Mar 2020.

[32] Sebastian Deffner, Juan Pablo Paz, and Wojciech H. Zurek. Quantum work and the thermodynamic cost of quantum measurements. *Physical Review E*, 94(1), July 2016.

[33] P. Kammerlander and J. Anders. Coherence and measurement in quantum thermodynamics. *Scientific Reports*, 6(1), February 2016.

[34] R Alicki. The quantum open system as a model of the heat engine. *Journal of Physics A: Mathematical and General*, 12(5):L103–L107, May 1979.

[35] Herbert Spohn and Joel L. Lebowitz. Irreversible thermodynamics for quantum systems weakly coupled to thermal reservoirs. In *Advances in Chemical Physics*, pages 109–142. John Wiley & Sons, Inc., March 2007.

[36] Ronnie Kosloff. A quantum mechanical open system as a model of a heat engine. *The Journal of Chemical Physics*, 80(4):1625–1631, February 1984.

[37] B. Leggio, A. Napoli, A. Messina, and H.-P. Breuer. Entropy production and information fluctuations along quantum trajectories. *Physical Review A*, 88(4), October 2013.

[38] F. W. J. Hekking and J. P. Pekola. Quantum jump approach for work and dissipation in a two-level system. *Phys. Rev. Lett.*, 111:093602, Aug 2013.

[39] Zongping Gong, Yuto Ashida, and Masahito Ueda. Quantum-trajectory thermodynamics with discrete feedback control. *Phys. Rev. A*, 94:012107, Jul 2016.

[40] Jordan M. Horowitz. Quantum-trajectory approach to the stochastic thermodynamics of a forced harmonic oscillator. *Physical Review E*, 85(3), March 2012.

[41] Jose Joaquin Alonso, Eric Lutz, and Alessandro Romito. Thermodynamics of weakly measured quantum systems. *Phys. Rev. Lett.*, 116:080403, Feb 2016.

[42] Cyril Elouard, David A. Herrera-Martí, Maxime Clusel, and Alexia Auffèves. The role of quantum measurement in stochastic thermodynamics. *npj Quantum Inf*, 3(9), mar 2017.

[43] Léa Bresque, Patrice A. Camati, Spencer Rogers, Kater Murch, Andrew N. Jordan, and Alexia Auffèves. Two-qubit engine fueled by entanglement and local measurements. *Physical Review Letters*, 126(12), March 2021.

[44] C. Jarzynski. Nonequilibrium equality for free energy differences. *Physical Review Letters*, 78(14):2690–2693, April 1997.

[45] Jens Koch, Terri M. Yu, Jay Gambetta, A. A. Houck, D. I. Schuster, J. Majer, Alexandre Blais, M. H. Devoret, S. M. Girvin, and R. J. Schoelkopf. Charge-insensitive qubit design derived from the cooper pair box. *Phys. Rev. A*, 76:042319, Oct 2007.

[46] David Isaac Schuster. *Circuit Quantum Electrodynamics*. PhD thesis, Yale University, 2007.

[47] Daniel Sank. *Fast, Accurate State Measurement in Superconducting Qubits*. PhD thesis, University of California Santa Barbara, 2014.

[48] Steven Weber. *Quantum Trajectories of a Superconducting Qubit*. PhD thesis, University of California, Berkeley, 2014.

[49] S. Ibáñez, S. Martínez-Garaot, Xi Chen, E. Torrontegui, and J. G. Muga. Shortcuts to adiabaticity for non-Hermitian systems. *Physical Review A*, 84(2), August 2011.

[50] S. Ibáñez and J. G. Muga. Adiabaticity condition for non-hermitian hamiltonians. *Physical Review A*, 89(3), March 2014.

[51] Carl M. Bender and Stefan Boettcher. Real spectra in non-Hermitian Hamiltonians having PT symmetry. *Physical Review Letters*, 80(24):5243–5246, June 1998.

[52] Carl M. Bender. *PT Symmetry in Quantum and Classical Physics*. World Scientific Publishing Europe Ltd., Singapore, Hackensack, NJ, 2018.

[53] Maryam Abbasi. *Experimental Investigation of Non-Hermiticity in Quantum Systems*. PhD thesis, Washington University in St. Louis, 2023.

[54] Ramy El-Ganainy, Konstantinos G Makris, Mercedeh Khajavikhan, Ziad H Musslimani, Stefan Rotter, and Demetrios N Christodoulides. Non-Hermitian physics and PT symmetry. *Nature Physics*, 14(1):11, 2018.

[55] Liang Feng, Ye-Long Xu, William S. Fegadolli, Ming-Hui Lu, José E. B. Oliveira, Vilson R. Almeida, Yan-Feng Chen, and Axel Scherer. Experimental demonstration of a unidirectional reflectionless parity-time metamaterial at optical frequencies. *Nature Materials*, 12(2):108–113, November 2012.

[56] Liang Feng, Ramy El-Ganainy, and Li Ge. Non-Hermitian photonics based on parity-time symmetry. *Nature Photonics*, 11(12):752–762, 2017.

[57] A. Guo, G. J. Salamo, D. Duchesne, R. Morandotti, M. Volatier-Ravat, V. Aimez, G. A. Siviloglou, and D. N. Christodoulides. Observation of $\mathcal{PT}$-symmetry breaking in complex optical potentials. *Phys. Rev. Lett.*, 103:093902, Aug 2009.

[58] Christian E. Rüter, Konstantinos G. Makris, Ramy El-Ganainy, Demetrios N. Christodoulides, Mordechai Segev, and Detlef Kip. Observation of parity-time symmetry in optics. *Nature Physics*, 6(3):192–195, January 2010.

[59] Bo Peng, Şahin Kaya Özdemir, Fuchuan Lei, Faraz Monifi, Mariagiovanna Gianfreda, Gui Lu Long, Shanhui Fan, Franco Nori, Carl M. Bender, and Lan Yang. Parity-time-symmetric whispering-gallery microcavities. *Nature Physics*, 10(5):394–398, April 2014.

[60] Hossein Hodaei, Mohammad-Ali Miri, Matthias Heinrich, Demetrios N. Christodoulides, and Mercedeh Khajavikhan. Parity-time-symmetric microring lasers. *Science*, 346(6212):975–978, 2014.

[61] S. Weimann, M. Kremer, Y. Plotnik, Y. Lumer, S. Nolte, K. G. Makris, M. Segev, M. C. Rechtsman, and A. Szameit. Topologically protected bound states in photonic parity–time-symmetric crystals. *Nature Materials*, 16(4):433–438, December 2016.

[62] Yang Wu, Wenquan Liu, Jianpei Geng, Xingrui Song, Xiangyu Ye, Chang-Kui Duan, Xing Rong, and Jiangfeng Du. Observation of parity-time symmetry breaking in a single-spin system. *Science*, 364(6443):878–880, May 2019.

[63] Jiaming Li, Andrew K. Harter, Ji Liu, Leonardo de Melo, Yogesh N. Joglekar, and Le Luo. Observation of parity-time symmetry breaking transitions in a dissipative Floquet system of ultracold atoms. *Nature Communications*, 10(1), February 2019.

[64] John Clarke and Alex I. Braginski. *The SQUID Handbook: Vol. I Fundamentals and Technology of SQUIDs and SQUID Systems*. Wiley-VCH Verlag GmbH and Co. KGaA, 1982.

[65] E. M. Purcell, H. C. Torrey, and R. V. Pound. Resonance absorption by nuclear magnetic moments in a solid. *Physical Review*, 69(1–2):37–38, January 1946.

[66] F. Bloch, W. W. Hansen, and M. Packard. The nuclear induction experiment. *Physical Review*, 70(7–8):474–485, October 1946.

[67] N. Bloembergen, E. M. Purcell, and R. V. Pound. Relaxation effects in nuclear magnetic resonance absorption. *Physical Review*, 73(7):679–712, April 1948.

[68] A. Wallraff, D. I. Schuster, A. Blais, L. Frunzio, J. Majer, M. H. Devoret, S. M. Girvin, and R. J. Schoelkopf. Approaching unit visibility for control of a superconducting qubit with dispersive readout. *Phys. Rev. Lett.*, 95:060501, Aug 2005.

[69] Alexandre Blais, Ren-Shou Huang, Andreas Wallraff, S. M. Girvin, and R. J. Schoelkopf. Cavity quantum electrodynamics for superconducting electrical circuits: An architecture for quantum computation. *Physical Review A*, 69(6), June 2004.

[70] P. Krantz, M. Kjaergaard, F. Yan, T. P. Orlando, S. Gustavsson, and W. D. Oliver. A quantum engineer's guide to superconducting qubits. *Applied Physics Reviews*, 6(2), June 2019.

[71] Yunzhao Wang. *Quantum Information Processing via Dissipation Engineering in Superconducting Circuit Platform*. PhD thesis, Washington University in St. Louis, 2023.

[72] F. Pedregosa, G. Varoquaux, A. Gramfort, V. Michel, B. Thirion, O. Grisel, M. Blondel, P. Prettenhofer, R. Weiss, V. Dubourg, J. Vanderplas, A. Passos, D. Cournapeau, M. Brucher, M. Perrot, and E. Duchesnay. Scikit-learn: Machine learning in Python. *Journal of Machine Learning Research*, 12:2825–2830, 2011.

[73] Lars Buitinck, Gilles Louppe, Mathieu Blondel, Fabian Pedregosa, Andreas Mueller, Olivier Grisel, Vlad Niculae, Peter Prettenhofer, Alexandre Gramfort, Jaques Grobler, Robert Layton, Jake VanderPlas, Arnaud Joly, Brian Holt, and Gaël Varoquaux. API design for machine learning software: experiences from the scikit-learn project. In *ECML PKDD Workshop: Languages for Data Mining and Machine Learning*, pages 108–122, 2013.

[74] Jochen Braumüller, Leon Ding, Antti P. Vepsäläinen, Youngkyu Sung, Morten Kjaergaard, Tim Menke, Roni Winik, David Kim, Bethany M. Niedzielski, Alexander

Melville, Jonilyn L. Yoder, Cyrus F. Hirjibehedin, Terry P. Orlando, Simon Gustavsson, and William D. Oliver. Characterizing and optimizing qubit coherence based on squid geometry. *Physical Review Applied*, 13(5), May 2020.

[75] Hossein Hodaei, Absar U. Hassan, Steffen Wittek, Hipolito Garcia-Gracia, Ramy El-Ganainy, Demetrios N. Christodoulides, and Mercedeh Khajavikhan. Enhanced sensitivity at higher-order exceptional points. *Nature*, 548(7666):187–191, August 2017.

[76] Weijian Chen, Şahin Kaya Özdemir, Guangming Zhao, Jan Wiersig, and Lan Yang. Exceptional points enhance sensing in an optical microcavity. *Nature*, 548(7666):192–196, August 2017.

[77] Akhil Kumar, Kater W. Murch, and Yogesh N. Joglekar. Maximal quantum entanglement at exceptional points via unitary and thermal dynamics. *Physical Review A*, 105(1), January 2022.

[78] Weijian Chen, Maryam Abbasi, Yogesh N. Joglekar, and Kater W. Murch. Quantum jumps in the non-Hermitian dynamics of a superconducting qubit. *Physical Review Letters*, 127(14), September 2021.

[79] Eva-Maria Graefe, Alexei A. Mailybaev, and Nimrod Moiseyev. Breakdown of adiabatic transfer of light in waveguides in the presence of absorption. *Physical Review A*, 88(3), September 2013.

[80] Serra Erdamar, Maryam Abbasi, Weijian Chen, Niklas Hörnedal, Aurélia Chenu, and Kater W. Murch. Exploring the topology of a non-Hermitian superconducting qubit using shortcuts to adiabaticity, 2025.

[81] M. V. Berry. Quantal phase factors accompanying adiabatic changes. *Proceedings of the Royal Society of London. Series A, Mathematical and Physical Sciences*, 392(1802):45–57, 1984.

[82] S. Pancharatnam. Generalized theory of interference, and its applications: Part i. coherent pencils. *Proceedings of the Indian Academy of Sciences - Section A*, 44(5):247–262, November 1956.

[83] Ieva Čepaitė. *Counterdiabatic, Better, Faster, Stronger*. PhD thesis, University of Strathclyde, Glasgow, 2024.

[84] Ido Gilary, Alexei A. Mailybaev, and Nimrod Moiseyev. Time-asymmetric quantum-state-exchange mechanism. *Physical Review A*, 88(1), July 2013.

[85] Raam Uzdin, Alexei Mailybaev, and Nimrod Moiseyev. On the observability and asymmetry of adiabatic state flips generated by exceptional points. *Journal of Physics A: Mathematical and Theoretical*, 44(43):435302, October 2011.

[86] D. Guéry-Odelin, A. Ruschhaupt, A. Kiely, E. Torrontegui, S. Martínez-Garaot, and J. G. Muga. Shortcuts to adiabaticity: Concepts, methods, and applications. *Reviews of Modern Physics*, 91(4), October 2019.

[87] Erik Torrontegui, Sara Ibáñez, Sofia Martínez-Garaot, Michele Modugno, Adolfo del Campo, David Guéry-Odelin, Andreas Ruschhaupt, Xi Chen, and Juan Gonzalo Muga. *Shortcuts to Adiabaticity*, page 117–169. Elsevier, 2013.

[88] Xi Chen, I. Lizuain, A. Ruschhaupt, D. Guéry-Odelin, and J. G. Muga. Shortcut to adiabatic passage in two- and three-level atoms. *Physical Review Letters*, 105(12), September 2010.

[89] Mark G. Bason, Matthieu Viteau, Nicola Malossi, Paul Huillery, Ennio Arimondo, Donatella Ciampini, Rosario Fazio, Vittorio Giovannetti, Riccardo Mannella, and Oliver Morsch. High-fidelity quantum driving. *Nature Physics*, 8(2):147–152, December 2011.

[90] Christopher Jarzynski. Generating shortcuts to adiabaticity in quantum and classical dynamics. *Physical Review A*, 88(4), October 2013.

[91] Adolfo del Campo. Shortcuts to adiabaticity by counterdiabatic driving. *Physical Review Letters*, 111(10), September 2013.

[92] Ieva Čepaitė, Anatoli Polkovnikov, Andrew J. Daley, and Callum W. Duncan. Counterdiabatic optimized local driving. *PRX Quantum*, 4:010312, Jan 2023.

[93] Stewart Morawetz and Anatoli Polkovnikov. Efficient paths for local counterdiabatic driving, 2024.

[94] Sebastian Deffner, Christopher Jarzynski, and Adolfo del Campo. Classical and quantum shortcuts to adiabaticity for scale-invariant driving. *Physical Review X*, 4(2), April 2014.

[95] Shuoming An, Dingshun Lv, Adolfo del Campo, and Kihwan Kim. Shortcuts to adiabaticity by counterdiabatic driving for trapped-ion displacement in phase space. *Nature Communications*, 7(1), September 2016.

[96] Yan-Xiong Du, Zhen-Tao Liang, Yi-Chao Li, Xian-Xian Yue, Qing-Xian Lv, Wei Huang, Xi Chen, Hui Yan, and Shi-Liang Zhu. Experimental realization of stimulated raman shortcut-to-adiabatic passage with cold atoms. *Nature Communications*, 7(1), August 2016.

[97] Jingfu Zhang, Jeong Hyun Shim, Ingo Niemeyer, T. Taniguchi, T. Teraji, H. Abe, S. Onoda, T. Yamamoto, T. Ohshima, J. Isoya, and Dieter Suter. Experimental implementation of assisted quantum adiabatic passage in a single spin. *Physical Review Letters*, 110(24), June 2013.

[98] Michael A Nielsen and Issac L Chuang. *Quantum computation and quantum information*. Cambridge University Press, Cambridge New York, 2000.

[99] Akira Tomita and Raymond Y. Chiao. Observation of Berry's topological phase by use of an optical fiber. *Physical Review Letters*, 57(8):937–940, August 1986.

[100] Alexei A. Mailybaev, Oleg N. Kirillov, and Alexander P. Seyranian. Geometric phase around exceptional points. *Physical Review A*, 72(1):014104, July 2005.

[101] J. Höller, N. Read, and J. G. E. Harris. Non-Hermitian adiabatic transport in spaces of exceptional points. *Phys. Rev. A*, 102:032216, Sep 2020.

[102] P. J. Leek, J. M. Fink, A. Blais, R. Bianchetti, M. Goppl, J. M. Gambetta, D. I. Schuster, L. Frunzio, R. J. Schoelkopf, and A. Wallraff. Observation of Berry's phase in a solid-state qubit. *Science*, 318(5858):1889–1892, December 2007.

[103] S. Berger, M. Pechal, A. A. Abdumalikov, C. Eichler, L. Steffen, A. Fedorov, A. Wallraff, and S. Filipp. Exploring the effect of noise on the Berry phase. *Physical Review A*, 87(6), June 2013.

[104] S. Filipp, J. Klepp, Y. Hasegawa, C. Plonka-Spehr, U. Schmidt, P. Geltenbort, and H. Rauch. Experimental demonstration of the stability of Berry's phase for a spin-1/2 particle. *Physical Review Letters*, 102(3), January 2009.

[105] Terumichi Ohashi, Shingo Kobayashi, and Yuki Kawaguchi. Generalized Berry phase for a bosonic Bogoliubov system with exceptional points. *Physical Review A*, 101(1), January 2020.

[106] Raymond Y. Chiao and Yong-Shi Wu. Manifestations of Berry's topological phase for the photon. *Physical Review Letters*, 57(8):933–936, August 1986.

[107] Zhenxing Zhang, Tenghui Wang, Liang Xiang, Jiadong Yao, Jianlan Wu, and Yi Yin. Measuring the Berry phase in a superconducting phase qubit by a shortcut to adiabaticity. *Physical Review A*, 95(4), April 2017.

[108] Paolo Zanardi and Mario Rasetti. Holonomic quantum computation. *Physics Letters A*, 264(2–3):94–99, December 1999.

[109] Erik Sjöqvist, D M Tong, L Mauritz Andersson, Björn Hessmo, Markus Johansson, and Kuldip Singh. Non-adiabatic holonomic quantum computation. *New Journal of Physics*, 14(10):103035, October 2012.

[110] J. R. Lane, C. Guria, J. Höller, T. D. Montalvo, Y. S. S. Patil, and J. G. E. Harris. Complex Berry phase and steady-state geometric amplification in non-Hermitian systems, 2025.

[111] Yogesh S. S. Patil, Judith Höller, Parker A. Henry, Chitres Guria, Yiming Zhang, Luyao Jiang, Nenad Kralj, Nicholas Read, and Jack G. E. Harris. Measuring the knot of non-Hermitian degeneracies and non-commuting braids. *Nature*, 607(7918):271–275, July 2022.

[112] Pei-Rong Han, Wen Ning, Xin-Jie Huang, Ri-Hua Zheng, Shou-Bang Yang, Fan Wu, Zhen-Biao Yang, Qi-Ping Su, Chui-Ping Yang, and Shi-Biao Zheng. Measuring topological invariants for higher-order exceptional points in quantum three-mode systems. *Nature Communications*, 15(1), November 2024.

[113] Richard H. Dittman Mark W. Zemansky. *Heat and Thermodynamics*. McGraw-Hill, Inc., 1981.

[114] Randy Harris. *Modern Physics*. Pearson Education, Limited, 2008.

[115] Denis J. Evans, E. G. D. Cohen, and G. P. Morriss. Probability of second law violations in shearing steady states. *Physical Review Letters*, 71(15):2401–2404, October 1993.

[116] Christopher Jarzynski. Equalities and inequalities: Irreversibility and the second law of thermodynamics at the nanoscale. *Annual Review of Condensed Matter Physics*, 2(1):329–351, March 2011.

[117] Denis J. Evans and Debra J. Searles. Equilibrium microstates which generate second law violating steady states. *Physical Review E*, 50(2):1645–1648, August 1994.

[118] Denis J. Evans and Debra J. Searles. The fluctuation theorem. *Advances in Physics*, 51(7):1529–1585, November 2002.

[119] G. Gallavotti and E. G. D. Cohen. Dynamical ensembles in nonequilibrium statistical mechanics. *Physical Review Letters*, 74(14):2694–2697, April 1995.

[120] Jorge Kurchan. Fluctuation theorem for stochastic dynamics. *Journal of Physics A: Mathematical and General*, 31(16):3719–3729, April 1998.

[121] Joel L. Lebowitz and Herbert Spohn. A Gallavotti–Cohen-type symmetry in the large deviation functional for stochastic dynamics. *Journal of Statistical Physics*, 95(1/2):333–365, 1999.

[122] Christian Maes. The fluctuation theorem as a Gibbs property. *Journal of Statistical Physics*, 95(1/2):367–392, 1999.

[123] G. M. Wang, E. M. Sevick, Emil Mittag, Debra J. Searles, and Denis J. Evans. Experimental demonstration of violations of the second law of thermodynamics for small systems and short time scales. *Physical Review Letters*, 89(5), July 2002.

[124] Gavin E. Crooks. Entropy production fluctuation theorem and the nonequilibrium work relation for free energy differences. *Phys. Rev. E*, 60:2721–2726, Sep 1999.

[125] Jan Liphardt, Sophie Dumont, Steven B. Smith, Ignacio Tinoco, and Carlos Bustamante. Equilibrium information from nonequilibrium measurements in an experimental test of Jarzynski's equality. *Science*, 296(5574):1832–1835, June 2002.

[126] D. Collin, F. Ritort, C. Jarzynski, S. B. Smith, I. Tinoco, and C. Bustamante. Verification of the Crooks fluctuation theorem and recovery of RNA folding free energies. *Nature*, 437(7056):231–234, September 2005.

[127] F Douarche, S Ciliberto, A Petrosyan, and I Rabbiosi. An experimental test of the Jarzynski equality in a mechanical experiment. *Europhysics Letters (EPL)*, 70(5):593–599, June 2005.

[128] V. Blickle, T. Speck, L. Helden, U. Seifert, and C. Bechinger. Thermodynamics of a colloidal particle in a time-dependent nonharmonic potential. *Physical Review Letters*, 96(7), February 2006.

[129] Nolan C. Harris, Yang Song, and Ching-Hwa Kiang. Experimental free energy surface reconstruction from single-molecule force spectroscopy using Jarzynski's equality. *Physical Review Letters*, 99(6), August 2007.

[130] Ivan Junier, Alessandro Mossa, Maria Manosas, and Felix Ritort. Recovery of free energy branches in single molecule experiments. *Physical Review Letters*, 102(7), February 2009.

[131] Elizabeth A. Shank, Ciro Cecconi, Jesse W. Dill, Susan Marqusee, and Carlos Bustamante. The folding cooperativity of a protein is controlled by its chain topology. *Nature*, 465(7298):637–640, May 2010.

[132] O.-P. Saira, Y. Yoon, T. Tanttu, M. Möttönen, D. V. Averin, and J. P. Pekola. Test of the Jarzynski and Crooks fluctuation relations in an electronic system. *Physical Review Letters*, 109(18), October 2012.

[133] S Ciliberto, N Garnier, S Hernandez, C Lacpatia, J.-F Pinton, and G Ruiz Chavarria. Experimental test of the Gallavotti–Cohen fluctuation theorem in turbulent flows. *Physica A: Statistical Mechanics and its Applications*, 340(1–3):240–250, September 2004.

[134] Hal Tasaki. Jarzynski relations for quantum systems and some applications, 2000.

[135] G. Hummer and A. Szabo. Free energy reconstruction from nonequilibrium single-molecule pulling experiments. *Proceedings of the National Academy of Sciences*, 98(7):3658–3661, March 2001.

[136] Carlos Bustamante, Jan Liphardt, and Felix Ritort. The nonequilibrium thermodynamics of small systems. *Physics Today*, 58(7):43–48, July 2005.

[137] Nolan C. Harris, Yang Song, and Ching-Hwa Kiang. Experimental free energy surface reconstruction from single-molecule force spectroscopy using Jarzynski's equality. *Physical Review Letters*, 99(6), August 2007.

[138] William J. Greenleaf, Kirsten L. Frieda, Daniel A. N. Foster, Michael T. Woodside, and Steven M. Block. Direct observation of hierarchical folding in single riboswitch aptamers. *Science*, 319(5863):630–633, February 2008.

[139] Tiago B. Batalhão, Alexandre M. Souza, Laura Mazzola, Ruben Auccaise, Roberto S. Sarthour, Ivan S. Oliveira, John Goold, Gabriele De Chiara, Mauro Paternostro, and Roberto M. Serra. Experimental reconstruction of work distribution and study of fluctuation relations in a closed quantum system. *Physical Review Letters*, 113(14), October 2014.

[140] Shuoming An, Jing-Ning Zhang, Mark Um, Dingshun Lv, Yao Lu, Junhua Zhang, Zhang-Qi Yin, H. T. Quan, and Kihwan Kim. Experimental test of the quantum Jarzynski equality with a trapped-ion system. *Nature Physics*, 11(2):193–199, December 2015.

[141] Federico Cerisola, Yair Margalit, Shimon Machluf, Augusto J. Roncaglia, Juan Pablo Paz, and Ron Folman. Using a quantum work meter to test non-equilibrium fluctuation theorems. *Nature Communications*, 8(1), November 2017.

[142] T. P. Xiong, L. L. Yan, F. Zhou, K. Rehan, D. F. Liang, L. Chen, W. L. Yang, Z. H. Ma, M. Feng, and V. Vedral. Experimental verification of a Jarzynski-related information-theoretic equality by a single trapped ion. *Physical Review Letters*, 120(1), January 2018.

[143] Andrew Smith, Yao Lu, Shuoming An, Xiang Zhang, Jing-Ning Zhang, Zongping Gong, H T Quan, Christopher Jarzynski, and Kihwan Kim. Verification of the quantum nonequilibrium work relation in the presence of decoherence. *New Journal of Physics*, 20(1):013008, January 2018.

[144] M. Naghiloo, J. J. Alonso, A. Romito, E. Lutz, and K. W. Murch. Information gain and loss for a quantum Maxwell's demon. *Physical Review Letters*, 121(3), July 2018.

[145] Takahiro Sagawa and Masahito Ueda. Generalized Jarzynski equality under nonequilibrium feedback control. *Physical Review Letters*, 104(9), March 2010.

[146] Sebastian Deffner and Avadh Saxena. Jarzynski equality in PT-symmetric quantum mechanics. *Physical Review Letters*, 114(15), April 2015.

[147] Bartłomiej Gardas, Sebastian Deffner, and Avadh Saxena. Non-Hermitian quantum thermodynamics. *Scientific Reports*, 6(1), March 2016.

[148] Meng Zeng and Ee Hou Yong. Crooks fluctuation theorem in PT-symmetric quantum mechanics. *Journal of Physics Communications*, 1(3):031001, November 2017.

[149] Bo-Bo Wei. Quantum work relations and response theory in parity-time-symmetric quantum systems. *Phys. Rev. E*, 97:012114, Jan 2018.

[150] Bo-Bo Wei. Links between dissipation and Rényi divergences in $\mathcal{PT}$-symmetric quantum mechanics. *Phys. Rev. A*, 97:012105, Jan 2018.

[151] Zheng-Yang Zhou, Ze-Liang Xiang, J. Q. You, and Franco Nori. Work statistics in non-Hermitian evolutions with Hermitian endpoints. *Phys. Rev. E*, 104:034107, Sep 2021.

[152] Gerhard Huber, Ferdinand Schmidt-Kaler, Sebastian Deffner, and Eric Lutz. Employing trapped cold ions to verify the quantum Jarzynski equality. *Physical Review Letters*, 101(7), August 2008.

[153] Jorge Kurchan. A quantum fluctuation theorem, 2001.

[154] Peter Talkner, Eric Lutz, and Peter Hänggi. Fluctuation theorems: Work is not an observable. *Physical Review E*, 75(5), May 2007.

[155] Serra Erdamar, Maryam Abbasi, Byung Ha, Weijian Chen, Jacob Muldoon, Yogesh Joglekar, and Kater W. Murch. Constraining work fluctuations of non-Hermitian dynamics across the exceptional point of a superconducting qubit. *Physical Review Research*, 6(2), April 2024.

[156] Cyril Elouard, George Thomas, Olivier Maillet, J. P. Pekola, and A. N. Jordan. Quantifying the quantum heat contribution from a driven superconducting circuit. *Phys. Rev. E*, 102:030102, Sep 2020.

[157] Jin-Lei Wu, Xin Ji, and Shou Zhang. Fast adiabatic quantum state transfer and entanglement generation between two atoms via dressed states. *Scientific Reports*, 7(1), April 2017.

[158] Ye-Hong Chen, Yan Xia, Jie Song, and Qing-Qin Chen. Shortcuts to adiabatic passage for fast generation of Greenberger-Horne-Zeilinger states by transitionless quantum driving. *Scientific Reports*, 5(1), October 2015.

[159] Francisco Andrés Cárdenas-López, Juan Carlos Retamal, and Xi Chen. Shortcuts to adiabaticity in superconducting circuits for fast multi-partite state generation. *Communications Physics*, 6(1), July 2023.

[160] Shoichi Toyabe, Takahiro Sagawa, Masahito Ueda, Eiro Muneyuki, and Masaki Sano. Experimental demonstration of information-to-energy conversion and validation of the generalized Jarzynski equality. *Nature Physics*, 6(12):988–992, November 2010.

[161] Y. Masuyama, K. Funo, Y. Murashita, A. Noguchi, S. Kono, Y. Tabuchi, R. Yamazaki, M. Ueda, and Y. Nakamura. Information-to-work conversion by Maxwell's demon in a superconducting circuit quantum electrodynamical system. *Nature Communications*, 9(1), March 2018.

[162] Xingrui Song, Mahdi Naghiloo, and Kater Murch. Quantum process inference for a single-qubit Maxwell demon. *Phys. Rev. A*, 104:022211, Aug 2021.